UNIVERSIDADE FEDERAL DE MINAS GERAIS

Instituto de Geociências da UFMG

Programa de Pós-Graduação em Análise e Modelagem de Sistemas Ambientais

Daniel Henrique Carneiro Salim

A combination of UAV photogrammetry and GIS irradiation modeling to suggest scenarios of PV transition in Fernando de Noronha Island (PE, Brazil)

Belo Horizonte

2021

Daniel Henrique Carneiro Salim

A combination of UAV photogrammetry and GIS irradiation modeling to suggest scenarios of PV transition in Fernando de Noronha Island (PE, Brazil)

Versão final

Dissertação apresentada ao Programa de Pós-Graduação em Análise e Modelagem de Sistemas Ambientais da Universidade Federal de Minas Gerais como requisito parcial para obtenção de título de Mestre em Análise e Modelagem de Sistemas Ambientais

Orientador: Dr. Marcelo Antonio Nero

Coorientador: Dr. Bráulio Magalhães Fonseca

Belo Horizonte

Instituto de Geociências da UFMG

2021

S165c
2021

Salim, Daniel Henrique Carneiro.

A combination of UAV photogrammetry and GIS irradiation modeling to suggest scenarios of PV transition in Fernando de Noronha Island (PE, Brazil) [manuscrito] / Daniel Henrique Carneiro Salim. – 2021.

126 f., enc.: il. (principalmente color.)

Orientador: Marcelo Antônio Nero.

Coorientador: Bráulio Magalhães Fonseca.

Dissertação (mestrado) – Universidade Federal de Minas Gerais, Instituto de Geociências, 2021.

Área de concentração: Análise, Modelagem e Gestão de Sistemas Ambientais.

Bibliografia: 106-126.

1. Modelagem de dados – Aspectos ambientais – Teses. 2. Geração de energia fotovoltaica – Teses. 3. Aeronave não tripulada – Teses. 4. Fotogrametria – Teses. 5. Ilhas – Fernando de Noronha, Arquipélago de (PE) – Teses. I. Nero, Marcelo Antônio. II. Fonseca, Bráulio Magalhães. III. Universidade Federal de Minas Gerais. Instituto de Geociências. IV. Título.

CDU: 911.2:519.6(813.6)

Ficha catalográfica elaborada por Elisabete Quatrini Vieira – CRB6 2210

UNIVERSIDADE FEDERAL DE MINAS GERAIS
INSTITUTO DE GEOCIÊNCIAS
PROGRAMA DE PÓS-GRADUAÇÃO EM ANÁLISE E MODELAGEM DE SISTEMAS AMBIENTAIS

FOLHA DE APROVAÇÃO

Combinação da fotogrametria com drone e modelagem da irradiância solar para sugerir cenários de transição fotovoltaica na Ilha de Fernando de Noronha (PE, Brasil)

DANIEL HENRIQUE CARNEIRO SALIM

Dissertação submetida à Banca Examinadora designada pelo Colegiado do Programa de Pós-Graduação em ANÁLISE E MODELAGEM DE SISTEMAS AMBIENTAIS, como requisito para obtenção do grau de Mestre em ANÁLISE E MODELAGEM DE SISTEMAS AMBIENTAIS, área de concentração ANÁLISE, MODELAGEM E GESTÃO DE SISTEMAS AMBIENTAIS.

Dr. Marcelo Antonio Nero - Orientador
IGC/UFMG

Dr. Bráulio Magalhães Fonseca - Coorientador
IGC/UFMG

Dr. Eduardo Coutinho de Paula
EE/UFMG

Dr. Flavio Augusto Bueno Figueiredo
UFPE

Dr. Rodrigo Affonso de Albuquerque Nóbrega
IGC/UFMG

Belo Horizonte, 30 de março de 2021.

---

sei! assinatura eletrônica

Documento assinado eletronicamente por **Marcelo Antonio Nero**, **Professor do Magistério Superior**, em 30/03/2021, às 18:04, conforme horário oficial de Brasília, com fundamento no art. 5º do Decreto nº 10.543, de 13 de novembro de 2020.

sei! assinatura eletrônica

Documento assinado eletronicamente por **Rodrigo Affonso de Albuquerque Nobrega**, **Professor do Magistério Superior**, em 30/03/2021, às 18:04, conforme horário oficial de Brasília, com fundamento no art. 5º do Decreto nº 10.543, de 13 de novembro de 2020.

sei! assinatura eletrônica

Documento assinado eletronicamente por **Braulio Magalhaes Fonseca**, **Subchefe de departamento**, em 30/03/2021, às 18:05, conforme horário oficial de Brasília, com fundamento no art. 5º do Decreto nº 10.543, de 13 de novembro de 2020.

sei! assinatura eletrônica

Documento assinado eletronicamente por **Eduardo Coutinho de Paula**, **Professor do Magistério Superior**, em 30/03/2021, às 18:06, conforme horário oficial de Brasília, com fundamento no art. 5º do Decreto nº 10.543, de 13 de novembro de 2020.

sei! assinatura eletrônica

Documento assinado eletronicamente por **Flávio Augusto Bueno Figueiredo**, **Usuário Externo**, em 30/03/2021, às 18:06, conforme horário oficial de Brasília, com fundamento no art. 5º do Decreto nº 10.543, de 13 de novembro de 2020.

A autenticidade deste documento pode ser conferida no site https://sei.ufmg.br/sei/controlador_externo.php?acao=documento_conferir&id_orgao_acesso_externo=0, informando o código verificador **0635760** e o código CRC **6955C5A2**.

Dedication

To my maternal grandfather, Moal (in memoriam), and paternal grandfather, Sebastião, for loving, teaching and supporting me.

You are my source of inspiration and will always be in my heart.

Dedicatória

Ao meu avô materno, Moal (in memoriam), e avô paterno, Sebastião, por terem me amado, ensinado e apoiado.

Vocês são minha fonte de inspiração e para sempre vão estar no meu coração.

Acknowledgments

To my mother and father, Soraya and Marcio, for their unconditional love and dedication.

To my brother, Lucas, for the eternal friendship.

To Thais, for being by my side and providing the best moments of life.

To other family members and close friends, who helped me in countless ways.

To the professors Marcelo Nero and Bráulio Fonseca, for all the guidance and support throughout this and other research.

To the other professors, students and collaborators of the PPG AMSA and UFMG, in special to Rodrigo Nóbrega, Eduardo Coutinho, Guilherme Gandra, Fábio Oliveira, and Flávio Figueiredo (UFPE).

To the collaborators of the ICMBio of Fernando de Noronha, who helped us carry out the research on the island, and in particular to the Volunteer Program, which provided the first experiences that motivated this research.

To the IGC and EE, UFMG and CAPES Foundation.

Agradecimentos

À minha mãe e meu pai, Soraya e Marcio, pelo amor e dedicação incondicional.

Ao meu irmão, Lucas, pela amizade eterna.

À Thais, por estar ao meu lado para tudo e proporcionar os melhores momentos da vida.

Aos outros familiares e amigos mais próximos, que me ajudaram de incontáveis formas.

Aos professores Marcelo Nero e Bráulio Fonseca, por todas orientações e suporte ao longo desta e outras pesquisas.

Aos demais professores, colaboradores e alunos do PPG AMSA e da UFMG, especialmente ao Rodrigo Nóbrega, Eduardo Coutinho, Guilherme Gandra, Fábio Oliveira e Flávio Figueiredo (UFPE).

Aos colaboradores do ICMBio de Fernando de Noronha, que nos auxiliaram na execução da pesquisa na ilha, e em especial ao Programa de Voluntários, que proporcionou as primeiras experiências que motivaram esta pesquisa.

Ao IGC e à EE, à UFMG e à Fundação CAPES.

Abstract

Thinking about the global and local demand to increasing renewable energy share, a concern of this century, this research presents an outstanding workflow for the advancement of photovoltaic (PV) energy and smart and solar cities. The methodology allows producing and analyzing spatial information that can guide and accelerate sustainable energy transitions, making them more feasible, intelligent, social engaged, and affordable.

The paradisiacal Fernando de Noronha Island (PE, Brazil) (FNI) was chosen as the study area because it predominantly depends on imported diesel to produce power, which results on an electrical matrix with higher costs and environmental impacts. Despite being a common reality for small and isolated islands, it is a paradoxical situation since FNI has great potential for generating wind and solar energy, is protected by environmental law, has high-standard tourism and sustainable development plans, and is internationally recognized by its extraordinary nature.

To estimate the PV potential of each roof and open area, which are respectively the locations for the installation of decentralized and centralized PV systems, initially, an unmanned aerial vehicle (UAV) photogrammetric survey was performed to generate an orthophoto (GSD of 5.3 cm) and a digital surface model (DSM) (GSD of 50 cm). In sequence, the DSM was used to produce the solar irradiation model of the Environmental Protected Area of FNI, which was calibrated for local climatic conditions, and then used as a basis for estimating the individual and total photovoltaic potential of the available surfaces. The analysis resulted on a Total Combined PV Potential of 118.6 GWh/yr. For the 1272 buildings identified, the Total Decentralized PV Potential was 51.6 GWh/yr, and for the 26 open areas, the Centralized PV Potential was 67.0 GWh/yr.

To demonstrate the application of this information in the context of planning PV transitions and solar cities, based on the analysis of the PV potentials, 9 energy transition scenarios were suggested, combining decentralized and centralized sources in different proportions to produce 20.2 GWh/year, in an integrated way. In addition to considering the location and photovoltaic potential of possible surfaces, these transition scenarios consider real factors that limit decentralized production, such as the percentage of buildings that will adopt PV systems (25%, 50%, 75%) and the roof area occupied by PV systems (10%, 25%, 50%). For example, in scenario “I” (greater use of decentralized sources), 22.0 GWh/yr of PV energy can be produced within rooftops, with centralized plants not being necessary. In scenario “A” (greater use of centralized sources), rooftops can produce 1.7 GWh/yr, requiring 18.5 GWh/yr, or 66443 m² of centralized PV energy. Depending on the degree of decentralization, the cost estimated for a PV transition vary between 550 and 2160 thousand US dollars. Finally, FNI has sufficient PV potential to achieve the transition, being able to combine centralized and decentralized production in different proportions.

Keywords: Photovoltaic, Irradiation, UAV, Photogrammetry, Energy transitions, Islands.

Resumo

Pensando na demanda global e local de aumentar a participação de energias renováveis, uma preocupação deste século, esta pesquisa apresenta um fluxo de trabalho de destaque para o avanço da energia fotovoltaica (PV) e cidades solares. A metodologia permite gerar e analisar informações espaciais que podem guiar e acelerar transições energéticas sustentáveis, tornando-as mais viáveis, inteligentes e econômicas.

A paradisíaca Ilha de Fernando de Noronha (PE, Brasil) foi escolhida como área de estudo pois depende predominantemente da importação de diesel para produzir eletricidade e, em consequência disto, possui uma matriz elétrica de altos custos e impactos ambientais. Apesar de ser uma realidade comum para ilhas pequenas e isoladas, é uma situação paradoxal visto que FNI possui grande potencial para geração de energia eólica e solar, é um ambiente com leis de proteção ambiental, turismo de alto padrão, planos de desenvolvimento e sustentabilidade, e natureza reconhecida internacionalmente.

Para estimar o potencial PV de cada telhado e área aberta, que são respectivamente os locais para instalação de fontes PV descentralizadas e centralizadas, inicialmente foi realizado levantamento fotogramétrico com drone para gerar uma ortofoto (GSD de 5.3 cm) e um modelo digital de superfície (DSM) (GSD de 50 cm). Em sequência, utilizou-se o DSM para produzir o modelo de irradiação solar na APA de FNI, que foi calibrado para condições climáticas locais, e depois serviu de base para estimar o potencial PV individual e total das possíveis superfícies. Os resultados da análise apontam que o Potencial PV Total Combinado é de 118,6 GWh/ano, sendo que para as 1272 edificações identificadas o Potencial PV Total Descentralizado é de 51,6 GWh/ano, e para as 26 áreas abertas o Centralizado é 67,0 GWh/ano.

Para demonstrar a aplicação dessas informações para o planejamento de transições PV, com base na análise dos potenciais estimados, foram sugeridos 9 cenários de transição energética que combinam em diferentes proporções as fontes descentralizadas e centralizadas, para produzir de forma integrada 20.2 GWh/ano. Além de considerar a localização e o potencial PV das possíveis superfícies, estes cenários de transição consideram fatores reais que limitam a produção descentralizada, como a porcentagem de construções que vão adotar os sistemas PV (25%, 50%, 75%) e a área de telhado ocupada para produção PV (10%, 25%, 50%). Por exemplo, no cenário "I" (maior uso da produção descentralizada) pode-se produzir 22,0 GWh/ano nos telhados, sendo desnecessário usinas PV centralizadas. No cenário "A" (maior uso da produção centralizada), 1,7 GWh/ano podem ser produzidos em telhados, requirindo pelo menos 18,5 GWh/ano, ou 66443 m² de produção PV centralizada. Dependendo do grau de descentralização, o custo estimado para uma transição fotovoltaica varia entre 550 e 2160 milhares de dólares americanos. Por fim, FNI tem suficiente potencial PV para alcançar a transição, podendo combinar a produção centralizada e descentralizada em diferentes proporções.

Palavras-chave: Fotovoltaica, Irradiação, Drone, Fotogrametria, Transição energética, Ilhas.

List of figures

Figure 13. Sample of UAV SfM-MVS photogrammetric products in FNI: A) Point cloud. B) Point cloud automatically classified. C) DSM. D) DTM. The difference between a DTM and a DSM is visualized in C-D. Buildings, trees, and objects above the surface are represented in DSM, but not in DTM, which only represents the ground surface. It is important to stress that the automatic point cloud automatic classification presented here needs to be manually refined to achieve a final-product DTM, because some structures above surfaces were considered as a ground point (red pixels in D).

Figure 14. Global Horizontal Irradiation map from GSA. Source: GSA (2020).

Figure 15. Calculation of the viewshed for one cell of a DEM. a) Horizon angles are traced along with a specified set of directions. b) Horizon angles are calculated for each direction. c) Horizon angles are interpolated in all directions. d) Horizon angles are converted to a hemispherical coordinate system. e) The resulting viewshed for a location represents which sky directions are visible and which are obscured. Numbers represent the calculated horizon angles. Source: Fu and Rich, 1999.

Figure 16. a) Left: Example of a fisheye photograph in an upward-looking manner. Right: Viewshed representation of the visible (blue) and obstructed (gray) sky. Source: Kodysh et al. (2013). b) Left: A sunmap representation from December 22 to June 22, within a 1-hour time interval, for a latitude of 45 degrees North. The sun sectors are represented by different colors of the grid. Right: Overlay of sunmap and viewshed to calculate the direct solar irradiance. Gray area represents the obstructed sun sectors. Source: Huang and Fu (2009). c) Left: A Skymap defined by sectors originated from 8 zenith divisions and 16 azimuth divisions. Right: The overlay between viewshed and skymap. Gray area means sky obstructed directions. Source: Huang and Fu (2009).

Figure 17. Configuration parameters window in ArcGIS Solar Radiation toolset.

Figure 18. Demonstration of the relationship between solar potentials estimated using GIS tools and irradiation models. The economic and environmental potential derives from the technical potential, which in turn, derives from the physical (modeled) potential.

Figure 19. Lifetime nonlinear efficiency for three PV systems composed of different materials and the same microinverter. Source: Lukač et al. (2016).

Figure 20. The number of years for the investment to be returned (i.e. NPV(y) > 0) for the two considered feed-in tariffs scenarios in Slovenia and three different PV systems. Source: Lukač et al. (2016).

Figure 21. Flowchart of the methodology.

Figure 22. Calendar of field operations. On the 18th and 19th of December 2019, bad weather precluded field operations.

Figure 23. Coordinates of the aerial photos acquired in FNI.

Figure 24. Up: GCP measured in a stripe painted on the floor. Down: Placing a marker on a photo.

Figure 25. RTK positioning scheme of GCPs measurement. The GCP distribution was mostly concentrated on the urban areas, on the areas that do not have environmental restrictions for installing PV plants, or where high-quality positional accuracy was needed. In those areas, the GCP distribution followed the recommendations presented in the literature review.

Figure 26. True (blue) and invalid (red) matches on a pair of photos. a) illustrated a pair of photos with 368 matches, from which 368 are true and 113 invalids. b) 1235 matches, from which 524 true and 711 invalids. In the last case, there were no matches over the ocean surface because it is in constant movement, which in consequence obfuscates below-surface targets and disturbs SfM reconstruction. In the first case, there was only one match over the ocean surface.

Figure 27. Sparse point cloud of Praia do Sancho, Baía dos Porcos e Praia Cacimba do Padre.

Figure 28. Dense point cloud of Praia do Sancho, Baía dos Porcos e Praia Cacimba do Padre.

Figure 29. Dense point cloud representation of Noronha II PV Plant and sloping rooftop.

Figure 30. Visual comparison of DSM with a GSD of 10.9 cm and 50 cm. Worth noting that objects above rooftops, trees and buildings are well represented in both spatial resolutions.

Figure 31. DSM produced by the photogrammetric survey. Although it did not influence PV potential analysis in buildings and open areas, the variation in ocean elevation is caused by erroneous interpolation process in water surfaces and lack of GCP located on extremities of FNI.

Figure 32. Reconstruction’s failures identified on Morro do Medeira.

Figure 33. Distribution of 22 GCP-Georeferencing inside APA-FNI.

Figure 34. Distribution of errors in GCP-Checkpoints.

Figure 35. Vectorization of buildings and open areas, the surfaces considered to produce decentralized and centralized PV energy, respectively.

Figure 36. GHI model of APA-FNI.

Figure 37. GHI map of the same areas represented by point clouds in figures 27 and 28. The high GHI open area in the southwest position is a plantation area, and the one near the center is a cleared and low vegetation area. Beaches and hills have lower GHI because of cliff shading and steep terrain slope.

Figure 38. GHI map of sector in Vila dos Remédios neighborhood. It is notable that GHI varies because of the shading caused by trees and buildings and due to variation in slope and orientation of the surfaces.

Figure 39. GHI data extracted by building vectors.

Figure 40. GHI data extracted by open area vectors.

Figure 41. PV-Potential of some open areas in APA-FNI.

Figure 42. Monthly GHI in two sample buildings to illustrate the GHI variation throughout the year in rooftop faces oriented to north and south. Between March and September, GHI is higher in faces pointing north. Between October and February, GHI is higher in faces pointing south.

Figure 43. Web GIS platform. Clicking on a building footprint opens a pop-up window informing area and mean annual and daily GHI.

Figure 44. Web GIS platform. Zooming in will show the annual GHI in rooftops.

List of tables

List of acronyms

ABSOLAR – Brazilian Association of Photovoltaic Energy

AC - Alternate current

ADEFN – Public Administration of Fernando de Noronha

AHP – Analytical Hierarchy Process

AI – Artificial Intelligence

ANEEL – National Electric Energy Agency

AOI – Area of Interest

APA-FNI – Environmental Protected Area of Fernando de Noronha Island

ASPRS - American Society for Photogrammetry and Remote Sensing

BBA – Bundle Block Adjustment

CELPE – Pernambuco Energy Company

CI – Carbon intensity conversion rate

DC - Direct current

CSP – Concentrating solar power

DEM – Digital elevation model

DSM – Digital surface model

DTM – Digital terrain model

ESRA – European Solar GHI Atlas

FNI – Fernando de Noronha Island

GCP – Ground control points

GHG – Greenhouse gases

GHI – Global Horizon Irradiation

GIS – Geographic Information System

GSA – Global Solar Atlas

IBGE – Brazilian Institute of Geography and Statistics

ICI – Initial capital investment

ICT – Information and Communication Technologies

ICMBIO – Chico Mendes Institute for Biodiversity Conservation

IoT – Internet of Things

LCOE – Levelized cost of energy

MCDM – Multiple Criteria Decision Making

MVS – Multiview Stereo

NAVGNSS – Navigational GNSS

NPV – Net present value

O&M – Operation and maintenance

OSM – Open Street Maps

PARNAMAR-FNI – National Marine Park of Fernando de Noronha

PP – Payback period

PPK – Post-processing Kinematic

PR – System performance ratio

PS – Project Sunroof

PV - Photovoltaic

R&D – Research and development

RMSE – Root mean square error

ROI – Return of Investment

RPA – Remotely Piloted Aitcraft

SDG – Sustainable development goals

RS – Remote Sensing

RTK – Real-time Kinematic

SfM – Structure from Motion

SIFT – Scale-invariant feature transform

SNUC – National System of Nature Conservation Units

SUAS – Small Unmanned Aircraft Systems

UAV – Unmanned Aerial vehicle

UHSR – Ultra high spatial resolution

UNESCO – United Nations Education, Scientific, and Cultural Organization

η – PV Module efficiency

Summary

1. Introduction

The social, environmental, and economic demands of the 21st century push-forward our society towards a renewable energy transition. Typically, in the case of isolated islands, where diesel power plants are the main source of energy, the energy matrix is centralized and associated with high costs and environmental impacts. As power alternatives, renewable sources are technologies that are more reliable, economic, environmentally friendly, and capable of decentralization. In this context, solar photovoltaic (PV) energy is one of the keys technologies to achieve a clean energy future and sustainable world.

Thinking on smart and solar cities, they aim to analyze and efficiently use the solar resource to produce PV. In this way, solar irradiation modeling is a powerful technique that enable estimation of PV potential in surfaces, such as rooftops or open areas, which are most common surfaces to produce PV power in decentralized and centralized ways, respectively. In irradiation modeling, the spatial resolution must be considered when using the tool for decision-making and planning. Only high spatial resolution irradiation models, with maximum ground sample distance (GSD) of 100 cm, can discount shading caused by buildings and trees and also model slope, aspect, and elevation of surfaces.

In this perspective, unmanned aerial vehicles (UAVs) photogrammetry is a remote sensing (RS) technique that are transforming the production of high spatial resolution orthophotos and digital elevation models, and, in consequence, innovative and affordable solutions are being developed for spatial analysis on geographic information systems (GIS) environments. In the context of developing countries, where there is a huge demand for high quality GIS data, which could promote environment and territorial management, urban planning, renewable energy transition planning, among others development processes, UAV photogrammetry is a powerful tool to generate spatial data that assist policy and decision making.

With all this perspective, this study took place in Fernando de Noronha Island (FNI), located 355 km offshore from the Brazilian northeast coast, at 3°51’S and 32°25’W. It is a tropical, remote island that depend on diesel importation to produce electricity, with only 8% of renewable energy penetration. In that way, this research focuses on the integration of RS and GIS techniques to collect and produce spatial data that elucidate the PV potential of FNI. To this extent, a UAV photogrammetry survey was conducted in December 2019 to produce a digital surface model and an orthophoto, which were used to produce the solar irradiation model and to perform the PV potential analysis in FNI, considering the building rooftops as surfaces for decentralized PV production and the open areas as places to install PV plants, representing the centralized PV production. Based on real-world factors limiting decentralized PV Potential (percentages of buildings adopting PV rooftop systems and rooftop area occupied by PV modules) and centralized PV Potential (areas already cleared, without vegetation), scenarios of PV energy transition considering different proportions of decentralization are suggested for FNI.

1.1. Characterization of the problem and justifications of the research

FNI faces a typical small island problem, the dependence fossil fuels for power production and energy security. Regarding renewable energy consumption in FNI, the Solar Plants Noronha I and Noronha II were designed to produce 1.4 GWh, which corresponds to less than 8% of the electricity produced by the Tubarão Thermoelectric Plant in 2018, which were 19.4 GWh, as reported by Celpe (2019). Figure 1 illustrates the location of power plants in FNI. The negative, unnecessary consequence of that is a centralized energy system with a high rate of greenhouse gases (GHG) and pollutant emissions, high electricity costs, and low levels of energy security and autonomy. In this manner, FNI aims to reduce the reliance and consumption of fossil fuels and increase the participation of renewable energy sources.

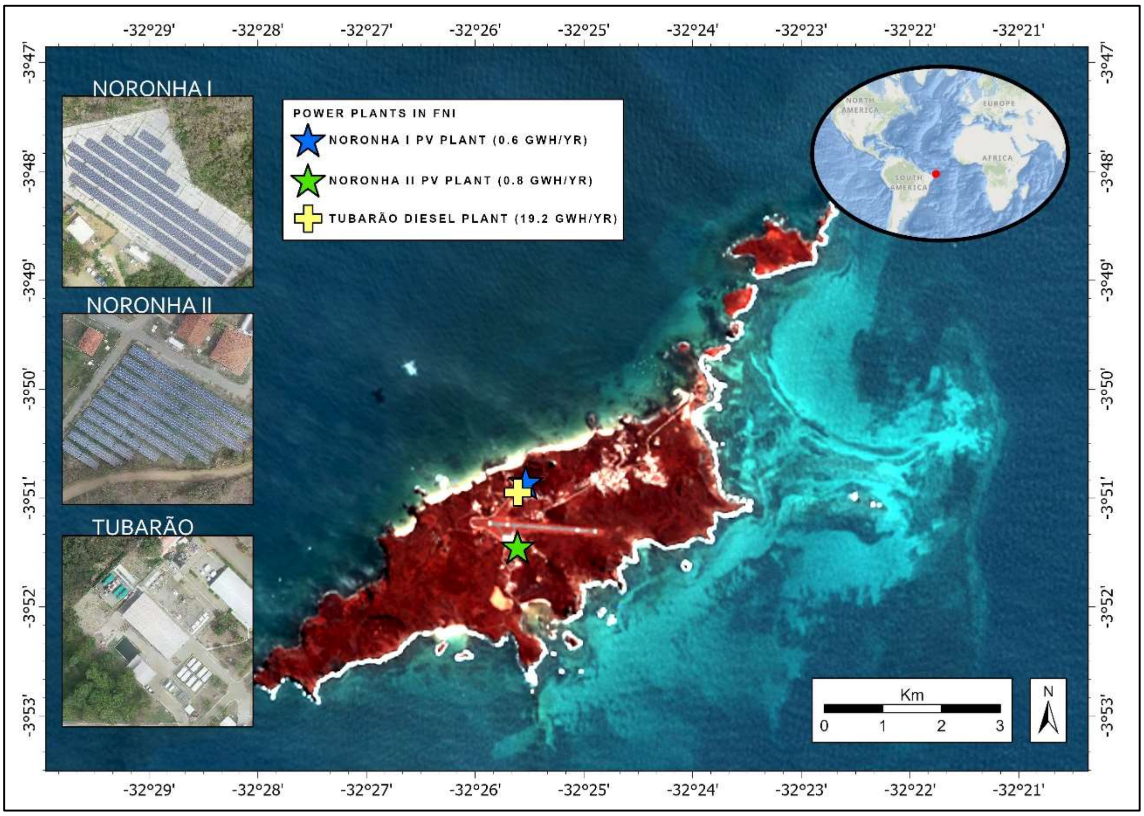

Figure 1. Location of PV and diesel power plants in the Archipelago of Fernando de Noronha. The background image is a modified Landsat 8 OLI/TIRS Level-1, from July 2019.

Regarding photovoltaic energy production, it is well known that the greater the solar irradiation incident on a PV module installed on a given surface, the greater the production of electricity. Thinking on an efficient transformation of solar radiation in PV power, it is recommended that PV module are installed on surfaces with less shading and with an optimum slope and orientation angles. In this context, solar irradiation modeling and analysis in high spatial resolution produce data that enlighten the numbers regarding the potential to generate PV power in any given area. However, it is worth mentioning that there is no available spatial data in high spatial resolution for modeling the solar resource in FNI, which is essential for the planning, acceleration, and guiding of a renewable energy transition.

FNI is a place of remarkable, paradisiac landscapes, with a magnificent flora and fauna and a vulnerable ecosystem, which is particularly important for reproduction and nursery of birds and maritime species. Moreover, the Archipelago is protected by federal environmental legislation and is recognized as a Natural World Heritage Site (UNESCO, 2020). Thereby, the island was chosen as a study area because environmental awareness is vivid and sustainable actions are regularly engaged by the local islanders, government administration, tourists, private sector, and non-government organizations.

Furthermore, FNI was also selected because of its territorial and populational sizes, which are suitable for the workflow proposed in this dissertation and works as a small-scale example that can be replicated later in larger areas. Nonetheless, taking advantage of FNI world-wide recognition, this research demonstrates that environmental sciences tools and methods have great potential to contribute to real world demands and decision-making processes, such as planning of renewable energy transitions.

Key questions that guided this research were “Which and where are the available surfaces for installing PV systems?” and “Does FNI have enough photovoltaic potential to achieve a renewable energy transition?”.

1.2. Proposed solution and methods

1.2.1. General objective

Integrate UAV photogrammetric surveying and GIS solar irradiation modeling and analysis to propose 9 scenarios of PV transition for FNI.

1.2.2. Specific objectives

To achieve the general objective, the specific objectives aimed in this research are:

a) Perform and evaluate a UAV photogrammetric survey to produce an orthophoto and a digital surface model of FNI.

b) Model and analyze solar irradiation in the Area of Environmental Protection of FNI (APA-FNI) with a GSD of 50 cm. In sequence, estimate individual and total PV potential of rooftops (decentralized) and open areas (centralized).
c) Propose scenarios of PV transitions, where decentralized (PV rooftop) and centralized (PV plants) sources are combined in different proportions, real-world limiting factors are considered, and cost estimation analysis are performed.

1.3. Originalities

This research presents innovative ideas and point of views that were inspired on papers that focused on UAV photogrammetry, high spatial resolution irradiation modeling and renewable energy transitions in islands. In the course of the literature review, although papers discussed UAV photogrammetry and irradiation modeling in cities or analyzed low resolution irradiation data to locate PV plants in islands, none had integrated the three topics in a single research.

It is likely that this research is the first one to do both, consider an island environment and produce an irradiation modeling based on UAV photogrammetric survey.

Another original element of this research is to associate high resolution irradiation data to propose scenarios to achieve PV transition, in a way that centralized (PV plants) and decentralized (PV rooftops) sources are combined in several proportions. It is considered real-world limitations for PV decentralized production, such as percentage of rooftop area occupied by PV modules and percentage of buildings that will install PV power systems, because some buildings do not have enough roof structure to support the weight of PV systems. Moreover, the suggested areas to install centralized PV plants are areas that had been previously cleared, which contribute to reduce pressure on scarce vegetated lands.

Worth noting that this research presented a complete process that started from almost zero and ends up with the finest data capable of addressing key demands in macro-problems, such as the production of a cartographic database and the planning of a centralized and decentralized PV energy transition.

1.4. Social Implication

The present research can be related to three sustainable development goals (SDG) of the 2030 Agenda of the United Nations: 7 (Affordable and clean energy), 9 (Industry, innovation and infrastructure), and 11 (Sustainable cities and communities).

In the context of global climate change, where a global response will only be significant if local communities do their part concerning renewable energies, the workflow proposed in this research is of great importance to plan and perform efficient and planned PV transitions at the community and neighborhood scale. Even though this study is focused on a remote island environment, which is fossil fuel dependent and has an isolated electricity system, the methodology can be replicated in any place that plans to improve the PV percentage in the electricity matrix or perform a PV energy transition. It can be reproduced on areas connected to continental energy systems, such as entire cities, specific zoning area (residential, commercial, recreational, industrial), and particular properties (farms, hotels, factories). As well as on remote areas, with isolated energy system, for example small communities living in desert, forest or island environments, typically powered by diesel power generators.

It is important to stress that the data offered by solar models in high spatial resolution has a great potential to plan, accelerate, and guide a PV energy transition because they provide data for both, the public administrators that want to make decisions based on cost-effective and technical data, and the individual consumers that want to install their own PV system.

In the typical conditions of cities in developing countries, where there is a huge demand for the finest geospatial data that guide sustainable development and planning, this research demonstrated that public administrators and decision-makers should make use of the advantages and vast applications offered by UAV photogrammetry.

1.5. Scope and limits of this research

It was out of the scope of this research:

a) Consider other renewable energy sources than solar PV, such as concentrated solar panels, wind, biomass, oceanic, among others.
b) Consider fundamental aspects of renewable energy transitions, such as storage battery systems, smart-grids control and automation, individual power consumption by building, diesel generator backup, among others.
c) Validate irradiation data using an annual pyranometer monitoring station or similar measurement tool.
d) Consider a life cycle analysis in calculation of CO_2 emission avoidance when replacing diesel thermoelectric plants by PV modules (Environmental potential).
e) Analyze PV potential in restricted areas.

The limits of this research can be seeing as ideas for future research.

2. Background – Fernando de Noronha Island

It is assumed that the Mappamundi of Juan de la Cosa, made around 1500, indicated an island with a format similar to FNI, and thereby, in some way, Juan de la Cosa can be considered a visual discoverer of FNI (Castro, 2001). At that time, the nobleman Fernán de Loronha was funding the Portuguese overseas expeditions. In one of those voyages, the Archipelago was found and described in detail by Amerigo Vespucci, another considered discoverer of FNI. The Italian explorer and navigator highlighted in his letters the exuberant flora and fauna, the isolation, the geology, and the lack of human occupation. Because of Loronha's sponsorship, King Manuel I of Portugal donated the Archipelago to Loronha as the first Brazilian Captaincy Hereditary (Silva, 2013).

The strategical position in the Atlantic Ocean marked the history of FNI by forced invasions of English, Dutch and French countries during the XVII and XVIII centuries, and by cooperation with the Allies during World War II and with the North Americans during Cold War. Moreover, the Archipelago was a place that exiles, political prisoners, and common prisoners were sent to serve time in prisons (Nascimento, 2009).

The Military Federal Territory of Fernando de Noronha was ratified by the Decree-Law No. 4.102/1942 (Brasil, 1942). Following that, the Decree-Law No. 94.780/1987 and the 1988 Federal Constitution sanctioned it into a State Territory and settle the first civil administration ever in FNI (Brasil, 1987; Brasil, 1988b). In 1988, the Decree-Law No. 95.922/1988 (Brasil, 1988a) established the ecological zoning of the Archipelago to control urbanization and conserve, preserve and restore natural resources. It consequently boosted the creation of the Fernando de Noronha National Marine Park, still in that year.

The Archipelago of Fernando de Noronha is located at 3°51'S and 32°25'W, close to the Equator. According to the Global Wind Atlas (GWA, 2020), the average annual wind speed at 100 meters high on the Island is 8.4 m/s, and according to the Global Solar Atlas (GSA, 2020), the average annual Global Horizon Irradiation (GHI) is 2175 kWh/m²/year, or daily GHI is 5.95 kWh/m²/day. Therefore, the geographical location of the Fernando de Noronha Island within the equatorial belt (between 5° N and S latitudes) ensures abundance of renewable energy resources. Despite the high standard ecotourism and numerous sustainable and conservation projects, the island is still heavily dependent on fossil fuel importation.

The Archipelago has one main island, the FNI, and 20 islets surrounding it. The FNI has approximately 2000 hectares of terrestrial area and is 350 Km distant from the Brazilian continental coast. Figure 2 presents different band compositions from a Landsat 8 OLI/TIRS Level-1 image of July 2019.

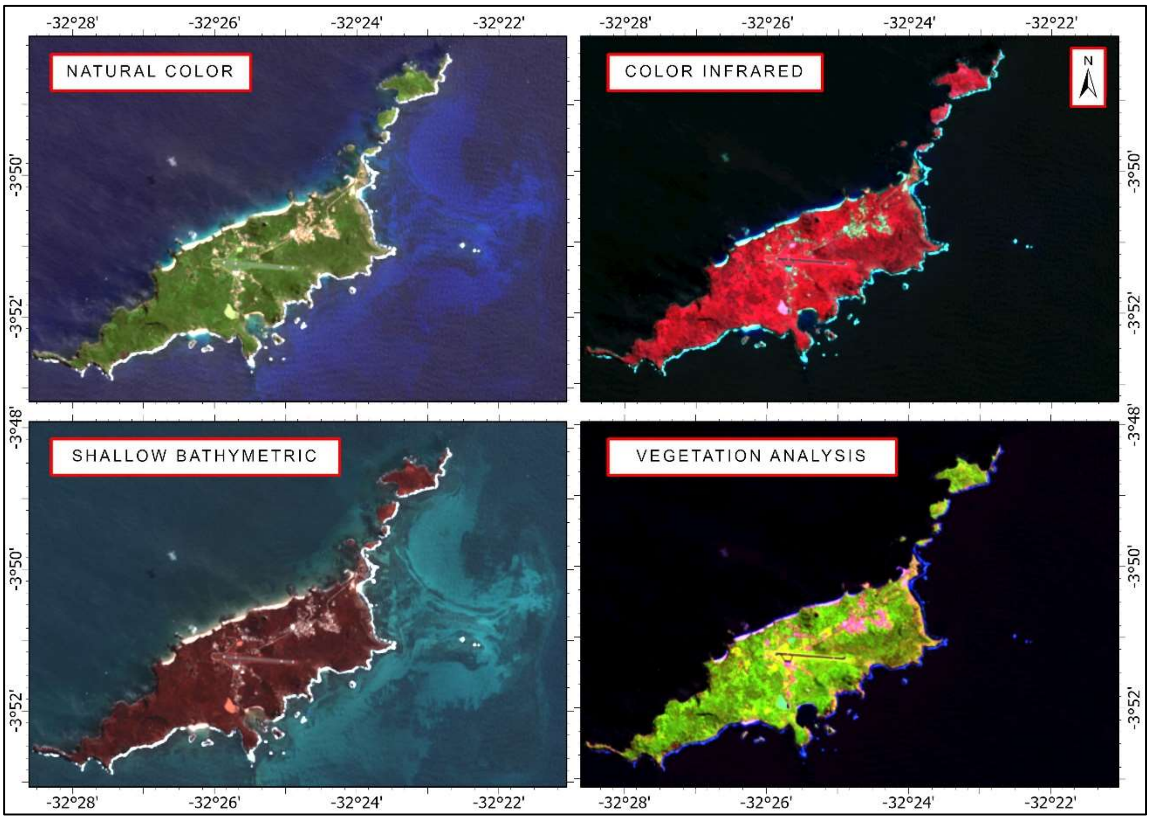

Figure 2. Different band composition (ArcGIS Pro tools) of a Landsat 8 OLI/TIRS Level-1, from July 2019.

There are two well-defined main seasons, a dry from August to January and a rainy from February to July. The mean annual temperature is 25.4 °C and has a small variation. The typical winds come from SE direction, at an average speed of 6.6 m/s, being faster during July and August (Sales, 2018).

The Brazilian Institute of Geography and Statistics (IBGE) database estimates a population of 3.061 inhabitants in 2019 and reports tourism as the main economic activity (IBGE, 2020, a). Although the island receives more tourists each year, over than 115,000 tourists in 2019, it is notable the need to improve management and infrastructure of basic sanitation (water treatment, wastewater treatment, stormwater drainage, and solid waste disposal). Worth noting that subsistence agriculture and artisanal fisheries are common habits in islanders' families.

FNI is well known because of its scenic landscapes, preserved ecosystems, and importance for reproduction and feeding of oceanic birds and marine fauna. Since 2001, the Archipelago is classified as a Natural World Heritage Site, by United Nations Education, Scientific, and Cultural Organization (UNESCO) (UNESCO, 2020).

Claudino-Sales (2018) pointed out that biodiversity (flora and fauna diversity) from FNI is relatively poor in variation but rich in endemism, which is expected due to the FNI isolation. The authors also stressed out that uncontrolled tourism implicates in negative environmental impacts, such as soil trampling, the introduction of invasive species, biological disturbances, and pollution. They concluded their work highlighting that in FNI the threat to the natural property is relatively low and the state of conservation is considered good, with some concerns, for example, lack of resources and monitoring tools.

In this context, Mello e Oliveira (2016) drew attention to an especially important issue that could be potentially managed by using high-resolution spatial data, which is the biological threats imposed on the island's natural balance by invasive species, particularly the tree “Leucaena leucocephala”. An initial step for managing negatives impacts from invasive species is the identification, quantification, and location of individuals, along with understanding their surrounding environment and relational species, which is why data with ultra-high spatial resolution is recommended.

Some species and scenes found in FNI are illustrated in Figure 3.

Figure 3. Photos of fauna and scenic views from FNI. For species, the first name is the Popular name (in portuguese) and the second is the scientific name. **a)** Praia do Sancho. **b)** Aratu Vermelho (in portuguese), *Goniopsis cruentata*. **c)** Atobá de pata vermelha (in portuguese), *Sula sula,* and the “Morro do Pico” behind the sea bird. **d)** Mabuia (in portuguese), *Mabuya maculata*. **e)** Enseada dos tubarões.

Ribeiro et al. (2017) indicated that the relief of FNI is composed by “beaches, plains, slopes, low plateaus, hills, shore cliffs and a high plateau, which is where the small town of Vila dos Remedios lies and where most of the inhabitants of the island live”.

Since 1988, the Pernambuco Energy Company (CELPE), currently managed by Neoenergia and Iberdrola groups, is responsible for the generation, transmission, and distribution of electricity in the FNI. According to the Pernambuco State Database (2020), in 2018 was consumed 18.590 MWh in FNI, as shown in Figure 4. Moreover, 46% and 33% of electricity was consumed by the commercial and residential sectors, respectively (Figure 5). Celpe (2019) mentioned that there are 976 power consumption units, and that the average monthly consumption of a unit is 900 KWh. The high-rate consumption can be justified by the high-standard tourism and energy consumption for water desalinization.

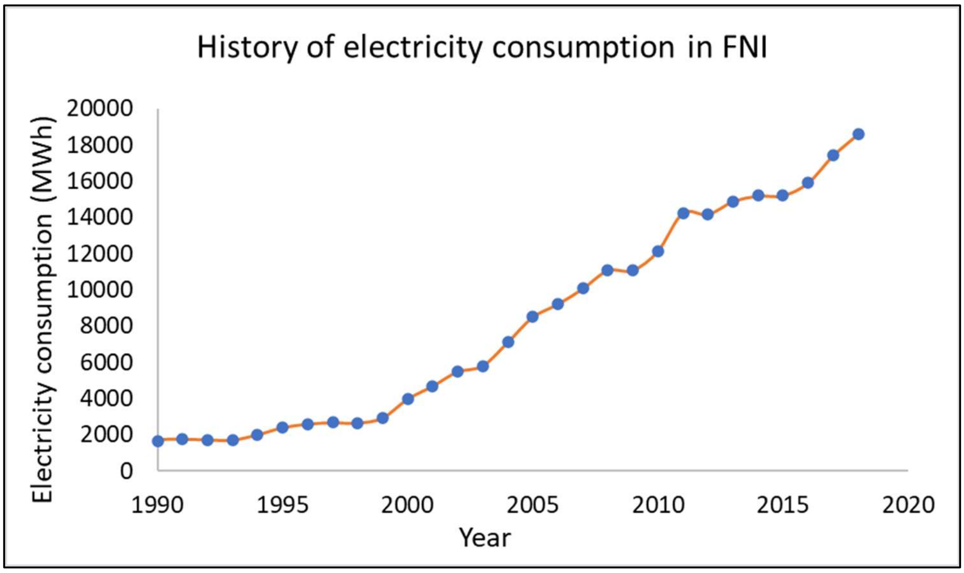

Figure 4. History of annual electricity consumption in FNI. Based on Pernambuco State Database (2020).

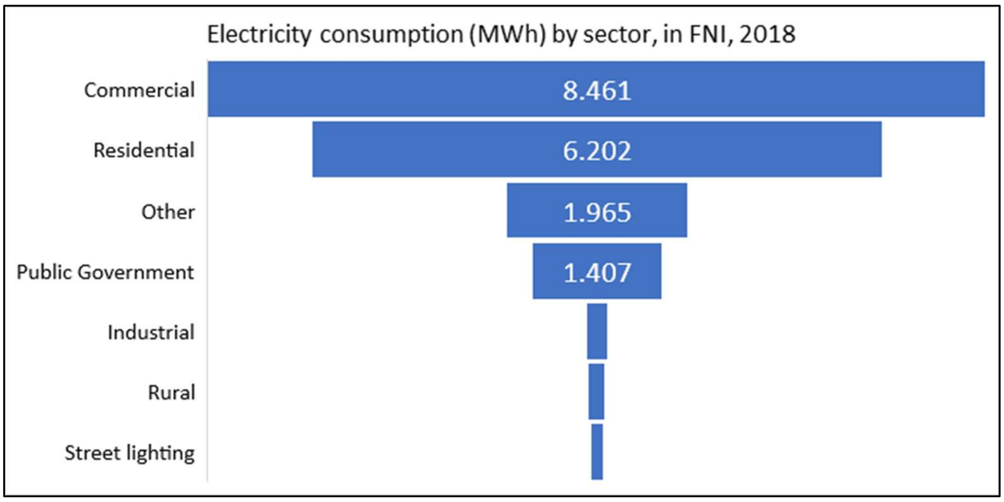

Figure 5. Electricity consumption by sector, in FNI, 2018. Based on Pernambuco State Database (2020).

Celpe (2019) reported that electricity in FNI is generated by the Tubarão Thermoelectric Plant and the PV Plants Noronha I and II. The PV plants were designed to produce 1400 MWh annually and avoid the consumption of 375 m³ of biodiesel, which corresponds to 8% of electricity consumed in FNI. Regarding the diesel consumption at the thermoelectric, a 10% parcel is replaced by biodiesel, a less polluting source. However, since 2017 the company is participating in a Research and Development (R&D) program that aims at developing an intelligent energy storage system. Moreover, Celpe (2019) indicated that the company performed an R&D program for smart grids from 2012 to 2017, and in 2018 started another R&D program that aims to promote and implement electric vehicles in FNI.

As reported by Celpe (2019), the energy generated in 2018 by Tubarão Thermoelectric Plant was 19.2 GWh, which corresponds to the consumption of 5378 m^3 of diesel. It is important to note that the numbers reported by Celpe (2019) are not the same as the ones presented by the Pernambuco State Database (2020).

In 2000, the company expanded the existing wind turbine to a power capacity of 225 kW but, unfortunately, in 2009 it was struck by lightning and collapsed down.

It is important to note that the FNI, like most small and isolated islands, does not efficiently exploit the available renewable energy resources and continues to depend on fossil fuels. It is reasonable to stress that although some policies and actions seek sustainability and environmental preservation on the island, there is still a lot to improve in terms of renewable energy sources.

Under the National System of Nature Conservation Units (SNUC) definitions of a protected area, detailed by the Decree-Law No. 9.985/2000 (Brasil, 2000), there are two main types of conservation units: Sustainable Use Units and Full Protection Units. The first allows organized human occupation and natural resources exploitation in a restrained form. The second is mainly focused on preserving the natural ecosystem. It prevents human occupation but authorizes scientific research, environmental education projects, and controlled tourism (MMA Brasil, 2011).

The Archipelago's area is composed of the National Marine Park of Fernando de Noronha (PARNAMAR-FNI) and the Environmental Protected Area of Fernando de Noronha (APA-FNI). PARNAMAR-FNI is a Full Protection Unit and APA-FNI a Sustainable Use Unit. Thereby, the PV energy production is limited to the APA-FNI area.

The Public Administration of Fernando de Noronha (ADEFN) represents the civil governmental power at the local scale, and the Chico Mendes Institute for Biodiversity Conservation (ICMBIO) the environmental federal agency power. The ADEFN concentrates his actions in the APA-FNI area, whilst in the PARNAMAR-FNI area the EcoNoronha, a private company, has the concession to operate and manage the ecotourism activities. The ICMBIO manages both conservation units through inspections and control actions.

3. Literature review

3.1. Photovoltaic energy and solar cities and islands

3.1.1. Overview

Solar photovoltaic energy is the key to a clean energy future because it is renewable, affordable, abundant, does not emit GHG when electricity is produced and represents a long value chain with good job opportunities.

The sun is a primordial and inexhaustible source of energy. Solar energy is harvested by PV generator systems mounted most commonly on the ground and rooftops.

It is a key renewable energy resource that can substitute fossil fuels and reduce carbon emissions, which is a social, environmental, and economical concern in the last decades (Kabir et al., 2018).

The main factors behind spatial and temporal variation in solar irradiation are the geographical location – defined by longitude, latitude, altitude; season – defined by solar distance and angles; atmosphere interactions – defined by cloud cover and aerosols; and shading effect – defined by topography obstructing sunlight rays. However, in urban areas, the solar irradiation in buildings' rooftop varies eminently due to complex urban morphology, such as buildings, trees, and objects above the surface. Therefore, for urban analysis and decision-making is essential to consider solar irradiation maps with sufficient spatial resolution and temporal distribution (Hofierka and Zlocha, 2012).

As stated in the brief history elaborated by Green (2000), the solar cells were one of the most remarkable scientific developments of the 20th century. Its origins can be traced back to the *energy levels* described by Max Planck and to the *photons* and *photoelectric effect* explained by Albert Einstein, which were followed by Edwin Schrodinger, with the *wave equation*, and Wilson, which solved the *wave equation* for solid materials in 1930. According to Green (2000), at this point, it was possible to classify materials as good conductors, semiconductors, or insulators of electrons. In 1940, Russel Ohl identified regions in a metal impure silicon rod that was electrically charged negatively and positively, that later was defined as the *p-n junctions* in solar cells. In 1949, William Shockley presented the theory of devices with p-n regions, the first transistor designed. It was only in 1954 that all this scientific progress culminated in an efficient solar cell.

In systematic literature research, Sampaio and González (2017) observed that the terms “electricity”, “solar irradiance”, “direct generation” and “conversion” are the most commonly used by authors to define PV energy. In this way, they stressed the following definition: “electricity obtained directly from the conversion of solar energy”. Smets et al. (2016) defined the *photovoltaic effect,* which is the phenomena behind PV energy and solar cells, as “the generation of a potential difference at the junction of two different materials in response to electromagnetic irradiance”. These materials are generated by the doping process, which is the addition of atoms with more or fewer electrons than Silicon (Si) to the crystal lattice layer, usually Boron or Phosphorus (Luque and Hegedus, 2011). One material is an n-type semiconductor, with more negative charges moving freely through the layer, and the other one is a p-type semiconductor, with positive charges moving freely, also known as “holes”. The n-p junction functions as a depletion zone, it prevents the “holes” to reach the n-semiconductor and the electrons to reach the p-semiconductor. Thus, the electrons freed due to the photovoltaic effect are orientated towards the electrodes instead of the p-semiconductor layer (Smets et al., 2016).

Moreover, to generate electricity, solar cells are made of semiconductors materials composed of two bands or levels of energy: the valence band (lower energy) and the conduction band (higher energy). The sunlight incident upon the metallic surface gives up energy to release the electron from the valent band to the conduction band. The difference in the level of energy (measured in electron-Volts) between these bands is called a bandgap. In that way, the photons are responsible for providing the energy needed by electrons (from the valent band) to overcome the bandgap and reach the conduction band. In sequence, the released electron load is carried throughout the conduction band of conductive materials (electrodes) into the circuit, charge controller, and then the inverter, to transform direct current (DC) in alternate current (AC) (Luque and Hegedus, 2011). Figure 6 illustrates a basic solar cell working.

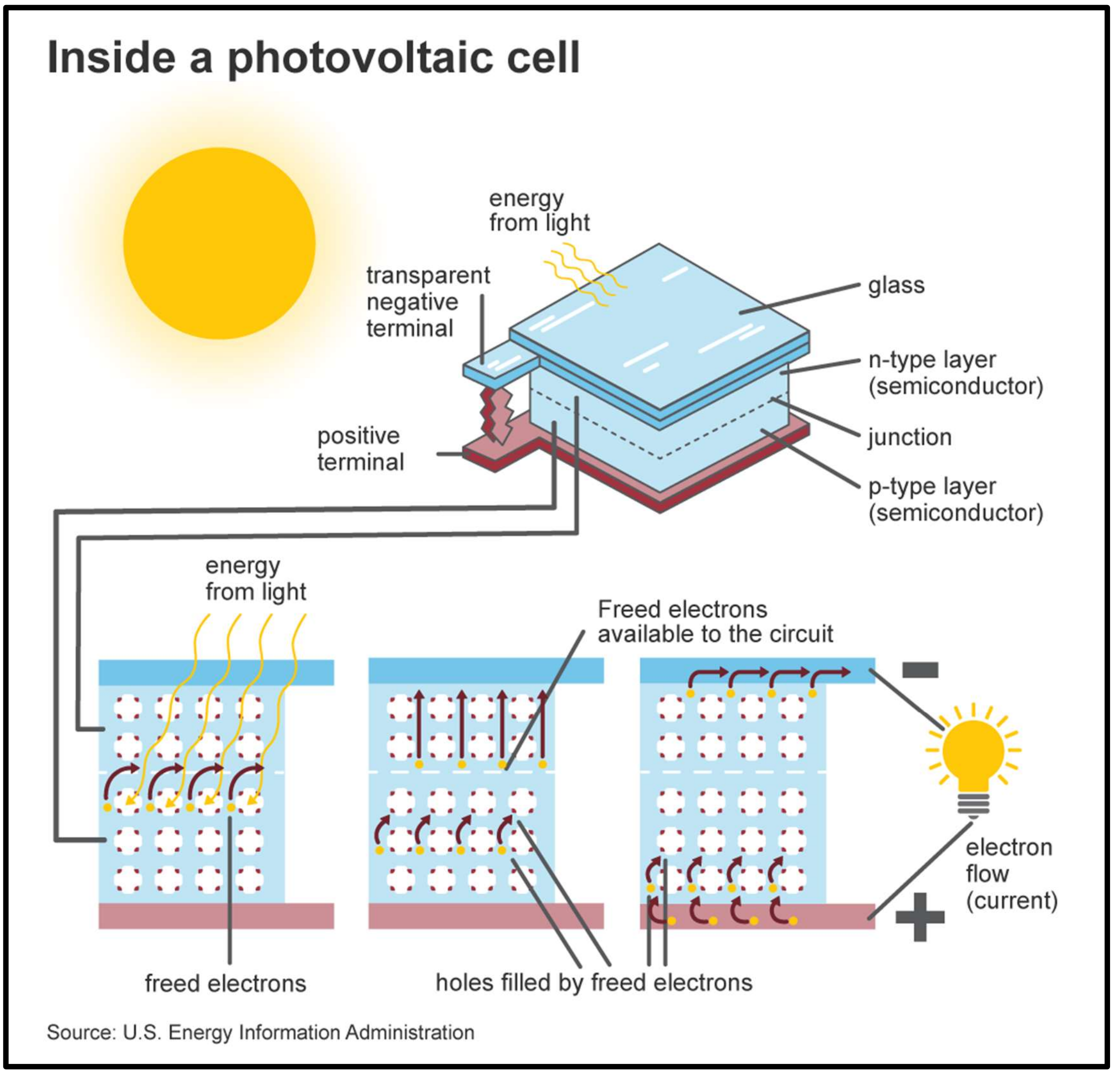

Figure 6: Conventional photovoltaic cell. Source: US EIA, 2020.

3.1.2. PV systems

Lopez et al. (2012) classified solar power technologies in four types: urban PV farm, rural PV farm, rooftop PV, and concentrating solar power (CSP). A CSP system is a utility-scale farm that uses multiple reflexive surfaces to concentrate the solar heat in a specific point location. The urban PV plants are solar PV plants greater than 1.8 ha, and rural more than 100 ha. At a smaller scale, rooftop PV systems are owned by consumers and the produced electricity is consumed on-site, stored in a battery system, or loaded into the grid. Indeed, rooftop PV systems represents decentralized sources, while the other types centralized.

Brewer et al. (2015) stressed out that in the case of PV plants, the greater the terrain slope, the greater the difficulties and costs of construction. For example, Lopez et al. (2012) recommended that PV plants were installed in terrains where slope does not exceed 3%.

Although operation and maintenance (O&M) expenditures are relatively low in PV systems, they require an extensive initial capital investment (ICI), which depends on the size of the new PV system and represents a significant share on the Levelized Cost of Electricity (LCOE) (Vartiainen et al., 2019). The LCOE, typically expressed in $/KWh, was created to compare the relative cost of electricity produced by different sources or situations, considering life cycle period of the energy project, ICI, O&M, performance, fuel costs, etc. In some cases, it is needed to construct new power lines and substations to connect the PV plant to the existing distribution grid, which will increase ICI and LCOE. Moreover, the grid power line connected to the solar farm or rooftop PV must have the appropriate hosting capacity to support the added load of electricity, if not it can cause overcurrent and overvoltage on the network grid (Etherden and Bollen, 2014).

The electricity system, or electric power grids, is the integrated network composed of power plants, substations, transmission and distribution lines, and end-consumer units. The system can be planned at a centralized, decentralized or both levels.

According to Hiremath et al. (2007), centralized generation systems focus on a few and distant power plants producing energy, giving preferences to distribution in large urban cities over small towns, rural areas, and urban poor communities. The authors argue that centralized systems do not consider social and environmental factors on a regional and local scale, which makes any intervention more challenging.

Kaundinya et al. (2009) defined a decentralized system as a system that the generated energy is consumed nearby, e.g., rooftop PV or urban PV farm, and are designed to supply local energy demand. Although decentralized systems increase individual autonomy due to the benefits in energy security and financial savings in electric bills, the LCOE of PV energy on rooftops is higher than in solar farm systems mounted on-ground due to their smaller size and scale (Kuang et al., 2016). Furthermore, Goldthau (2014) claims that climate change targets and rising demand for electricity access will require decentralized energy solutions and advances in the energy infrastructure of countries.

3.1.3. Global and Brazilian context

According to REN21 (2019), the global expansion of the PV system in 2017 was supported by the market competition, growing demand for energy in developing countries, and the growing awareness to diminish pollution and GHG emissions and ensure everyone accesses to energy. The report indicated that innovations in industry were led by energy efficiency and cost reduction disputes. It highlighted that government policy was a significant driver to the global growth industry. In 2017, the bid prices reached low records of 30 USD/MWh (in Saudi

Arabia) compared to the 100 USD/MWh in 2010 (in the United States of America), representing a reduction of 73% in 7 years, or approximately 10% per year from 2010 to 2017. For comparison, on average there was a cost reduction in bid prices of 6% each year over the last four decades, demonstrating that in the last 7 years the bid prices are reducing more than previously. Still in the global context, IRENA (2019) highlighted that PV remained the top leader employer among renewables, representing one-third of all renewable energy jobs.

In addition to that, Creutzig et al. (2017) pointed out that among renewables energy, PV energy has grown the most in the last 40 years and has the steepest learning curve (module price vs cumulated capacity). The authors concerned that the Southern hemisphere has huge potential for solar energy, but also has countries that are immature, with limited institutions and mechanisms to deal with the up-front capital investment required for renewable energy systems and transitions. They stressed that the need for automation and intelligent technologies in smart power grids are also a challenge to global energy management and industry. In the same context of PV expansion, Hofierka et al (2014) mention that policies and beneficial support represent a vital role in PV systems adoption, for example, subsidies, easy access to capital credit, tax reduction, and excessive energy production trading.

In the context of islands, Kuang et al. (2016) highlighted that the majority of islands still rely on the importation of fossil fuels as the main energy source for power supply. The authors mention that in the Caribbean islands and most world islands, 90% of the energy demanded depends on imported fossil fuels. Thereby, energy costs can lead to difficulties in overall island management. For example, in Small Island Developing States, fuel imports can represent up to 20% of annual importation costs, and in some other world islands up to 30%.

More information about the use of solar photovoltaic in cities and islands will be presented in 3.1.4 Solar cities and islands.

3.1.3.1. Brazilian context

The Brazilian Association of Photovoltaic Energy (ABSOLAR) highlighted in its most recent infographic regarding PV energy in Brazil (ABSOLAR, 2020): **i)** 2.2% of the electricity supply in Brazil was generated by PV sources in January 2020. **ii)** Between the years 2012 and 2019, the PV sector generated more than 130k jobs and it is estimated to create 120k more in 2020. **iii)** In 2019, PV decentralized sources accounted for 2226 MW (45%) and centralized 2673 MW (55%). In 2017 it was 191 MW (16%) and 968 (84%), respectively. **iv)** Between the years 2013 and 2019, the average price of energy auctions in the regulated market dropped from 103.00 USD/MWh to 20.33 USD/MWh, which represents a reduction of 80.3%.

The National Electric Energy Agency (ANEEL) is responsible for regulating and supervising the generation, distribution, and transmission of electric energy in the country. The Normative Resolution (NR) 482 of April 2012 (ANEEL, 2012) classifies decentralized sources in two categories: mini-generation and microgeneration. The first includes systems with power generation capacity between 75 kW and less than or equal to 5 MW, while the second refers to systems with less than 75 kW. The regulation allows the consumers to install private energy renewable systems to generate their energy and supply the surplus to the distributor's network and use it as credits (ANEEL, 2012).

De Andrade et al. (2020) presented a historic view of the distributed generation (DG) rules, focusing on the Public Hearings held by ANEEL since 2010 and the impacts of those in regulations. For example, NR 482/2012 was revised in NR 687/2015 and NR 786/2017. The authors highlighted that NR 687/2015 allowed that DG could include condominiums, consortiums, cooperatives, and remote auto-consumption. They conclude that the NR 482/2012 was a big step for the decentralized sector because it allowed consumers to generate their electric energy, contributed to reducing market barriers for DG, and addressed issues related to public intervention in the energy sector.

3.1.4. Solar cities and islands

The term smart city is multidisciplinary, generic, and vastly discussed in the literature. It is typically associated with information and communication technologies (ICT), internet of things (IoT), artificial intelligence (AI), social and environmental sustainability, economic growth, and celerity.

Caragliu et al. (2009) pointed out six general aspects in smart cities: economy, mobility, environment, people, living, and governance. It is understood that smart cities with clear socio-environmental visions can also be seen as a sustainable and livable city (Zygiaris, 2012).

Calvillo et al. (2016) defined smart cities as sustainable and efficient cities that offer high living standards and appropriate resources management. In a way, they referred to urban infrastructures that promote environmental protection and reduction of CO_2 emissions, in conjunction with growth and sustainability in social, economic, and technology dimensions.

See Albino et al. (2018) for smart cities definitions, dimensions, and initiatives, and Camero and Alba (2019) for a bibliographic review.

The idea of a solar city is to make the most of the solar resources to generate thermal and photovoltaic energy. Although it is a recent topic in literature, it is expected that a city becomes a solar city when there is widespread development of photovoltaic systems on suitable rooftops (Byrne et al. 2015) and energy management improvement through deployment of a smart grid (Wan et al., 2015).

Smart grids are autonomous bidirectional power grid infrastructures controlled by artificial intelligence that promote efficiency, communication, automation, and security (Gungor et al., 2011). Based on smart metering data and communication networks among all users of the grid, the smart grids controllers reduce impacts from variations in customer substations, generation, transmission, and distribution (Kabalci, 2016). In this manner, the IoT represents a key role in smart grids management as it enables fast communication between consumers' smart meters and device power controllers. For example, IoT is applied to identify consumption house patterns, manage smart home devices, and recharge electrical vehicles (Reka and Dragicevic, 2018).

Di Silvestre et al. (2018) paid attention to a recent concept in energy management, the three D's: decarbonization, digitalization, and decentralization. The digitalization part is represented by the internet of things (IoT) and the 4th Industrial revolution modern changes, which are improving communication, business models, and transactions. The decentralized aspect surged due to the increasing customer participation and new strategies of power production distribution. Decarbonization is related to the reduction in CO_2 emissions. Altogether they represent a disruptive phenomenon, which are considered by the authors as the main drivers of substantial transformations in our society.

3.1.4.1. Solar and smart islands

In the context of renewable energy in islands, it is crucial to analyze each island considering their particular local situation regarding the energy use and available resources. Samsø Island, in Denmark, is a great example of pursuing a 100% renewable transitions until 2030 (Nielsen and Jørgensen, 2015; Jantzen and Kristensen, 2018). Other articles that researched the use of renewable energy for remote islands are Liu et al. (2018) in the Maldives, Selosse et al. (2018) in Reunion Island, France, Eras-Almeida et al. (2020) in Galapagos Island and Curto et al. (2020) in Lampedusa Island, Italy.

Sperling (2017) stressed out that many authors focused on the end-results of renewable transitions, but few described the practices and conditions to achieve that. Therefore, the authors evaluated the internal and external factors that enabled the transaction in Samsø Island. They concluded that the main external conditions were governmental assistance with technology, expertise, and process support. In the internal context, the main factors that favored the renewable energy transaction were the community engagement and sense of cooperation and responsibility, individual entrepreneurship, and distribution network.

In a review paper of renewable energy for islands, Kuang et al. (2016) pointed out that technological advances permitted higher participation of renewable energy sources in islands power supply, and because of long distances and high costs of submarine transmission cables, usually there is no connection with the continent or adjacent islands, which affect the grid stability and reliability. Additionally, they detailed aspects that sustain renewable transactions: energy storage techniques, hybrid renewable energy system, microgrid, demand-side management, distributed generation, and smart grid.

Blechinger et al. (2016) argued that renewable energy in small islands must be studied because of the high dependency on the importation of costly fossil fuel and abundant solar and wind energy resources. Moreover, due to their limited population and size, the authors claimed that there is a simplification in the management of technical and political approaches to increase renewable sources. Also, they highlighted that small islands serve as inspiring small-scale examples to replicate in larger areas.

Curto et al. (2019) also mentioned that most small islands are powered by old diesel generators, although there are remarkable advances in renewable energy technologies and reduction of costs. The deployment of renewable energy sources in those cases could address some important issues, such as fossil fuel reliance, pollutant emission, and high electricity costs.

Particularly in a small extension oceanic island case, where potable water is scarce and water supply faces growing anthropic pressure, it is important to observe the relationship between desalination water and energy supply. Bilton et al. (2011) presented a general process that evaluated the feasibility of PV-powered reverse osmosis in remote areas, based on a cost comparison between desalinated water produced by conventional diesel power and photovoltaic. Mentis et al. (2015) also worked on a tool to improve the design and sizing of desalination systems integrated with renewable energy sources. They found out that the proposed approach is feasible in the majority of the remote areas analyzed. In a similar context, Wright et al. (2014) demonstrated through a GIS analysis (that combined water scarcity, salinity, and solar resource maps) in India that GIS is an essential approach for supporting decision-making processes. Also, within the view of feasibility analysis, the authors compared the costs of water desalination systems and salinity range to determine the most suitable integrated solution for specific locations. It is worth noting that their research considered salt groundwater in continental India, which has a distinguished socio-environment condition when compared to ocean islands, but still, they are isolated remote areas, and the population size of a median Indian village range from 2000 to 5000, similar to FNI.

More recently, Liu et al. (2018) investigated the feasibility to integrate water and energy supply systems in remote islands and proposed a framework for an interconnected system in Maldives Islands. In the same context, Mehrjerdi (2020) conducted a study for an isolated island, associating three different types of desalination plants (reverse osmosis (RO), multi-stage flash (MSF), and multi-effect distillation (MED)) supplied by a hybrid renewable energy system made of PV-wind, which is backed up by a battery energy storage system and a diesel generator. The store system supply power in hours of low energy production and store excess energy in hours of high production. The diesel generator is employed in case of emergencies and network instability. The author compared simulations between methods of desalination and concluded that RO presented better results than CSP methods, in terms of costs and reliability. With a different view than the previous author, Wang et al. (2020) also researched the integration of CSP and desalination plants but argued that their proposed system, where there is an integration between CSP+MED with renewable systems and RO, has better cost-effectiveness in comparison with other state-of-art systems when dealing with areas with high abundant renewable energy resources and high fuel costs. The three papers cited here highlighted that the integration of desalination plants and renewable power supply can potentially reduce energy costs and pollutant emissions, and the proposed nexus between water and renewable energy is a future trend for remote islands.

Again, particularly in a small extension oceanic island case, where there is high pressure on land use, and occupation and land resources are scarce, it is important to consider more than one use for the same area. For example, installing PV power systems on parking lots, which can reduce charging costs of electric vehicles, or combining PV generation and agricultural activities, which could raise food supply and reduce electricity and food prices for residents.

In the context of agrivoltaics, which is the combination of PV and agriculture, Sekiyama and Nagashima (2019) presented and demonstrated successful results of a stilt-mounted agrivoltaic system associated with a corn plantation, which is known as a typical shade-intolerant crop. In Saint Joseph, Reunion Island, similar to FNI in many aspects, there is an example of a real case study of a photovoltaic greenhouse with an annual production of 1.96 GWh (Scognamiglio et al., 2014). In the case of solar parking lots, Nunes et al. (2016) highlighted that although they are not yet economically viable, they offer great environmental and technical benefits.

Within the frame of GIS context, Doorga et al. (2019) modeled in high spatial and temporal resolution the PV potential of Mauritius Island to optimize the location of solar plants, through GIS Multiple Criteria Decision Making (MCDM) analysis integrated to Analytical Hierarchy Process (AHP). Likewise, Suh and Brownson (2016) studied the solar plants' suitability in Ulleung Island, Korea, using MCDM coupled to fuzzy methodology to normalize each spatial factor adopted in MCDM.

The method proposed in the present dissertation differs from the papers previously cited at the spatial resolution, the types of PV systems considered in the study, and the framework of decision of PV systems location. Their analyses were limited to utility-scale solar plants, Suh and Brownson (2016) adopted a digital elevation model (DEM) with grids of 5 x 5 m and Doorga et al. (2019) with 10 x 10 m, while in this present research, it was produced a DEM with grids of 50 x 50 cm. The gains provided by this ultra-high spatial resolution are in considering the PV potential analysis not only in open areas, where PV plants are installed, but also in rooftops, where individual and decentralized systems are analyzed. In the literature, no study associated the ultra-high spatial resolution and PV potential in an island environment.

3.2 UAV Photogrammetry

3.2.1. State of the art

The American Society for Photogrammetry and Remote Sensing (ASPRS) defines photogrammetry as “the art, science, and technology of obtaining reliable information about physical objects and the environment through processes of recording, measuring, and interpreting photographic images and patterns of recorded radiant electromagnetic energy and other phenomena” (Wolf et al., 2014). In that way, photogrammetry techniques encompass digital imagery, radiated acoustical energy patterns, laser ranging measurements, and magnetic phenomena. The remote sensing instruments used to acquire photos, laser, and irradiance data photos can be integrated to sensors onboard of manned or unmanned aerial vehicles, orbital satellites, or terrestrial cameras (Wolf et al., 2014).

Photogrammetry is separated into two main areas: metric and interpretative. Metric photogrammetry works with quantitative measurements and geographic location of points, which in turn provides information on distances, angles, areas, volumes, elevations, and sizes and shapes of objects. Interpretative photogrammetry attends to the recognition and identification of objects and their significance to the surrounding environment (Wolf et al., 2014).

The metric photogrammetric surveys are performed to produce orthophotos, digital elevation models, triangular meshes, cloud points, and textured 3D models, where geometric measurements can be done. While the application of interpretative photogrammetry focuses on algorithms of digital image processing segmentation and classification of objects and is typically associated with other RS sensors, like multi and hyperspectral.

The photogrammetry basic principle is inspired on the stereographic vision phenomena, which allows humans to perceive depth from two different points of view or from a single observing point when the observer or the target is moving

(Ullman, 1979). In that way, a collection of bidimensional photos can reproduce a virtual tridimensional world, whose structure is represented by a point cloud.

Photogrammetry was first published by the German architect Albrecht Meydenbauer, in an article called *“Die Photogrammetrie”* (“The photogrammetry” in English), in 1867. The photogrammetrist and his colleagues founded the Royal Prussian Photogrammetric Institution to research the field and preserve the architectural and cultural monuments of the German Empire (Albertz, 2002). However, the approach is marked by constant technological and methodological innovations that made it more flexible and effective. With the consolidation of airplanes, sensors, and stereo plotters during World War I, the analog photogrammetry was recognized as an efficient surveying and mapping method. Although the mathematical fundamentals were well known at the time, it was only after 1950, with the arrival of computers and AI, that analytical photogrammetry established itself, improving the precision of aerial triangulation by a factor of ten. Then, with the advent of digital images, the current digital photogrammetry appears (Schenk, 2005).

This technological progress kept evolving and today we have well-established UAVs, sensors, computers, and algorithms that put photogrammetry as the main approach to collect and compute spatial data. It is not an exaggeration to affirm that almost all maps produced since World War II were produced by photogrammetry. Historically, the advances in photogrammetry were essential for pushing forward artificial intelligence and computers, spatial programs, inertial sensors, digital sensors, among others current technologies and projects.

The term *drone* is used to represent unmanned aerial vehicles. More technical terminologies are used in this purpose too, such as small unmanned aircraft systems (SUAS) or remotely piloted aircraft (RPA). In the present research, the term UAV is adopted due to its popularity in scientific research and technical reports.

In the last decade or so, there has been a great advance in the science of photogrammetry. The flexibility, safety, low cost, and simplicity of UAVs equipped with sensors, and the robustness and efficiency of computer vision algorithms are responsible for this rapid scientific development. The enhancement of the algorithms Structure from Motion (SfM) and MultiView Stereo (MVS) are the key elements behind the current photogrammetric computation.

In literature, some books and articles review or take the photogrammetry SfM-MVS as the main subject: Westoby et al. (2012), Turner et al. (2012), Colomina and Molina (2014), Nex and Remondino (2014), Pajares (2015), Biljecki et al. (2015), Carrivick et al. (2016), Agüera-Vega et al. (2017), James et al. (2017), Singh and Frazer (2018), Jeziorska (2019), Iglhaut et al. (2019), Yao et al. (2019), among others.

The use of UAVs and almost fully automated SfM-MVS workflow facilitates the production of high spatial resolution 3D point clouds, DEMs, and orthophotos of large areas, which were previously produced by costly and more complex LiDAR surveys and manned aerial missions (Wallace et al., 2016).

It is important to mention that LiDAR surveys perform a direct measurement of the objects, by actively emitting and receiving laser pulses that physically hit the object's surface. The cloud point in SfM-MVS photogrammetry is originated from RGB pixel values belonging to a set of images, while the ones from LiDAR surveys are derived from the interpretation of pulses reflective values and waveforms. However, ultimately, both techniques belong to the field of photogrammetry.

The techniques can be considered concurrent since both are capable of generating point clouds, or complementary when there is an integration of RGB data from the photographs with elevation from LiDAR (Zaragoza et al., 2017).

Turner et al. (2012) highlighted some technical differences between photogrammetric surveys lead by traditional manned aerial vehicles and UAV: i) UAV flight lines show greater variations in overlap and intersections; ii) UAV images show greater variations in rotation and translation angles, light conditions, and spatial resolution; iii) exterior and interior orientation parameters from UAV imagery are unstable, unknown, or, if measured, are likely to be inaccurate. In the same context, Westoby et al. (2012) pointed out a fundamental difference between UAV SfM-MVS and conventional photogrammetry: “the geometry of the scene, camera positions, and orientation are solved automatically without the need to specify a priori, a network of targets which have known 3-D positions. Instead, these are solved simultaneously using a highly redundant, iterative bundle adjustment procedure, based on a database of features automatically extracted from a set of multiple overlapping images”.

There are two UAV basic categories: fixed-wing and multi-rotor. Both categories have unique characteristics that give them advantages and disadvantages, which depends upon the context of the application. For example, Jeziorska (2019) indicated that multi-rotors land and take off vertically on the ground, while fixed wings need a manual or mechanical launching and a smooth and flat area to land. The author observed that rotary wings gained market popularity over the fixed-wing due to its lower price and ease of use. Boon et al. (2017) compared both types of UAV in the context of environmental mapping and concluded that for vegetation and gully erosion modeling, multi-rotor is most suitable because there is less distortion in aerial images, although fixed wing delivers data with sufficiently quality. For wetland slopes and contour mapping, both can be applied without noticing differences.

Colomina and Molina (2014) described several studies that adopted fixed or multi-rotor wings, where one can think that the output data quality of photogrammetric surveys depends more upon the UAV model, the surveyors' experience, the environment mapped, and the scale and application of the survey, than on the type of UAV used, if fixed-wing or multi-rotor type.

The UAV photogrammetric approach has been used for many purposes and applied on different scales. Pajares (2015) and Yao et al. (2019) argued that the UAV photogrammetry capacity for ultra-high spatial and temporal resolutions increases the range of solutions and opportunities for remote sensing applications. Moreover, the quality and quantity of spatial data lead the decision-making process to be more accurate and quicker.

Regarding the georeferencing and positional accuracy in UAV SfM-MVS photogrammetry surveys, worth note that most consumer-grade UAVs have a navigational GNSS receptor (NAVGNSS) for image geotagging, with a positional accuracy about 10 m, which is insufficient for some applications. To improve the georeferencing of the UAV SfM-MVS photogrammetric model to a few cm-levels, surveyors add ground control points (GCP) typically measured by dual-frequency (L1/L2) cm-level GNSS receivers.

The positional method *Real-Time Kinematic* (RTK) is extensively adopted for the GCP georeferencing (Forlani et al., 2018), yet *Post-Processing Kinematic* (PPK) (Fazeli et al. 2016) or NTRIP-RTK (Haas et al., 2016) are also feasible alternatives. More recently, L1/L2 GNSS receivers fixed onboard UAVs are used to direct georeferencing aerial photos to few cm-level positional accuracies (Forlani et al., 2018; Tomaštík et al., 2019; Ekaso et al., 2020). Padró et al. (2019) compared four georeferencing approaches: onboard NAVGNSS, onboard PPK L1/L2 with the base distance 4 km, onboard PPK L1/L2 with the base inside flight area, and traditional L1/L2 GCP. The authors reached positional accuracies at 1.837 m, 0.443 m, 0.062 m, and 0.039 m, respectively.

A UAV photogrammetry has two main phases: data collection and data processing. Before going to fieldwork to collect the GCP coordinates and aerial images, it is fundamental to have in mind the expected quality of the survey. It starts with the evaluation of the area of interest and the definition of photogrammetric flight parameters (areas for takeoff and landing, flight height, overlapping percentage, final spatial resolution) and GCP scheme (places for base station, quantity, and spatial distribution). After acquiring field data, computer vision algorithms are employed to detect matching points in overlapping photos, which are used to compute georeferenced cloud point, DEM and orthophoto.

The SfM-MVS main role is to compute a 3D model, e. g., a point cloud from a set of sufficiently overlapped photos, which is further processed into a dense point cloud, mesh, DEM, and ultimately, in an orthophoto (Figure 7).

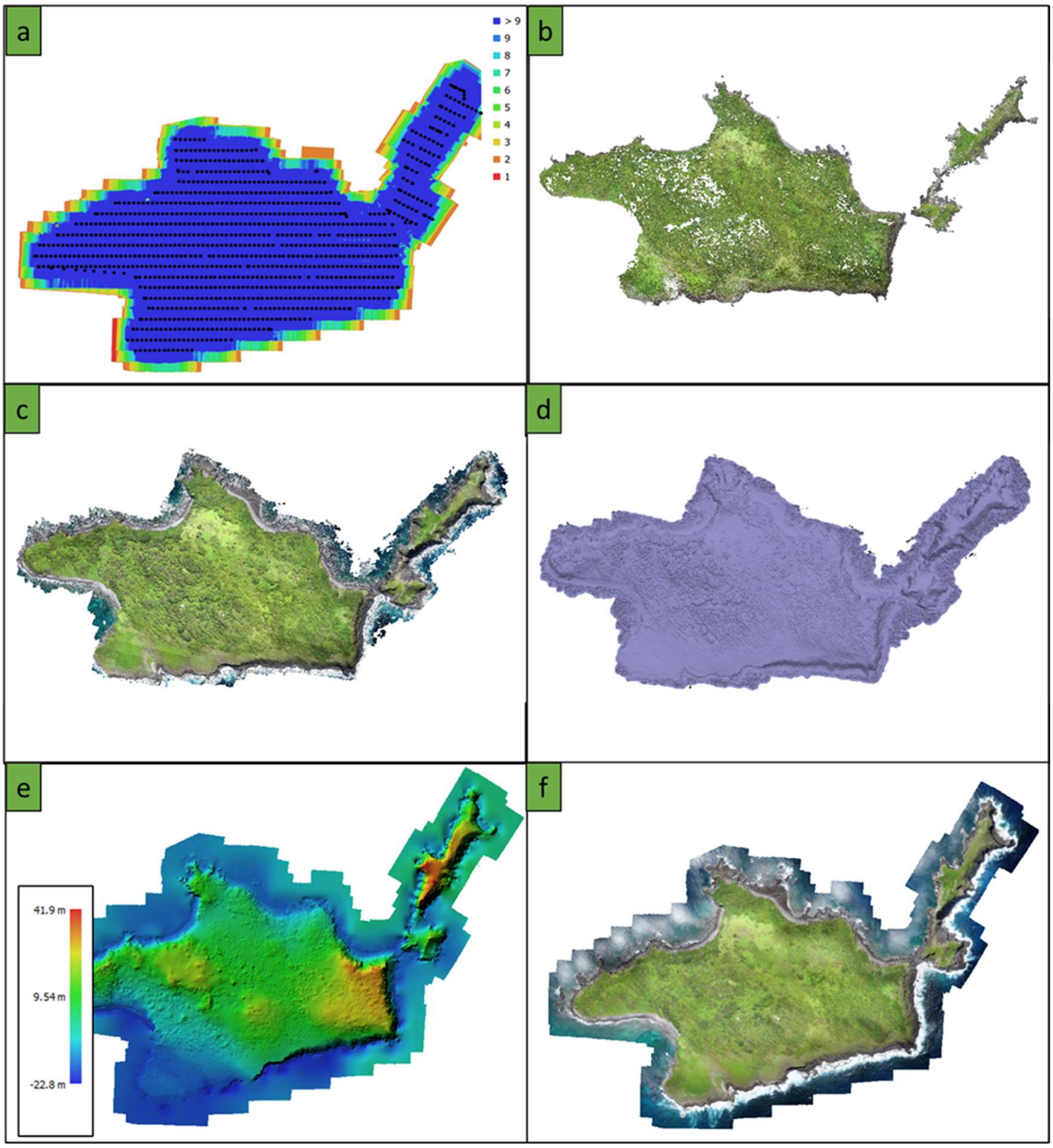

Figure 7. An example of image processing photogrammetric workflow from Ilha da Rata, an adjacent island from the Archipelago of Fernando de Noronha. (A) aerial photo coordinates and overlap; (B) sparse point cloud; (C) dense point cloud; (D) mesh; (E) DSM; (F) orthophoto.

3.2.2. Structure from Motion and algorithms in digital photogrammetry processing

As the name itself, SfM stands for a structure derived from a moving sensor. The algorithm is responsible for the stereo plotting proceedings in modern digital photogrammetry processing. SfM aims to produce a sparse cloud and determine the location of matching features in a set of photos, taking from different perspectives (Westoby et al., 2012).

In SfM, the photogrammetric process of Bundle Block Adjustment (BBA) begins with an image recognition algorithm, for example, the scale-invariant feature transform (SIFT), that identifies and matches common features that are visible in a set of overlapped images (Lowe, 2004). In SIFT, these features are written as 3D vectors (represented by a unique feature descriptor) that are invariant to the scale and rotation of the images and are represented by a point cloud. The matched points in a set of photos are named *keypoints*, and they are responsible for the scene geometry reconstruction done by SfM (Carrivick et al., 2016).

The SIFT algorithm is based on a digital recognition processing of multiscale image brightness and color gradient analysis. The main advantage of the first one is to deal with mixed image resolution (common in UAV photogrammetric surveys), and of the second is to use colors gradient instead of pixel values, which facilitate differentiation of targets and their backgrounds (Fonstad et al., 2013).

After the recognition and description of features in overlapped photos, the SfM is responsible for calculating camera location and orientation based on the positions of the matched features. At the same time, SfM constructs a sparse 3D point cloud composed of the 3D vectors written by SIFT (Carrivick et al., 2016). Figure 8 illustrates an SfM scene geometry reconstruction.

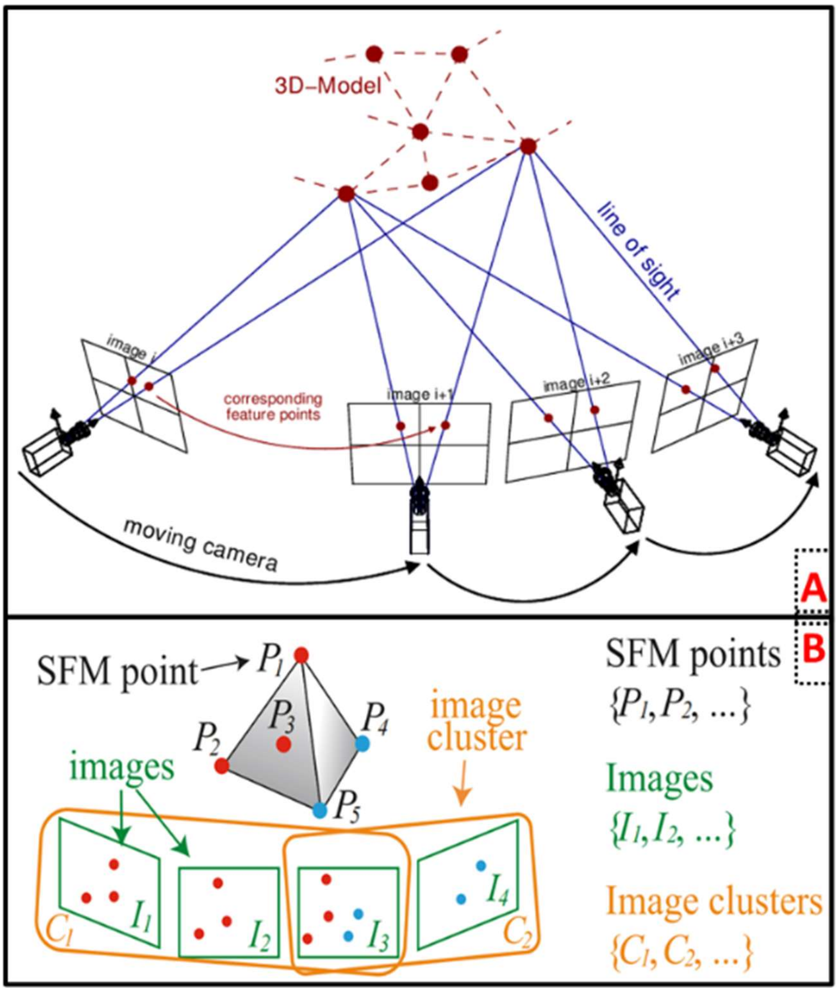

Figure 8. A: Demonstration of Structure from Motion process of 3D model reconstruction. Source: Sweeney (2016). B: Demonstration of MultiView Stereo process of image clustering. Source: Furukawa et al. (2010).

The abilities to establish thresholds in computation calculus and filtering invalid 3D reconstruction are essential to deal with a large number of images and produce high-quality photogrammetric products using SfM workflow (Remondino et al., 2017; Carrivick et al., 2016).

To achieve higher quality in scene reconstruction, a multiview stereopsis (MVS) technique is applied to densify the sparse cloud. According to Furukawa and Ponce (2009), the first step is to organize the data into a manageable size by doing an image clustering based on their location (Figure 9). Then, the tie matched in SfM are used to generate new matched points, that are repeatedly expanded to neighboring pixels to find new correspondents' points. In that way, the dense point cloud is generated by expanding the search radius and finding new matches around the sparse cloud points.

The next steps consist of a derivation and interpolation of the dense cloud to compute the mesh, DEM, and orthophoto.

Finally, the entire process of modern photogrammetry can be partitioned in three main algorithms or steps: image matching, block bundle adjustment, and multiview stereopsis (Furukawa and Ponce, 2009).

Iglhaut et al. (2019) elaborated two figures demonstrating the SfM-MVS workflow. The first (Figure 9) is a scheme of algorithms used on the three main stages (SIFT, SfM, and MVS) and the second (Figure 10) is a visual demonstration of results on each stage. The authors also mention that the main advantage of automation of the photogrammetric process is the unnecessary expertise to operate fully automated black-box software, but it can also be a disadvantage because there are less data quality control and error detection.

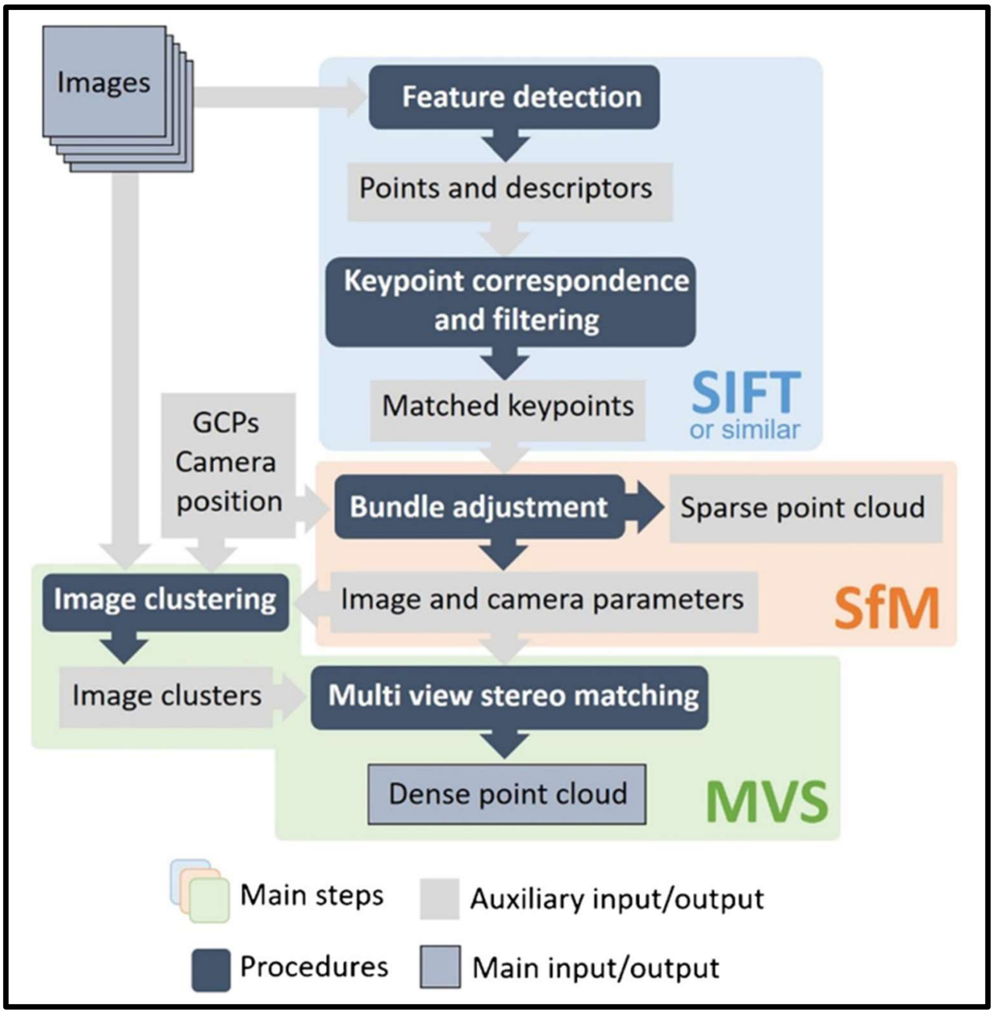

Figure 9. Schematic workflow of the SfM-MVS process to obtain a dense point cloud. Source: Iglhaut et al. (2019).

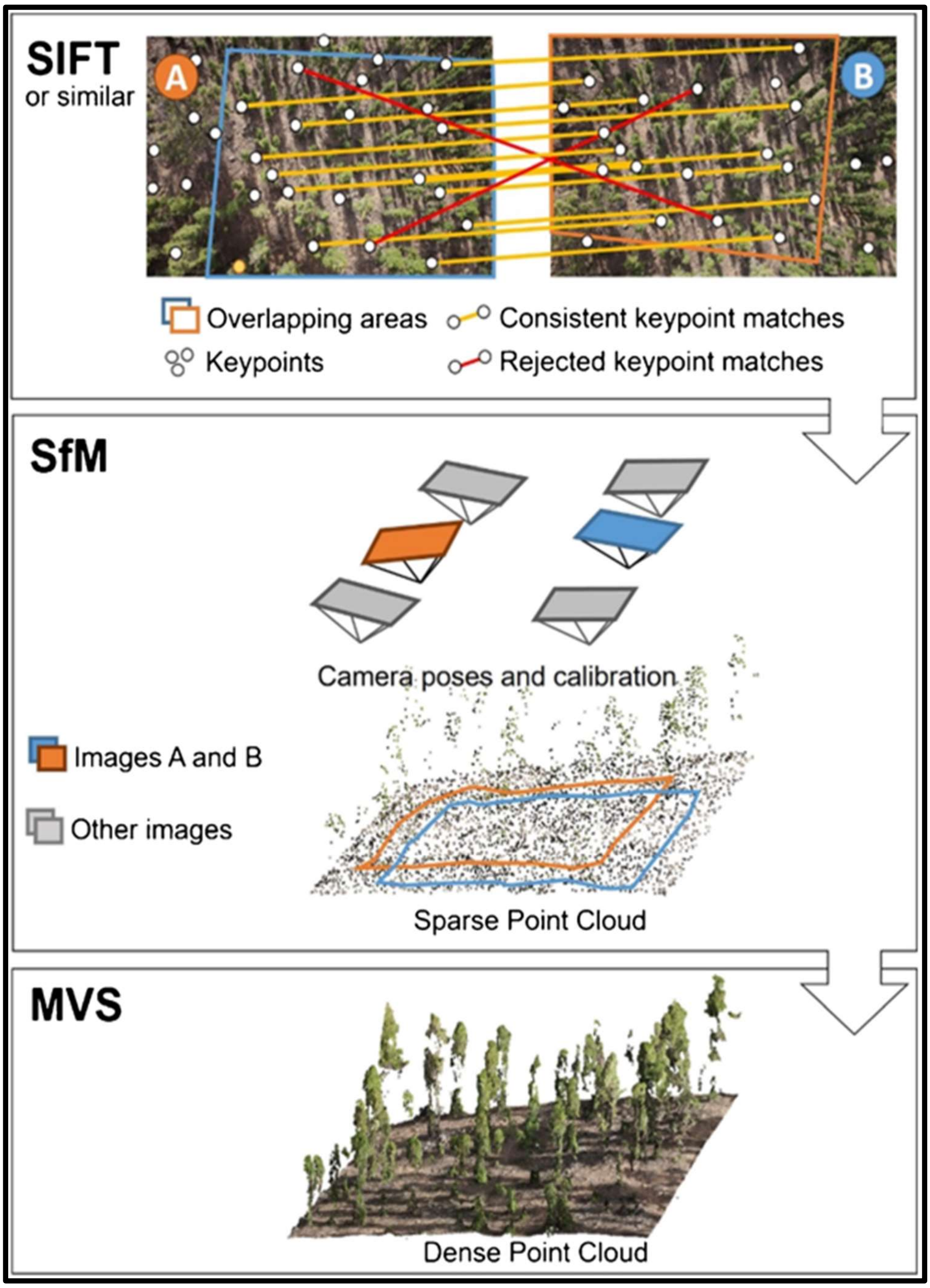

Figure 10. The schematic illustrated workflow of the three main stages SIFT, SfM, and MVS. The process to obtain a dense point cloud. Source: Iglhaut et al. (2019).

3.2.2.1. Photogrammetric data processing in Agisoft Metashape 1.6

The overview provided by the User Manual Agisoft LCC (2019) states a brief description of the program: “Agisoft Metashape is an advanced image-based 3D modeling solution aimed at creating professional quality 3D content from still images. Based on the latest multi-view 3D reconstruction technology, it operates with arbitrary images and is efficient in both controlled and uncontrolled conditions. Photos can be taken from any position, providing that the object to be reconstructed is visible on at least two photos. Both image alignment and 3D model reconstruction are fully automated." Although it did not mention the mapping purposes, it is one of the most popular tools for processing UAV SfM-MVS photogrammetric surveys.

Typical steps of the workflow offered by Agisoft Metashape 1.6 are: load photos, align photos, perform white balance correction and gradual selection of undesired points, align GCPs, build dense point clouds, build 3D polygonal mesh, build DEM, build orthophoto (Agisoft LCC, 2019).

The alignment step is performed by SfM and considers several *keypoints* to search for matching features in the set of images. In Agisoft LCC (2019) terminologies, *keypoints* are features of interest, typically texturized and with high contrast, from which can be easily recognizable on overlapped photos. When keypoints are matched on different cameras, they are assigned as a tie point (Agisoft LCC, 2019).

Once the set of photos were aligned and sparse cloud generated, it is recommended three important steps executed in sequence: calibration of white balance color of points, gradual selection and exclusion of unsatisfactory points, and optimization of camera alignment (USGS, 2017).

The step of color correction is performed to compensate for brightness and to adjust the white balance in images set. Along with that, a gradual selection of sparse cloud points is operated to reduce error and BBA optimization. It is recommended that the threshold adopted for reconstruction uncertainty is set to level 10, for projection accuracy level 3, and reprojection error level 0.3 (USGS, 2017). The software does not inform the measurement units for the thresholds.

The step of optimization of camera alignment is based on the known reference coordinates enhanced by GCP. The procedure removes non-linear deformations and improved georeferencing accuracy. It is executed by re-estimating both camera parameters and constructed sparse cloud. Ultimately, it optimized interior and exterior orientation (Agisoft LCC, 2019).

After the refinement of the sparse cloud, the generation of the dense cloud is the next step. For that, the program calculates a depth map for every photo, which is then filtered to remove noisy and badly focused images. As recommended in aerial mapping, the filtering mode must be set to aggressive, because there is no need to model meaningfully small objects (Agisoft LCC, 2019).

In sequence, the mesh is constructed based on a linear interpolation method that constructs a polygonal mesh that smoothed the high variability of the dense cloud. It worth highlighting that the solar irradiation model based on a smoothed DSM (originated from a mesh) will be less noisy than if it were used a DSM created directly by the dense cloud - although the last one is more accurate. As recommended by Agisoft LCC (2019), the surface type for aerial mapping is the height field, which is the most efficient option to work with planar surfaces, such as terrains and roofs. The interpolation process is check-marked when the process fills possible holes that originated from bad matching in SfM and errors in cloud densification.

After that, based on the inverse distance weighting (IDW) method, the elevation data of the polygonal mesh is interpolated into a regular raster grid to generate the DSM with a default spatial resolution (Agisoft LCC, 2019).

The process of orthophoto generation is done by projecting and mosaicking undistorted orthogonalized photos onto the mesh surface (Agisoft LCC, 2019).

3.2.3. Photogrammetric data collection

The two basic data of photogrammetric surveys are aerial photos and GCPs coordinates. Typically, photos are collected by RGB cameras onboard UAVs and GCPs georeferenced by L1/L2 GNSS receivers. As in many other computational techniques, it is expected that if the inputs are somehow low quality, the output will also have low quality.

3.2.3.1. Aerial images

In that way, it is important to attend to some aspects during photo collection, like lighting conditions, occlusions, final spatial resolution, overlapping percentage, view angles, surface contrast, surface pattern, among others (Gienko and Terry, 2014). For example, the SIFT algorithm matches more correspondent points when searching in a stony or heterogeneous soil surface than in a sandy or icy homogeneous and low contrast surface (Carrivick et al., 2016). Also, surfaces that are in movement during image collection, like vehicles, winding leaves and waving water, will cause optical distortions and reflections that propagate error in SIFT feature matching and, in consequence, in SfM matching procedures (Casella et al., 2016).

The aerial photo scales are determined by the geometric relationship in Equation 1 and 2. The flight height parameter defines the scale of photos and ultimately, the orthophoto spatial resolution. Another basic concept, which is the stereoscopic coverage or the frontal and lateral overlapping between photos are demonstrated in Figure 11. It is expected that an object covered by more photos, i. e., higher overlapping percentage, will have a better 3D reconstruction (Carrivick et al., 2016). The Ground Sample Distance (GSD), i. e., the size of the pixel, is also employed to indicate spatial resolution.

Eq. 1 Scale = Photo Distance / Ground Distance

Eq. 2 Scale = Focal Length / Altitude Above Ground Level

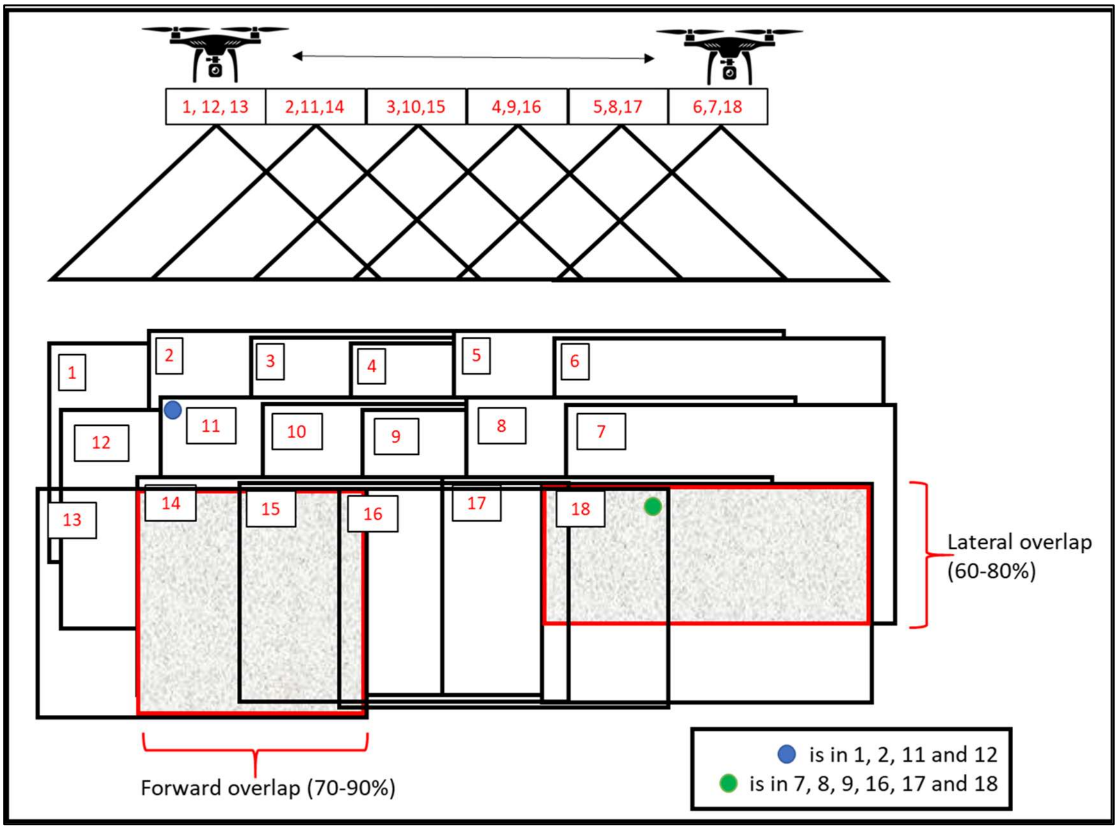

Figure 11. Flight pattern in a typical UAV SfM-MVS photogrammetry survey. The photographs are taken with a forward and lateral overlap to feed the SIFT algorithm, where matching points in different photos are identified.

The NAVGNSS, compass and IMU systems onboard a UAV are essential for geotagging photos and to control the automatic pilot program that makes the UAV follow a photogrammetric flight pattern. There are several applications available for smartphones and tablets for mission planning, like DroneDeploy, DJI Ground Station, MapPilot, etc. The programs allow users to estimate final spatial resolution and simultaneously set up flight path, direction, altitude, speed, overlap configuration, gimbal pitch angle, return to home options, and essential camera parameters.

The UAV ability to execute missions with high overlapping percentage and low altitudes will result in digital maps with an ultra-high spatial resolution (UHSR) under one decimeter (Yao et al. 2019) and up to one centimeter (Agüera-Vega et al., 2017).

Sanz-Ablanedo et al. (2018) affirmed that homogeneous coverage overlapping and constant altitude above ground will result in photogrammetric products with less geometric distortion. Figure 12 illustrates the influences that variability on the altitude AGL have in overlapping parameters and the SIFT stitch process.

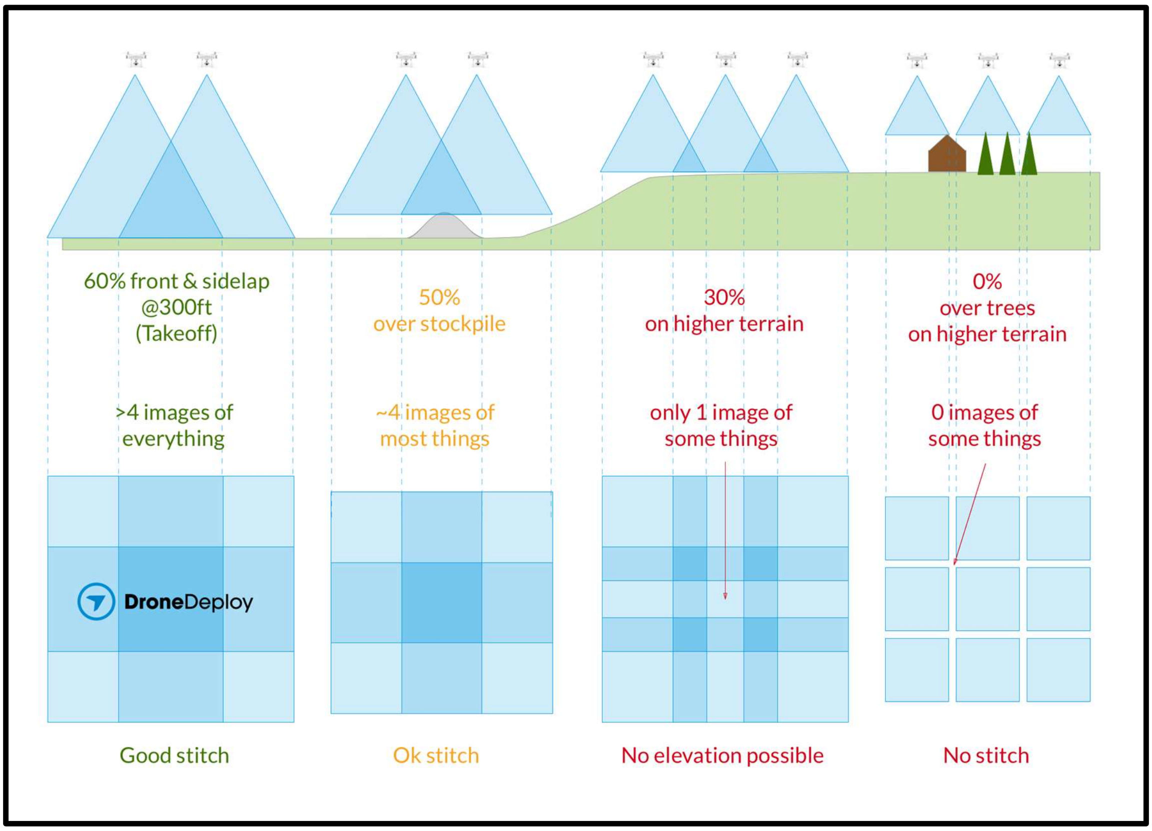

Figure 12. Percentage of overlapping images when varying elevation of terrain, trees, and high buildings. Source: DroneDeploy (2019).

Singh and Frazier (2018) found out in their meta-analysis and review on UAV imagery application that most of the authors consider at least 75% in the forward overlap and high variability in the side overlap, from 20 to 90%. Yet, they recommended percentages above 70% on the forward overlap and 60% on side overlap, it will depend on the final spatial resolution and the type of terrain and surface surveyed. Jeziorska (2019) noted that forward or side overlap must be at least 60-80%.

Manfreda et al. (2019) suggested that the combination of two flights, one with nadir perspective (perpendicular to the ground) and a complimentary with a 20° angle tilted camera, improve the overall accuracy of the 3D model and vertical precision. Furthermore, Leitão et al. (2016) assessed four different mapping variables: flight altitude, image overlapping, camera pitch, and weather conditions. The low altitude flight, with at least 60% frontal overlap, in overcast weather conditions are preferable for high-quality DEMs. The authors considered the technology very robust to these variations and concluded that UAV photogrammetry competes with traditional LiDAR DEMs due to its flexibility and accuracy.

When setting up flight parameters and mission, it is important to look for an optimum equilibrium between final product quality and efficient field operation parameters, such as the number of photos acquired, flight length and duration, battery power supply, processing time and data storage.

3.2.3.1. Ground Control Points

As previously stated, GCPs are used to enhance the georeferencing of UAV photogrammetric maps. A survey must contemplate at least three GCP distributed in a triangular shape but requires more if it is needed better positional accuracy. The GCPs must have enough size and contrast to be identified on photos during the GCP photo targeting procedure. When adopting homogeneous GCP distribution and sufficient number of GCPs, authors achieved positional accuracies of less than 10 cm (Lucieer et al., 2014; James et al., 2017; Sanz-Ablanedo et al., 2018).

James et al. (2017) highlighted that the distribution and density of GCP on the area of interest are planned based on the required accuracy, network geometry, and quality of images.

Villanueva and Blanco (2019) pointed out that the three main propagators of error in GCP operations are distribution, quantity, and inter distance between GCPs. The authors tested all of them in a quarry-site area and indicated that a greater distribution of GCPs placement will result in fewer errors, and in accordance, a concentrated distribution of GCPs results in higher errors. They also observed an inverse relationship between the quantity of GCPs and Root Mean Square Error (RMSE), up to a certain limit number of GCP placed. Finally, in the inter distance test, the authors conclude that the higher error group of GCP has also a higher inter distance between GCPs. Similarly, Manfreda et al. (2019) also evaluated the GCP quantity and placement in UAV photogrammetry. They demonstrated that a well-distributed number of GCPs placed in a small inter distance is the best approach to increase overall accuracy. The researchers cited in this paragraph did not consider the scenario of GCP and positional assessment in extensive areas, like FNI with more than 2000 ha.

Within a more quantitative view, Sanz-Ablanedo et al. (2018) performed a comparative study combining multiple combinations of GCPs in photogrammetric surveys in an area of 1200 ha. They conclude that if few GCPs were used, the RMSE of checkpoints will be around 5 times the GSD, but if an appropriate number of GCPs were employed, this ratio could be up to 2 times. Furthermore, according to the authors, if independent checkpoints data are not available, the real accuracy can be estimated by multiplying the RMSE of GCPs by 3 (when a high number of GCPs is used) or 4-8 (when few GCPs are used). They suggest that large projects can achieve high accuracy when using >3 GCP per 100 photos in the area of interest.

3.2.4. UAV SfM-MVS Photogrammetry Applications

The control of spatial and temporal resolution offered by SfM-MVS photogrammetry and UAVs are now a key changing point in GIS and remote sensing applications. There are new perspectives because advances in hardware and software have added more quality to cartographic products (point clouds, DEMs, and orthophotos) and safety, accessibility, simplicity, and flexibility to the photogrammetric process.

Not only visible range sensors can onboard a UAV, but multispectral and hyperspectral sensors too. In that way, infrared spectral bands are measured and analyzed to identify, for example, vegetation stresses, water content, and thermal variations, which in some cases, can be a hard effort, sluggish and expensive task (Jeziorska, 2019). These portable and cutting edge technology sensors are being applied to precision agriculture (Zhang and Kovacs, 2012; Baluja et al., 2012; Honkavaara et al., 2013; Bendig et al., 2015; Gago et al., 2015; Maes and Steppe, 2019), forest management (Anderson and Gaston, 2013; Lisein et al., 2013; Zarco-Tejada et al., 2014; Sankey et al., 2017), fire management (Yuan et al., 2015; McKenna et al., 2017), damage inspection of photovoltaic systems (Tsanakas et al., 2017; Gallardo-Saavedra et al., 2018), among others. Although multispectral sensors are not used in the present case study of FNI, the papers cited in this paragraph demonstrated that multispectral sensors have a great role in GIS analysis and have the potential for further research.

Using RGB sensors, there are applications in landslide measurements (Niethammer et al., 2012; Turner et al., 2015), superficial hydrological modeling (Shaad et al., 2016; Hashemi-Beni et al., 2018), urban planning, territorial management, environmental works in forest and coastal areas, among others.

In the matter of urban planning, UHSR orthophoto and DEM allow automatic classifications and vectorization of semantic data to develop a basic geodatabase, such as thematic maps, properties boundaries, buildings, green parks, etc, essentials for decision support in city management (Crommelinck et al., 2016), although it needs further development of algorithms. Furthermore, elevation data supports visibility analysis and estimation of population, which is crucial data for several statistical and spatial analysis that directly involves demography (Biljecki et al., 2015).

In territorial management, particularly in developing countries with low cadastral coverage, orthophotos are used for cadastral mapping and developing a geographic database. Cadastral maps are instruments that provide basic information and precise location of lands, properties, and buildings, being essential for the documentation of land rights, land taxation, control urban growth, infrastructure city planning, compose geodatabase, and geostatistics analysis (Crommelinck et al., 2016). For example, the cadastral mapping based on UAV orthophoto was applied in Indonesia (Ramadhani et al., 2018), Namibia (Mumbone et al., 2015), Rwanda (Koeva et al., 2018), Brazil (Fonseca Neto et al., 2017), and many developed country cities. It is important to note that the land boundaries must be physical and visualized in orthophotos to manually vectorize or perform automatic classification of boundaries (Fetai et al., 2019; Xia et al., 2019).

According to Crommelinck et al. (2016), the increasing popularity of UAVs for cadastral mapping is justified by their flexibility to work on urban and rural environments, lower cost, and final products with higher spatial resolution than traditional RS methods. They also highlighted the high demand in developing countries for spatial information for new cadastral mapping, and in developed countries, for updating it.

In the case of conservation works in protected areas, Koh and Wich (2012) developed a UAV prototype that cost less than 2000 USD and embraced the photogrammetry technique for surveying forests in Indonesia to obtain spatial information about the land use, illegal deforestation, and large animals. Based in flights up to 200 m above ground level, they discriminated features and generated land use occupation maps, like palm plantation, maze fields, human settlement, preserved and logged forests, trails, and also observed orangutans. Jiménez-López and Mulero-Pázmány (2019) conducted a literature review on the use of UAVs for conservation in protected areas and alerted that the foster effectiveness of UAVs remains fundamentally unexplored. The authors argued that applying UAV photogrammetry for quantifying ecosystem services is especially efficient when there is a lack of useful remote sensing data, with little spatial and temporal resolution. And highlighted that UAVs have the potential to assess the implementation and results of conservation actions, site design, and zoning, and to assist the reintroduction plan of endangered species.

In coastal ecosystem surveying, the approach plays a vital role in assessing post-storm impacts, perform a land cover classification, extract geomorphic feature, measure topography and beach erosion, coastal line delineation, and monitor vegetation recovering (Gonçalves and Henriques, 2015; Papakonstantinou et al., 2016; Turner et al., 2016; Sturdivant et al., 2017).

The main application discussed in this dissertation, which is the modeling and analysis of solar irradiation based in UAV SfM-MVS photogrammetry maps, is discussed in 3.3. Solar Irradiation Modeling section, along with other remote sensing tools for collecting spatial data.

3.3. Solar Irradiation Modeling

3.3.1. Geographic Information Systems

GIS is a set of tools and frameworks for managing, visualizing, storing, consulting, analyzing, and editing data, maps, and spatial information in general. There are two main data types: vector and raster. The raster data is represented by one or more layers of a grid, which stores information inside of their bands, for example, color value, altitude, slope, incident solar irradiation, etc. It can be continuous or discrete. However, the vector data is represented by geometric graphics, like points, lines, and polygons. In practice, both data are used together for computing GIS operations (Sanchéz-Lozano et al., 2013; Longley et al., 2015).

A Digital Elevation Model is defined as a Digital Surface Model (DSM) or as a Digital Terrain Model (DTM). The pixels in a DTM raster refer to the ground elevation, thereby there is no data about trees, buildings, cars, man-made structures, or other objects above the surface. In contrast, DSM contains information about both those elements above the ground and the ground itself.

Particularly for GIS environmental analyses where natural processes and phenomena are modeled, DSMs are important because they mold the physical barriers that drive the propagation of fluids (air and water) and electromagnetic waves (noise, heat, microwaves, solar radiation, etc). However, DTMs are adopted on studies focusing on the ground surface and morphology, such as topographic measurements and earthworks.

To generate a DTM in UAV SfM-MVS Photogrammetry, it is performed a point cloud classification to identify ground surfaces, which correspond to terrain data, DTM. In this case, the main limitations and challenges are in classifying the objects above surface and filling (by interpolation) gaps caused by removal of surface objects. Figure 13 illustrates the difference between a DSM and DTM and demonstrated that point cloud automatic classification needs improvement.

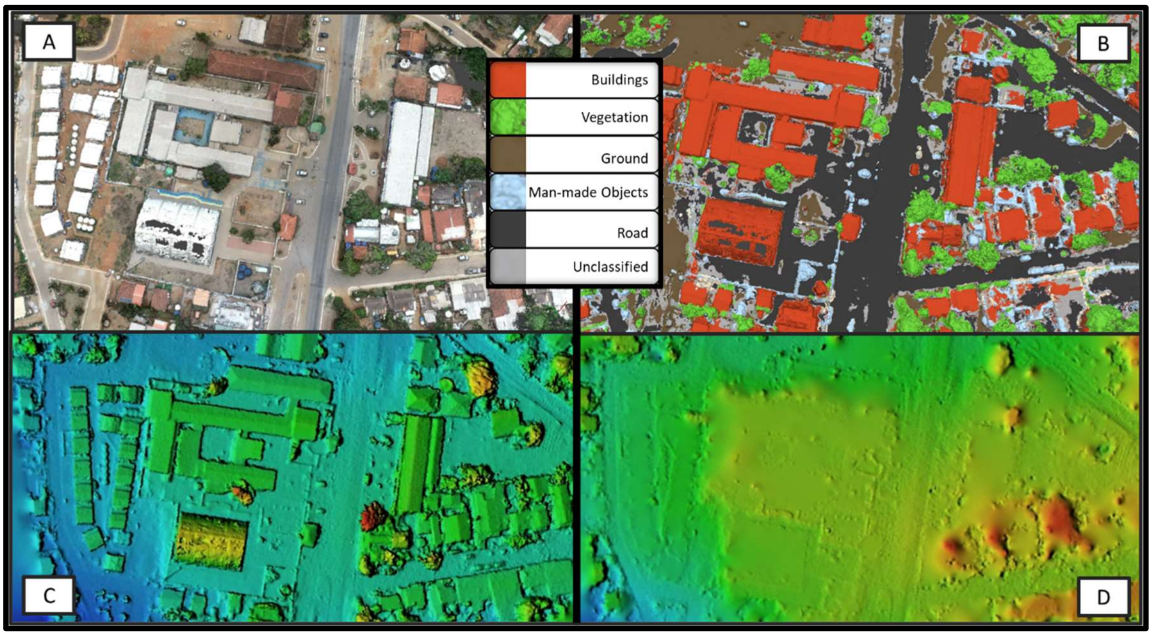

Figure 13. Sample of UAV SfM-MVS photogrammetric products in FNI: A) Point cloud. B) Point cloud automatically classified. C) DSM. D) DTM. The difference between a DTM and a DSM is visualized in C-D. Buildings, trees, and objects above the surface are represented in DSM, but not in DTM, which only represents the ground surface. It is important to stress that the automatic point cloud automatic classification presented here needs to be manually refined to achieve a final-product DTM, because some structures above surfaces were considered as a ground point (red pixels in D).

The comparison between LiDAR and UAV SfM-MVS photogrammetric surveys to produce DEM data is well discussed in the literature. It is important to highlight that in the context of PV potential analysis both methods are appropriate to model the complex morphology of an urban area, although they have different working principles.

Szabó et al. (2016) indicated that LiDAR surveys have a higher relative cost per building modeled, require higher expertise to collect and process data, cover wider areas and work better with topographic gaps because of higher flight altitude. However, the authors highlighted that it is unlikely that a small town or a company would hire a LiDAR survey to evaluate the PV potential. Tenedório et al. (2016) highlighted that the UAV photogrammetry can be used for areas wider than 1 km², but it will also require expertise and computational effort relatively similar to LiDAR surveys. The authors suggested that UAV is more appropriate for small regions due to periodicity, spontaneity, simplicity, and low cost.

Regardless of the survey technique, ideally, the DSM spatial resolution in urban solar irradiation modeling needs to represent all parts of rooftop structures and the features that shade rooftops and ground, where PV systems are typically installed. Moudrý et al. (2019) and Schuffert et al. (2015) argued that perform a

PV potential analysis in sub metric resolution DSMs are unnecessary due to the high annual variability caused by variations in atmospheric conditions and weather, which will have more significance than the variability caused by better spatial resolution. Simply put, the authors claimed that there is no need to use DSMs with a higher spatial resolution than 1 m/pixel, because the variations caused by meteorological and weather conditions are more significant and unpredictable. In contrast, Zink et al. (2015) and Besser et al. (2019) pointed out that 1-meter spatial resolution DSM cannot precisely identify PV available rooftop area because of miss-representation of chimes, water tanks, roof structures, elevator machine room, etc.

However, thinking of computational effort and useful outputs, Zink et al. (2015) suggested a 25-cm spatial resolution for an optimum equilibrium in the classification of usable rooftop areas. The authors claimed that a higher spatial resolution in DSM does not necessarily reduce errors in solar modeling outputs. They evaluated the aspect and slope algorithm outputs in GRASS GIS on less than 10-cm spatial resolution DSM and alerted that higher resolutions aggregate false estimation in irradiation modeling because of the high variability caused by differences in every single tile. It is important to note that the authors did not mention a fundamental smoothing step in photogrammetry SfM-MVS workflow before DEM generation, which is the mesh generation, that could potentially avoid high variability in DSM. Furthermore, the 25-cm spatial resolution recommended by the authors will face a long processing time when the area of interest is extensive (more than 1000 ha).

From the perspective of urban surveys and irradiation models for smart cities, Nelson and Grubesic (2020) discuss previous research and present differences and similarities between surveys with LiDAR sensors and those with photogrammetry with drone. In financial terms, one of the difficulties of LiDAR surveys is the high associated cost. The authors stressed that a manned plane or helicopter flight (one fuel tank operation) to cover a medium sized area can cost between US$ 20,000 – US$ 50,000, depending on the required operational logistics. In terms of spatial resolution, in general, UAV photogrammetry produces a denser point cloud than LiDAR surveys, managing to more accurately model small objects (like water tanks, air conditioners, etc) and the structures that shade or prevent the installation of photovoltaic systems on roofs. Thus, the authors demonstrated in their case study that the UAV photogrammetry DSM was able to estimate 36% more aggregate irradiation than the LiDAR DSM.

3.3.2. Overview of Solar Irradiation Modeling

To commence this section, it is convenient to distinguish the terms “irradiance” and “irradiation”. Solar irradiance regards to the instantaneous solar energy flux per unit area, typically expressed in W/m^2. However, solar irradiation represents the solar irradiance integration over the time, typically expressed in Wh/m^2, on an annual or daily interval. In other words, irradiation modeling aims to estimate the Global Horizontal Irradiation (GHI) (Hofierka and Kaňuk, 2009).

Understanding the solar irradiation phenomena is essential because life on Earth depends upon insolation, it influences energy flows, water balance, natural regimes, soil moisture, snow melting, evapotranspiration, and photosynthesis (Fu and Rich, 1999).

In the context of photovoltaic potential and smart-solar cities, a GHI model works toward a rational, efficient, and feasible planning and design of photovoltaic power systems.

Following the concepts presented by Perez et al. (1987), Fu and Rich (1999) and Šúri and Hofierka (2004), the GHI is composed of three independent components: direct, diffuse, and reflected. The solar irradiation that reaches a surface directly, without being reflected or scattered by atmosphere attenuation, is known as direct irradiation. It travels unimpeded in a line that starts at the Sun and finishes at the targeted surface (Adeleke, 2018). In that way, the irradiation scattered by the atmosphere attenuation is named diffuse irradiation, and the irradiation reflected by ground and superficial objects is called reflected irradiation. The three components combined are called GHI.

Reflected irradiation contributes little to GHI, and is therefore neglected in some modeling tools, such as in ArcGIS Solar Radiation. Moreover, the direct irradiation is the one that contributes the most to global irradiation and the diffuse irradiation presents the highest variability due to atmospheric dynamics, therefore, it is the main source of errors (Šúri and Hofierka, 2004).

The GIS-based solar irradiation modeling to estimate PV potential has been applied in different scales: a small area, a village, a town, a region, a nation, or a continent. For example, Nero et al. (2020) discussed the application and produced an irradiation model of some buildings of the Federal University of Minas Gerais, based on DEMs produced by UAV photogrammetry surveys. Mavromatidis et al. (2015) estimated the PV potential of a small village in Switzerland, Zernez, with 308 buildings and 1153 habitants, and presented a framework for the optimal integration of PV that considers the electricity demand profiles and PV potential. The authors considered a mixed 1-meter resolution DEM, a combination of topography and buildings height. Van Hoesen and Letendre (2010) used a 30 m resolution DEM to evaluate the PV potential for a rural community in Poultney, Vermont, USA. It worth noting that the papers cited did not consider the attenuation of irradiation caused by shading trees. The first because it was used a manipulated DEM that considered only terrain and buldings, and the second one, used a DEM with low spatial resolution, insufficient to distinguish trees, buildings, and terrain tiles.

On a big city, Wong et al. (2016) used a 50 cm spatial resolution LiDAR DEM (4 pt/m²) to estimate PV potential in buildings from Hong Kong and identify optimal PV rooftops. In a similar approach, based on 1-meter spatial resolution LiDAR DEMs of 128 USA big cities and shapefile polygons of buildings, Margolis et al. (2017) estimated the rooftop solar technical potential for approximately 122 million people. The paper demonstrated that freely available and high-resolution spatial data are essential for developing energy plans and targets of a sustainable future. Furthermore, Yushchenko et al. (2017) performed a regional scale GIS MCDM analysis to estimate geographical and technical potentials for the deployment of grid-connected and off-grid PV systems in rural areas in West Africa. The parameters considered in the MCDM were solar irradiation, distance to the grid, distance to roads, population density, protected areas, and distance from settlements.

Janke (2010) and Sánchez-Lozano et al. (2013) applied similar MCDM analysis to determine solar farm locations, in Colorado State, USA, and Cartagena, Spain, respectively. Also, on a regional scale, Bergamasco and Asinari (2011) used the freely available European Solar Irradiance Atlas (ESRA) and cadastral information to analyze the PV potential for municipalities from Piedmont Region, Italy. On a national scale, Rediske et al. (2020) used GIS MCDM and AHP methodology to identify the best locations in Brazil to install large PV plants and found out that more than 1000 km² are suitable for it. Finally, Vardimon (2011) assessed PV potential in building scale for Israel and found out that if it were deployed PV system with 10% efficiency in buildings with a rooftop area larger than 800 m², they could meet 7% of national electricity consumption.

In this review is important to mention the online platforms Project Sunroof (PS) by Google and the Global Solar Atlas (GSA) on behalf of World Bank Group, both are GIS models and are freely available for public administrators as well as final consumers of PV systems. The first one is based on a machine learning approach that constructs a 3D model by processing high spatial resolution satellite images available only in some cities in the USA and estimates PV potential based on shading and weather data from the National Renewable Energy Laboratory (NREL) (PS, 2020). As an example of using the data, Sunter et al. (2019) integrated PS data and the USA Census Bureau to analyze PV deployment by race and ethnicity in the USA. The second one, the GSA, provides global solar resource and PV power potential and also has a complex methodology to calibrate and estimate them (GSA, 2020). Dupont et al. (2020) used the GSA data, with a spatial resolution of 1 km/pixel, to analyze global PV potential and return of investments. Figure 14 presents the Global Horizon Irradiation map from GSA (GSA, 2020).

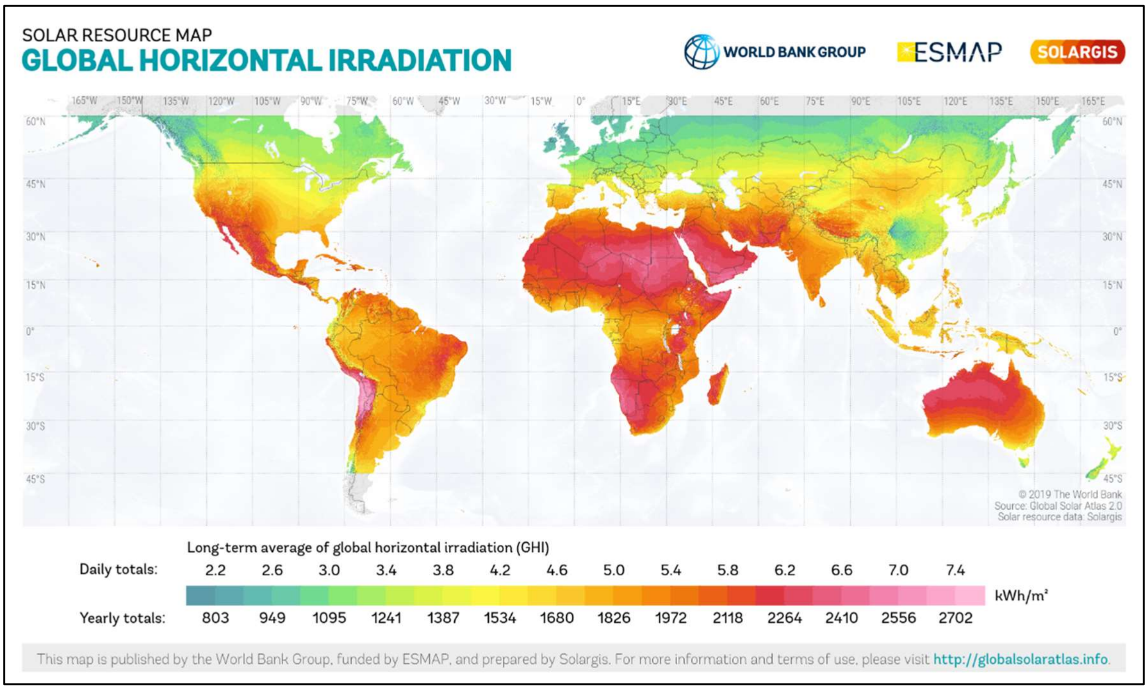

Figure 14. Global Horizontal Irradiation map from GSA. Source: GSA (2020).

Compared to the PS, the GSA output data have a worse spatial resolution, being insufficient to model buildings and support decision making in an urban complex morphology. In contrast, GSA covers all land areas between 60°N to 45°S, while PS consider less than hundred USA cities. The ideal data would have the high spatial resolution provided by PS and the extensive land cover from GSA.

In a different approach than online platforms, there are irradiation tools and algorithms available in commercial GIS software, for example, ArcGIS Solar Radiation (Fu and Rich, 1999; Kodysh et al., 2013) (used in this dissertation), and open-source GIS, for example, r.sun model integrated into GRASS GIS (Šúri and Hofierka, 2004; Nguyen and Pearce, 2012), SRAD and Solei-32 (Ruiz-Arias et al., 2009). Šúri and Hofierka (2004) informed that SolarFlux was the first GIS-based irradiation model, described by Dubayah and Rich (1995).

To model solar irradiation, ArcGIS Solar tool applies a geometrical approach that divides the sky into sectors defined by zenith and azimuth divisions, and the atmospheric attenuation is based on atmospheric transmissivity and proportion of diffusion (Fu and Rich, 1999).

The SRAD considers surface geometry, albedo, topographic shading, vegetation classification, among others. SRAD atmospheric attenuation is based on monthly averaged atmospheric transmission or sunshine fraction (Wilson and Gallant, 2000). The irradiation tools r.sun and Solei-32 use the turbidity coefficient of Linke to calculate atmospheric attenuation, which varies with latitude, time, and elevation. In that way, they are more appropriate for regional and continental modeling (Ruiz-Arias et al., 2009).

For more information about other GIS-based irradiation models, see Freitas et al. (2015), Martín et al. (2015), and Choi et al. (2019) reviews. The ArcGIS Solar Radiation toolset, the tool adopted in the present research, will be discussed in detail in the following 3.3.3. ArcGIS Solar Radiation toolset section.

In the context of urban GIS high spatial resolution solar maps, Erdélyi et al. (2014) indicated that the ray-tracing technique or similar approaches aim to determine if a surface is shaded by an obstacle, in other words, if the sunbeam that started at the Sun will be intercepted or not by physical obstacles before reaching a given surface. They stress that the step of raytracing requires high computational capacity. In that background, the model computation needs an optimum equilibrium between the DSM spatial resolution, solar modeling discrete time resolution, and computer processing capacity to achieve efficient outputs. The authors also claimed that most existing models do not consider shadows cast by buildings, trees, and obstacles. So, it is important to understand the limitations and accuracy of solar models before using it as a decision tool for PV power systems.

In this regard, Castellanos et al. (2017) discussed scalability and compared accuracies of irradiation maps produced by different methods, with varying spatial resolutions. Their results showed an average absolute percent difference of 110% between the methods. Because of that, the authors argued that policymakers are in a difficult position because they depend upon potentially low accuracy data or have to invest in expensive data collection methods of high spatial resolution, such as LiDAR surveys. It is important to note that the authors did not consider UAV photogrammetry as an alternative methodology, which can potentially reduce the costs of the survey.

Adeleke (2018) pointed out three main factors to compute solar irradiation modeling in a GIS environment. The first one is related to the constant extra-terrestrial irradiance, mainly based on Sun-Earth distances and angles and Earth’s rotation and translation. The second referred to the atmospheric influences caused by clouds and aerosols. The natural variability and dynamism in atmospheric conditions represent the most common source of error in GIS irradiation models, which results in some level of inaccuracy. The third factor depended on the terrain and surface characteristics modeled by the DSM, which must have enough spatial resolution to compute the slope, orientation, and ray-tracing operation that considers adjacent features and objects.

Krüger and Kolbe (2012) suggested three levels of decision-making when dealing with the Energy Atlas of Berlin, which is a solar irradiation modeling tool: i) Political and entrepreneurial level, ii) Design and planning level, and iii) Engineering level. The first level, for a regional and city scale, has the competence to establish strategic goals and legal regulations. The second, for a neighborhood and urban district scale, addresses solutions in spatial planning and conceptual design of PV systems. The third level, on a building scale, aims to build strategies for energy-efficient components, energy sources and production, and distribution networks. The authors did not enter in more details about the three levels, unfortunately. However, the authors noted that a wider scale requires more spatial aggregation and generalization, and in consequence, less spatial resolution and level of detail. In contrast to that, at a building scale, there are less generalization and more detail. From the perspective of this research, the solar irradiation model will be applied within a design and planning view for an urban district scale, the second level established by the authors.

Even though irradiation maps are widely applied to solar cadaster and evaluate PV potentials, it is also used within other environmental analyses. Mezei et al. (2012) analyzed the relationship between the number of spruce bark beetles caught in pheromone traps and the solar irradiation potential and found out a significant statistically positive relationship between the two variables. In a similar subject, De Groot and Kogoj (2015) researched the abundance of oligophagous insects in the forest ecosystem considering solar irradiation and other natural phenomena. The authors demonstrated a positive relationship between solar irradiation and larval (*Cheilosia fasciata*) abundance in its host plant (*Allium ursinum*). Pielech et al. (2015) indicated that solar irradiation is a landscape factor that influences the plant species composition and distribution in a spring riparian forest, but not in streamside forests, which have distance from river and stream power as driving forces. However, Salim (2012) presented a GIS analysis that involved solar irradiation, aquifer depth, aquifer salinity, among other factors, to support the decision-making process of selecting sites to install groundwater pump stations integrated with desalination by solar energy. Papers that present the relationship between solar irradiation resource and water desalination, agriculture, and other important subjects are presented in 3.1.4. Solar cities and islands section.

3.3.3. ArcGIS Solar Radiation toolset

The GIS tool adopted in this dissertation is the Solar Radiation toolset within ESRI ArcGIS Pro 2.4 software. This section describes the key calculations and steps behind the tool, which can be consulted on ESRI (2020) website, the theses Falklev (2017) and Adeleke (2018), and the paper originally presented by Fu and Rich (1999), when it was named Solar Analyst.

The tool has the ability to calculate the global horizontal irradiance on given points or geographic areas, and to integrate (within specific time-step configuration) to compute GHI (irradiation) over a period of time (ESRI, 2020). In this case, the global irradiance comprises direct and diffuse irradiance, but neglects reflected irradiance due to the irrelevant amounts (Fu and Rich, 1999). The four steps for estimation of global irradiance are: i) Calculate an upward-looking hemispherical viewshed based on topography and horizon angle tracing, ii) overlay of produced viewshed with sunmap layers to compute direct irradiance, iii) overlay of the produced viewshed with diffuse sky map to compute diffuse irradiance, iv) reiterating the process for every cell of interest to produce the insolation map (Adeleke, 2018; ESRI 2020).

The first step, which is the calculation of an upward-looking hemispherical viewshed considering the upward point of view, outputs a raster for every DSM grid cell that represents the portion of the sky that is visible or obstructed. This is similar to taking a fisheye photograph located on the center of each cell and pointed to the sky, which will show the visible sky and obstructed sky caused by topography and surface elements, as illustrated by gray (obstructed) and blue (visible) color in Figure 17.

Fu and Rich (1999) elaborated a sequence of figures that illustrate the step to calculate the viewshed for one DEM cell, which is represented and explained in Figures 15 a-e. The viewshed calculation role is to determine if a higher elevation DEM cell will shade lower elevation cells, like in a ray-tracing method. However, when dealing with smooth topography, the authors recommended tracing 16 horizontal angle directions, but in a complex environment, more directions should be considered, 32 or 64, always a multiple of 8.

Furthermore, another key parameter in ArcGIS Solar Radiation toolset, the viewshed resolution, or the sky size, must be sufficiently large to represent all sky directions, but small enough to allow efficient computation. The authors argued that a sky size of 200 x 200 cells is sufficient for most purposes, but if it is needed more accuracy and time calculation is not an issue, the sky size can be more detailed, 512 x 512. It is important to note that processing time quadruples when sky resolution goes from 200 x 200 to 400 x 400.

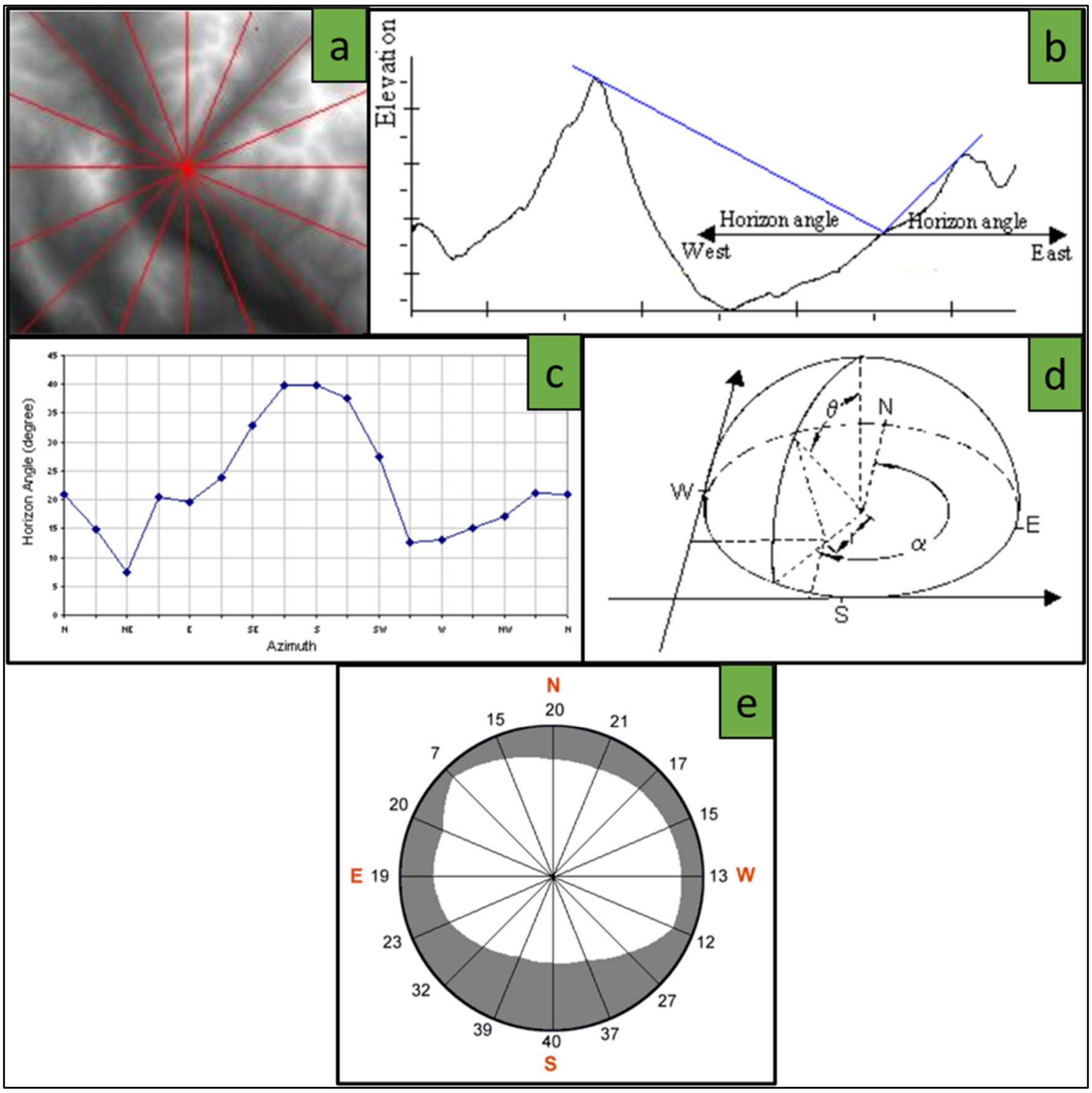

Figure 15. Calculation of the viewshed for one cell of a DEM. a) Horizon angles are traced along with a specified set of directions. b) Horizon angles are calculated for each direction. c) Horizon angles are interpolated in all directions. d) Horizon angles are converted to a hemispherical coordinate system. e) The resulting viewshed for a location represents which sky directions are visible and which are obscured. Numbers represent the calculated horizon angles. Source: Fu and Rich, 1999.

Once a viewshed is calculated for every DEM cell (Figure 15.e and Figure 16.a), the next step is to compute the sunmap, a raster grid that represents the track of the sun, i.e., the sun position varying through time intervals (hours, days or years) (Fu and Rich, 1999). The purpose of the sunmap is to compute direct solar irradiance that reaches each DEM cell. The sunmap is based on the same hemispherical projection of the viewshed, so sunmap and viewshed can be overlayed

The zenith and azimuth angles of the sun, which represent the sun's position to each DEM cell, are calculated based on astronomical equations that consider latitude and time parameters configured to define sunmap sectors. Each sunmap sector is defined by time configuration that symbolizes the position of the sun considering hour intervals through the day and monthly intervals throughout the year.

Figure 16.b demonstrates a sunmap of latitude 45 degrees North with a 1-hour interval calculated from December 22 to June 22, winter solstice to summer solstice. In the ArcGIS Solar Radiation toolset, data and interval parameters are set in the configuration window. Once a sunmap is calculated for each cell, the viewshed and sunmap are overlaid to calculate the direct solar irradiance, illustrated in Figure 16.b.

The next step is the calculation of skymaps, which represents a hemispherical view of the entire sky divided by sectors defined by the solar zenith and azimuth angles. Each sector from the bi-dimensional grid has a unique identifier value and has its centroid calculated to represent the direction of the sky sector to use in further calculations (Kodysh et al., 2013). In that way, the total diffusive irradiance that hits each DEM cell is the sum of all-sky map sectors irradiance value for that particular cell.

The diffusive irradiance is calculated for each skymap based on a uniform sky diffuse model or a standard overcast sky diffuse model. The first considers that diffuse irradiance income has the same value from all-sky, while the second includes a variation in diffuse irradiance income that is based on the zenith angle (Fu and Rich, 1999). Figure 16.c illustrates a skymap divided by 8 zenith divisions and 16 azimuths and the overlaying operation between skymap and viewshed to compute the diffuse irradiance income.

Within this framework, it is important to note that diffuse irradiance originates from the entire sky as a result of scattering caused by atmospheric elements (clouds and particles), and that the parameters diffuse proportion and transmittivity (in ArcGIS Solar Radiation toolset) adjust the atmospheric attenuations.

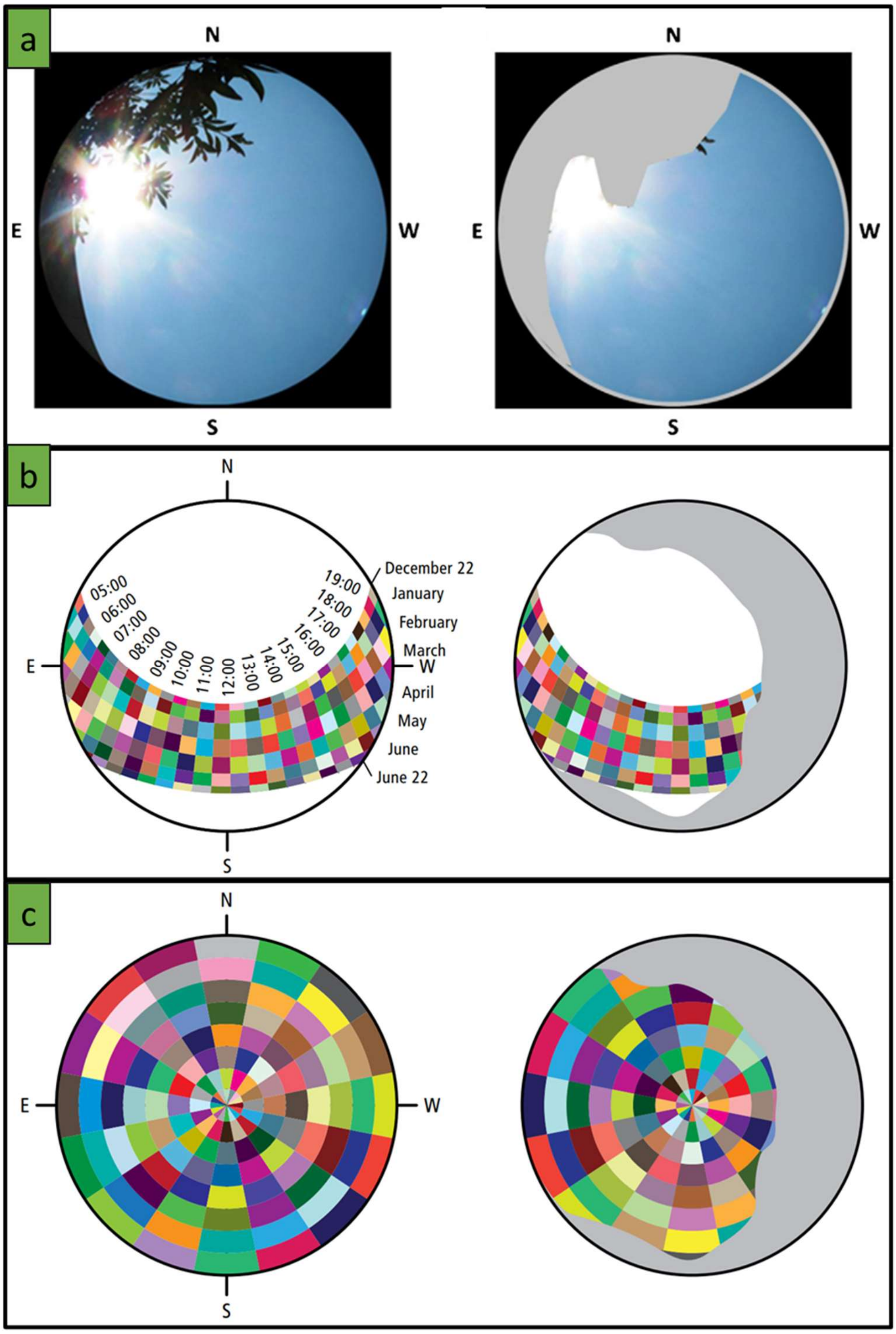

Figure 16. **a)** Left: Example of a fisheye photograph in an upward-looking manner. Right: Viewshed representation of the visible (blue) and obstructed (gray) sky. Source: Kodysh et al. (2013). **b)** Left: A sunmap representation from December 22 to June 22, within a 1-hour time interval, for a latitude of 45 degrees North. The sun sectors are represented by different colors of the grid. Right: Overlay of sunmap and viewshed to calculate the direct solar irradiance. Gray area represents the obstructed sun sectors. Source: Huang and Fu (2009). **c)** Left: A Skymap defined by sectors originated from 8 zenith divisions and 16 azimuth divisions. Right: The overlay between viewshed and skymap. Gray area means sky obstructed directions. Source: Huang and Fu (2009).

The next paragraphs are based in ESRI (2020) and explain the equations adopted in the calculation of direct and diffuse irradiance.

As stated, the Solar Radiation toolset considers that the global irradiance of a given DEM cell is the sum of the direct and diffuse irradiance income (Equation 3). The total direct irradiance is the sum of direct irradiance (**$Dir_{\theta,\alpha}$**) that comes from all sunmap sectors (Equation 4). Each sector is defined by the Zenith angle (**θ**) and Azimuth angle (**α**) and takes into consideration (Equation 5): the solar constant flux at 1367 W/m² (**Sconst**), the transmissivity of the atmosphere (**β**), the relative optical path length (**m(θ)**), the time duration represented by the sky sectors (**SunDur**θ,α), the obstructed gap fraction from the overlay of sunmap and viewshed (**SunGap**θ,α) and the incident angle between axis normal to the surface and sky sector centroid. In Equation 5, **m(θ)** is in the function of **θ** and the elevation.

Eq. 3 GlobalTot = DirTot + DifTot

Eq. 4 $DirTot = \Sigma Dir_{\theta,\alpha}$

Eq. 5 $Dir_{\theta,\alpha} = SConst * (\beta^{m(\theta)}) * SunDur_{\theta,\alpha} * SunGap_{\theta,\alpha} * \cos(AngIn_{\theta,\alpha})$

The tool allows users to set up the value for the parameter **β,** the discrete-time interval modeling configuration, and also to define if the surface aspect and orientation will originate from the DEM inputted or a specific value.

β values range from 0 (no transmission) to 1 (full transmission), being 0.5 typical.

Continuing ESRI (2020) explanation, to calculate the DifTot, which is the sum of diffuse irradiance incoming from every sky sector (**$Dif_{\theta,\alpha}$**), the Solar Radiation toolset adopts the following parameters to calculate $Dif_{\theta,\alpha}$ (Equation 6): global normal irradiance (**Rglb**), the proportion of diffuse irradiance compared to Rglb flux (**Pdif**), time interval configuration (**Dur**), the obstructed gap fraction from the overlay of skymap and viewshed (**$SkyGap_{\theta,\alpha}$**), the proportion of diffuse irradiance in a given sky sector relative to all sectors (**$Weight_{\theta,\alpha}$**) and the incident angle between the sky sector and the surface (**$AngIn_{\theta,\alpha}$**).

It is important to note that **Pdif** has a typical value of 0.2 for a truly clear sky and 0.7 for a very cloudy sky. Moreover, during the phase of calibration of the model, **Pdif** and **β** have an inverse relationship. Furthermore, **Weightθ,α** has a different method of calculation if it is adopted the uniform diffusive model or standard overcast sky model.

Eq. 6 $Dif_{\theta,\alpha} = Rglb * Pdif * Dur * SkyGap_{\theta,\alpha} * Weight_{\theta,\alpha} * \cos(AngIn_{\theta,\alpha})$

In the context of GIS, the type of GHI rasters generated by ArcGIS Radiation Toolset are floating-point and their measurement unit is watt-hours per square meter (Wh/m²).

The tool allows users to export some optional outputs raster, for example, annual, monthly or daily GHI (Wh/m²), direct irradiation raster (Wh/m²), diffuse irradiation raster (Wh/m²), direct duration raster (h), and graphic representation of viewshed, sunmap, and skymap.

A georeferenced DEM raster is the only mandatory file input needed for the irradiation modeling and it is recommended by ESRI (2020) that the data has a projected coordinate system in a unit of meters, otherwise, Z-factor corrections must be applied to the proper calculation.

The typical configuration parameters from the solar modeling geoprocessing tool are presented in Figure 17 and are classified into three categories:

(a) General modeling: latitude, sky size resolution, and timestep configuration.

(b) Topographic parameters, which control the viewshed raster generation: calculation directions and slope and aspect input type.

(c) Radiation parameters, which control the direct and diffuse irradiances calculus: zenith and azimuth divisions, diffuse model type, diffuse proportion, and transmittivity.

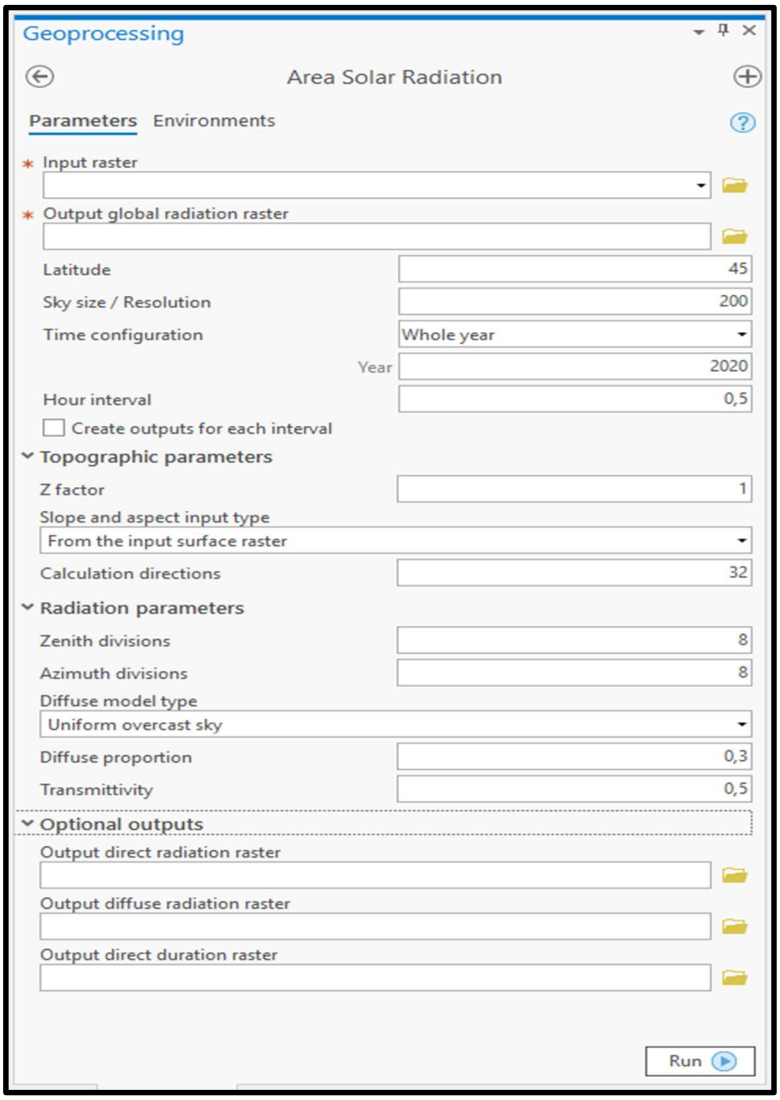

* Input raster
* Output global radiation raster
Latitude: 45
Sky size / Resolution: 200
Time configuration: Whole year
Year: 2020
Hour interval: 0,5
☐ Create outputs for each interval
Topographic parameters
Z factor: 1
Slope and aspect input type: From the input surface raster
Calculation directions: 32
Radiation parameters
Zenith divisions: 8
Azimuth divisions: 8
Diffuse model type: Uniform overcast sky
Diffuse proportion: 0,3
Transmittivity: 0,5
Optional outputs
Output direct radiation raster
Output diffuse radiation raster
Output direct duration raster

Figure 17. Configuration parameters window in ArcGIS Solar Radiation toolset.

Hofierka et al. (2002) alerted that adopting only one value for latitude for the entire DEM area limits the application to a local scale. Because of that, the authors considered the ArcGIS Solar Radiation modeling not flexible enough for calibration of atmospheric transmissivity and diffuse proportion for large areas. They recommended that if the DEM covers areas larger than 1 degree, the project should be divided into smaller areas for accurate results.

In the context of adjusting parameters in the ArcGIS toolset, to consider the modeling results as reliable and useful for making important decisions, it is necessary to calibrate the values for diffuse proportion and atmospheric transmissivity, and ultimately the output GHI. Although Fu and Rich (1999) claimed that validation data is not typically available, the model calibration can be done by calculating diffuse proportion and atmospheric transmissivity from: **(i)** analyzing cloud-cover data acquired by ground weather stations (Huang et al., 2008), **(ii)** by interpolation of pyranometer stations data and comparison with the output model value (Zhang et al., 2020), **(iii)** by comparing thermal satellite data with the output model value (Majumdar, 2018), **(iv)** or by comparing the nearest pyranometer station, prior calibrated models and the output model value (Marešová, 2014). However, when the aimed objective of the irradiation modeling is to quantify relative variations as a function of surface slope and aspect and shading effect, the radiation parameters do not require calibration and typical values can be adopted (Pelletier and Swetnam, 2017).

3.3.4. Potential assessment

The GIS DEM-based solar irradiation modeling aims to generate a raster file where cells values represent the estimated GHI, which is a theoretical potential of total available solar resources. This modeled data, also named resource or physical potential, is the base layer for afterward calculations and assessments of subsequent potentials. Following the concepts presented by Lopez et al. (2012), Fath et al. (2015), Lukač et al. (2016), Hong et al. (2016), Lee et al. (2018), and Bódis et al. (2019), the potentials that are in the scope of this review are physical, technical, economic and environmental. Figure 18 demonstrates the relationship between GIS solar potentials.

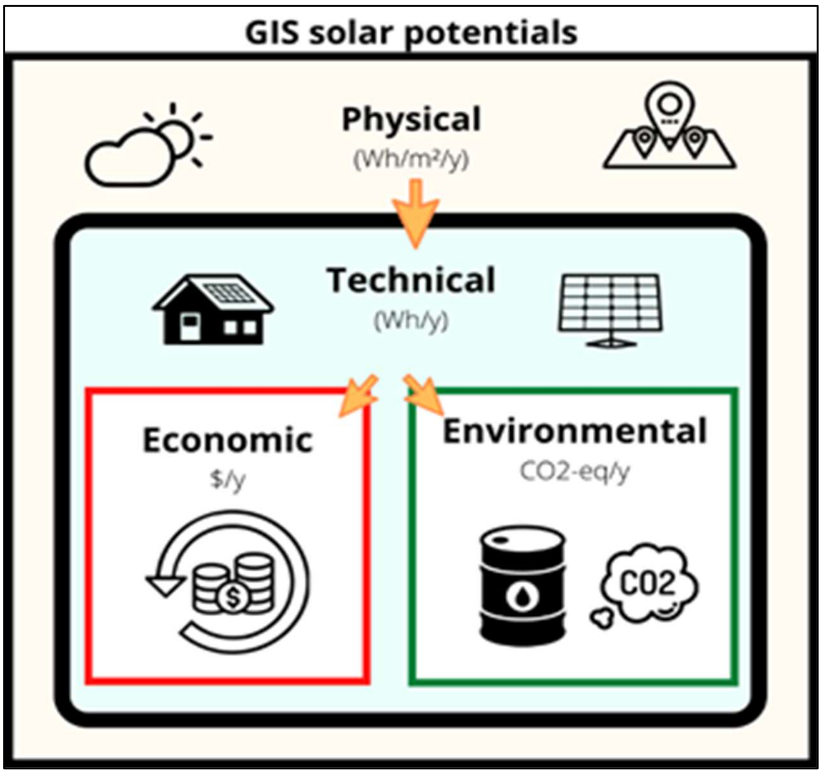

Figure 18. Demonstration of the relationship between solar potentials estimated using GIS tools and irradiation models. The economic and environmental potential derives from the technical potential, which in turn, derives from the physical (modeled) potential.

As detailed in the previous section, key factors in the calculation of physical potential are the surface orientation, aspect, sun and global position, shading technique to identify sunlight obstructions, atmospheric conditions, and model specifications and parameters.

The most aimed metric of a PV system is the technical PV Potential, i.e., the annual yield for electricity generation. Peronato (2019) estimated PV potential based on the physical potential, rooftop available area, panel efficiency (η), inverter efficiency, system performance ratio (PR), and ambient temperature. For the last three factors, Lopez et al. (2012) substituted them for an overall capacity factor, which is the ratio of actual electricity produced by a given power system over the maximum possible electricity output that it can generate. The approach of using a capacity factor is typically adopted when dealing with large scale renewable energy plants, thereby is out of the scope of this dissertation.

In the studies presented by Schallenberg-Rodríguez (2013), Eicker et al. (2013), and Fath et al. (2015), once area and physical potential were determined, the factors η and PR were adopted to predict the potential to produce PV electricity. More simply, Lee et al. (2018) considered only the η.

In that matter, solar cells made of different materials have different η, for example, organic thin-film cells have an efficiency of 11.0 ± 0.3%, Si (crystalline) 25.6 ± 0.5 and Si (multi-crystalline) 20.8 ± 0.6 (Green et al., 2015). However, Fath et al. (2015) adopted 15% for multi-crystalline modules. Moreover, Lukač et al. (2016) noted that η will decrease as time passes and irradiance varies (Figure 19), and Lee et al. (2018) assumed that the system degradation rate of the technical performance reduces 0.8% annually and highlighted authors that indicated that during the useful 25 years lifetime project, the PV technical performance degraded 20%. Furthermore, the PR depends on variations on material quality, irradiance, temperature, and internal losses from inverter operation.

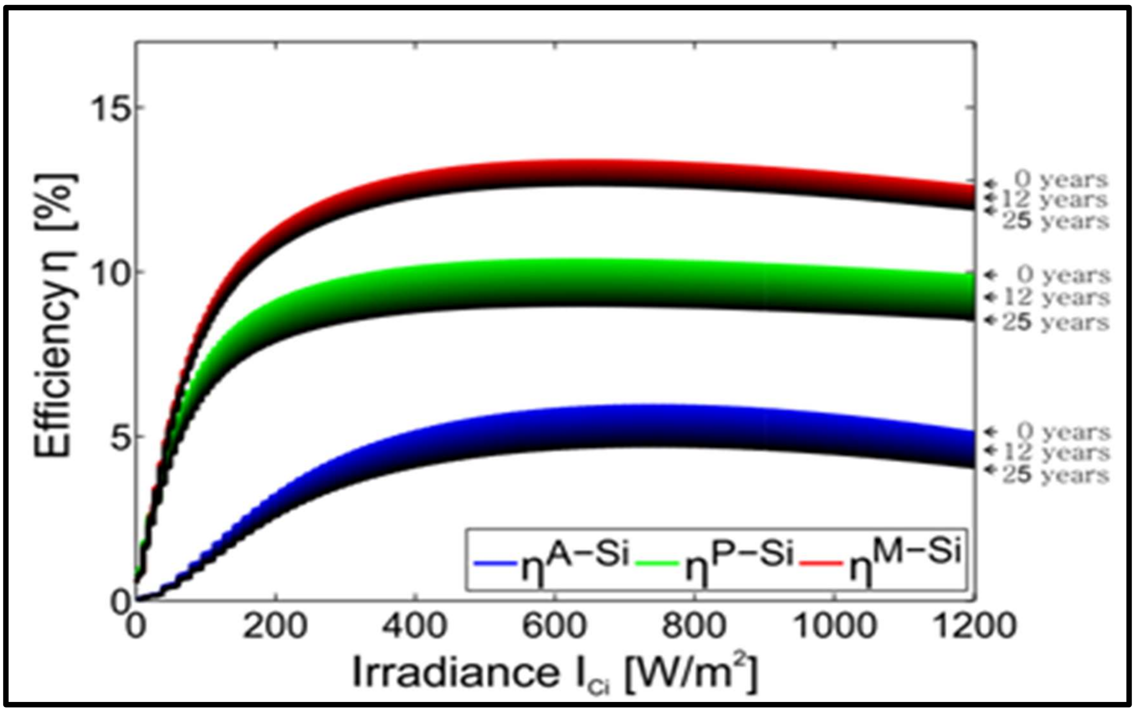

Figure 19. Lifetime nonlinear efficiency for three PV systems composed of different materials and the same microinverter. Source: Lukač et al. (2016).

The PR annual average adopted by Fath et al. (2015) was 90%. For purposes of comparison, studies showed that PR annual average range from 70% to 88% in real measurement (Shukla et al., 2016) and 73% to 76% in well-known PV simulation web-platforms, e.g., SolarGis, PVSOL, PVGIS and SISIFO (Dondariya et al., 2018).

The economic analysis of a PV system based on irradiation maps focuses on two relative financial indices: the payback period (PP) and the return of investment (ROI). This kind of analysis investigates whether the location of a PV system is profitable or not. PP refers to the time required for the PV system to be able to cover the costs of the system itself. The lower the PP, the better for the PV system owner. ROI indicates the profitability for PV systems, it stands for the ratio of cash inflows and outflows. A ratio greater than 1 indicates that the PV system is economically attractive and is profitable throughout its lifecycle (Lee et al., 2018). In general, the economic analyses depend upon the amount of energy produced, the selling price of a KWh in the feed-in tariff, the project lifetime, the interest rate, the ICI and O&M costs (Fath et al., 2015; Lukač et al., 2016; Lee et al., 2018).

As well as in technical PV potential, the economic mathematical functions used by modelers vary in levels of complexity and scale. For example, Miranda et al. (2015) evaluated the economic potential of PV systems on Brazilian rooftops considering low spatial resolution GHI maps and included specific data in their calculation, for example, residential income, electricity consumption, available rooftop area, load curve, ICI and O&M costs, and renewable energy financing policy by public banks.

On a local scale, based on a high-resolution LiDAR DEM and GHI map, Lukač et al. (2016) estimated the net present value (NPV) of PV systems in residential areas taking into consideration the shadowing effect, pyranometer irradiance measurements, local feed-in tariff and market statistics. The authors also estimated two scenarios based on the minimum and maximum average yearly feed-in tariff, where the most suitable roofs had positive NPV after 3 and 11 years, respectively (Figure 20). Nonetheless, Fath et al. (2015) pointed out that economic potential assessments are not common in potential studies and that the unexpected plant dropping prices, such as the 66% reduction occurred from 2006 to 2013, undermined the economic assessments made before that.

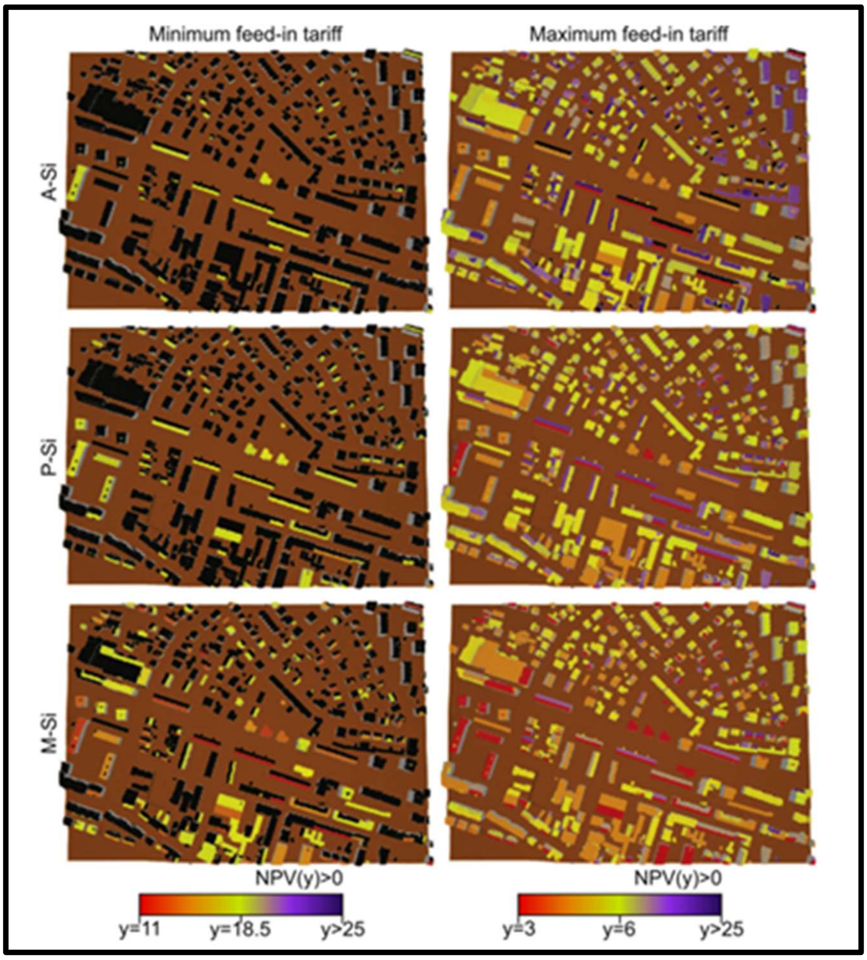

Figure 20. The number of years for the investment to be returned (i.e. NPV(y) > 0) for the two considered feed-in tariffs scenarios in Slovenia and three different PV systems. Source: Lukač et al. (2016).

The environmental potential assessment refers to the quantity of CO_2 that would have been emitted if fossil fuel had been used as a source of energy (Desthieux et al., 2018), simply called carbon savings or ecopotential. The carbon intensity conversion rate (CI) represents the amount of CO_2 emissions per kWh of electricity produced, which is in the function of the source of energy. For example, in a case studied in Madrid, Esclapés et al. (2014) assumed a CI of 600 g/KWh of CO_2, while in Western Europe, Lukač et al. (2016) considered 420 g/KWh of CO_2. Peronato (2019) went further in a more complete and complex assessment by introducing the life cycle analysis into the assessment. In their case, the author used 300 g/KWh of CO_2 for CI and included the carbon footprint of solar panels as 70 g/kWh of CO_2.

The environmental potential data is crucial to evaluate the environmental impacts in the context of sustainable and solar cities, particularly for the public administration that needs quantitative data to develop environmental policies that combat climate change (Camargo et al., 2015). Mavromatidis et al. (2015) pointed out that in the case of the absence of environmental policies, it is common to follow economic criteria in decision-making processes.

4. Methodology

The methodology approached in this research made use of a sequential workflow that combined (i) UAV photogrammetry, (ii) high spatial resolution irradiation modeling and PV Potential assessment, and (iii) proposition of scenarios of PV transition. In that way, this chapter has one topic dedicated to each technique. Figure 21 presents a flowchart of the methodology.

In brief, the orthophoto produced by the UAV photogrammetric survey were used to identify all buildings and open areas, which are the surfaces that can produce decentralized and centralized PV energy, respectively. Further, the DSM were employed to produce the high spatial resolution GHI model. In sequence, buildings and open areas vectors were used in zonal statistics tools to tabulate individual irradiation data. The output table was then used to assess the PV and Environmental Potentials for every building and open area and calculate total PV potentials.

After analyzing the Total PV Potential for decentralized and centralized sources in APA-FNI, it was possible to schematize 9 scenarios where combined PV production surpasses the annual electric consumption, meaning that a PV transition is technically feasible. Scenarios were constructed considering real world limitations, such as percentage of buildings that will adopt PV rooftop systems, percentage of roof area occupied by PV systems, and available (already cleared) open areas to install PV plants. The key result is presented on a table containing for each scenario numbers of (i) Decentralized Rooftops PV-Potential (GWh/yr), (ii) Centralized PV complementary power (GWh/yr), (iii) Centralized PV plants area required (m²).

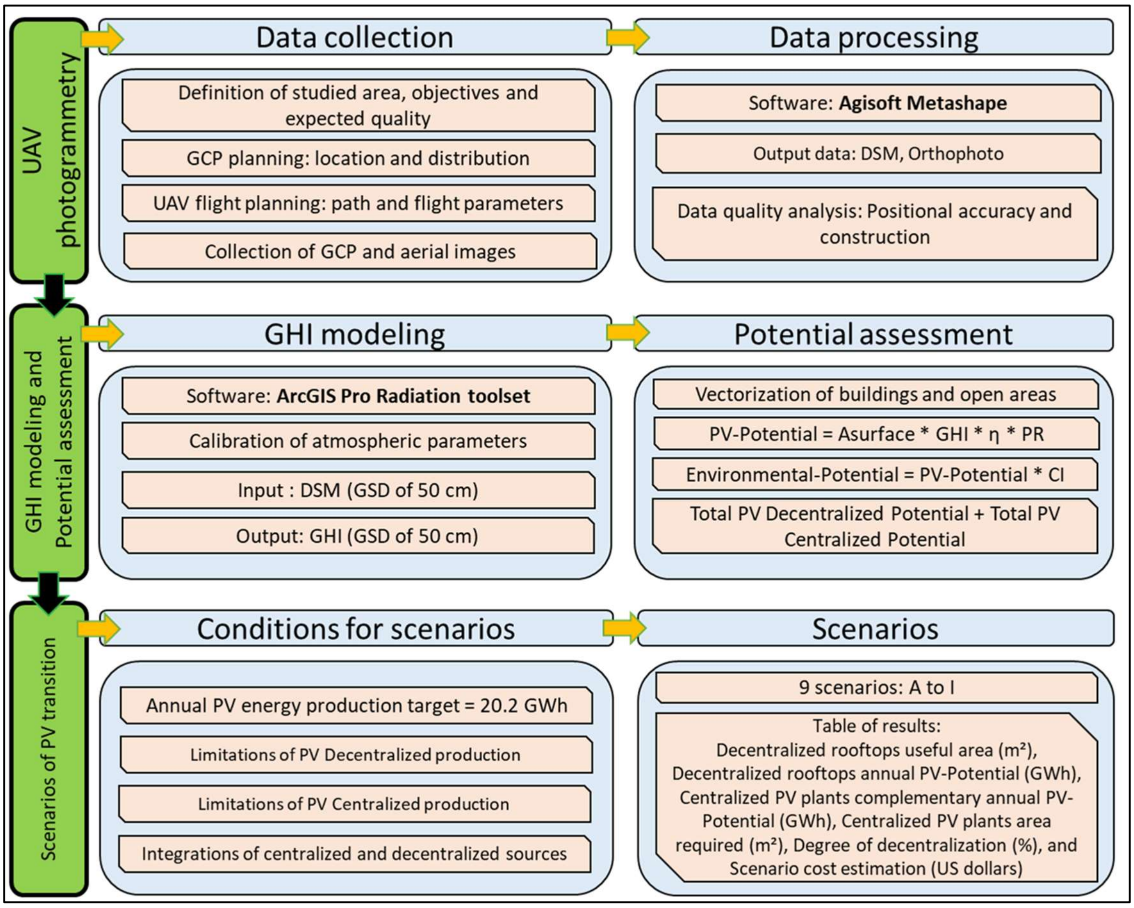

Figure 21. Flowchart of the methodology.

The information about FNI is available in the 2. Background – Fernando de Noronha Island section.

Worth noting that “*Morro do Pico*” and “*Morro do Espinhaço*” were not fully covered by the UAV because of their high altitude, which brought risk and uncertainty for the aerial missions.

4.1. Phase 1: Photogrammetric survey

This case study followed a typical photogrammetry SfM-MVS workflow mentioned in literature review, to ultimately produce an orthophoto and a digital surface model georeferenced, with very-high spatial resolution.

Once the scope of the project has been defined, the next steps were to plan and collect UAV imagery data and measure GCP coordinates, which were described in the following 4.1.1. Photogrammetric Data Collection section.

After that, the 4.1.2. Photogrammetric Data Processing section described the methodology adopted in Agisoft Metashape 1.6 software to produce the point cloud, mesh, DSM, and orthophoto, and the positional accuracy analysis.

The planning of the UAV photogrammetry survey included the definition of coverage area, composition of the field team, identification of takeoff areas and access and transportation routes, definition of UAV and GNSS receiver models and accessories needed, evaluation of the site and local topography, verification of current legislation, registration of research project in areas of environmental protection, requisition of flight notification, among other basic actions before going on a field campaign.

The field team was composed by three members of the Post-graduation Program in Analysis and Modeling of Environmental Systems at the Universidade Federal de Minas Gerais: Daniel Salim (the author, student), Guilherma Gandra (student), and Professor Marcelo Nero (Advisor Profesor). Worth mentioning that ICMBio helped the field team with accommodation and getting around hard access places with 4x4 vehicles to install RTK basis and take-off the UAV. Moreover, the Post-graduation Program also helped with basic logistics, such as GNSS equipment rental and flight tickets.

For the present research on FNI, the data collection phase of the photogrammetric survey took place between the morning of the 10th and midday of the 17th of December 2019. The plan was to be on the field until the 19th, but it was not possible due to the bad weather caused by the natural phenomenon called “Swell”, originated by strong winds coming from the ocean. The forecast forced the team to work faster and more efficiently.

Once data was collected, the phase of data processing was performed on a dedicated computer.

4.1.1. Photogrammetric data collection

The UAV photogrammetric methodology proposed in this research needed two basic input data: sufficiently overlapped aerial images and GCP precise coordinates. Both tasks were initially planned with the limited image and elevation data provided by Google Earth, which was complemented using SRTM DEM and Copernicus Sentinel-2 satellite image. Based on that, were identified landing and takeoff points, accessible trails, highest risk flight areas, potential locations for GCP distribution, and obstacles that could obstruct the GNSS receiver’s connection link. Moreover, the Geodetic Database from IBGE (2020, b) offered potential locations for RTK base installation, which were geodetic stations ratified by IBGE.

For the flying mission, the UAV DJI Phantom 4 Pro was used as a remote sensing platform to acquire aerial images. Together with the remote controller and the tablet, they constituted the unmanned aerial system. The flight routes and parameters were programmed on the Drone Deploy application.

For the GCP measurement, were used the GNSS receiver Zenith 10 and X-PAD Ultimate survey application. The deployment of GCPs was shrunk to a feasible area of interest due to bad weather forecast, time management, positional quality required, and access issues.

Figure 22 presents the calendar of field operations and basic numbers of the photogrammetric data collection phase.

Calendar of field operations

Day	Number of Photos	Number of GCPs
10/12/2019	2091	0
11/12/2019	1597	18
12/12/2019	1518	0
13/12/2019	533	69
14/12/2019	442	93
15/12/2019	0	61
16/12/2019	1014	0
17/12/2019	1186	0

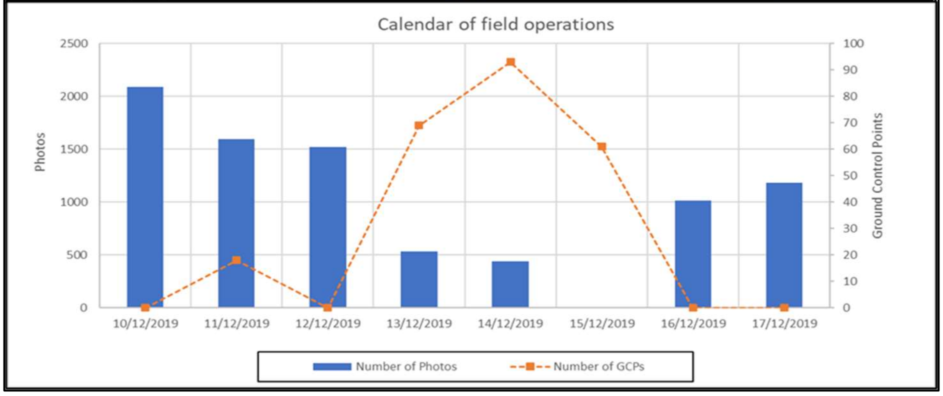

Figure 22. Calendar of field operations. On the 18th and 19th of December, 2019, bad weather precluded field operations.

4.2.2.1. Image acquisition

The DJI Phantom 4 Pro used in this research is a consumer-grade UAV that carries onboard: NAVGNSS, single-frequency GNSS receiver, IMU system and Vision System with multilateral sensors to avoid obstacles, DJI FC6310 camera, LiPo intelligent battery 5870mAh, 3-axis (pitch, roll, yaw) Gimbal, etc. The camera lens has an 8.8 mm focal length and a 13.2 mm width, which corresponds to a 13.2 x 8.8 mm image size of 5472 x 3648 pixels and a pixel size of 2.61 x 2.61 µm. It also includes a 1” CMOS sensor of 20M effective pixels. Including the battery and propellers, the aircraft weights 1388 g and can stay up to 30 min flying on a single new battery (DJI, 2020).

For image acquisition, the camera was configured to automatic settings to avoid over or underexposure, blur, and white balance variations on photographs.

Once the coverage area and UAV model were defined, the primary flight parameters for the photogrammetric flight mission were altitude and overlapping percentage. The other parameters were resultant from them, for example, the number of photos, flight speed, length, and time. In this manner, the altitude influenced directly the orthophoto spatial resolution and the overlapping percentage determined the quality of 3D and 2D reconstruction.

In that regard, it was determined a constant percentage of 75% for longitudinal overlap and 65% for side overlap, and a flight height varying from 120 (in APA-FNI area) to 200 meters (in PARNAMAR-FNI). In that configuration it is expected that terrain and objects above surface (trees and buildings) are modeled through the SfM-MVS stitching process, which is fundamental for shading calculations in GIS irradiation modeling.

A set of 13 batteries were used to cover the 2200 ha area in 8 days. To cover FNI, the flight missions were divided into 50 programmed, adjacent flight blocks of around 50 ha each. It was guaranteed that at least one flight line overlapped between adjacent flight blocks. In total, 64 gigabytes of data and 8383 aerial photos were acquired. The coordinates of the aerial photos are illustrated in Figure 23.

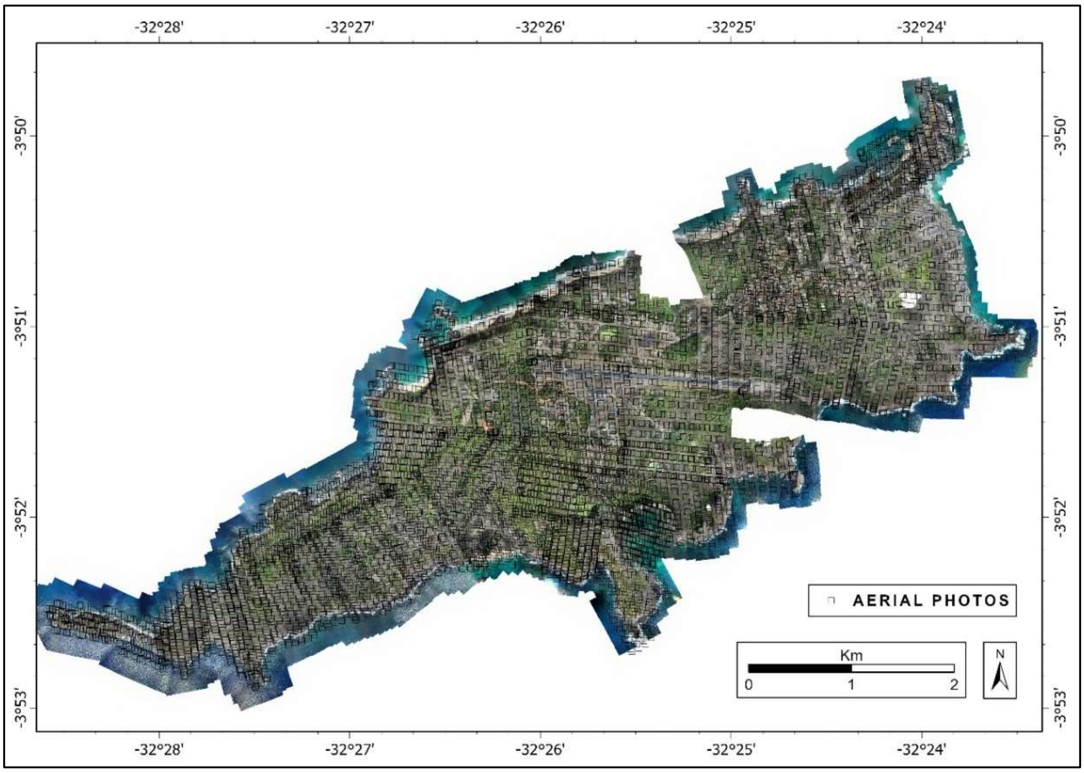

Figure 23. Coordinates of the aerial photos acquired in FNI.

4.2.2.2. Ground Control Points measurement

The GCP coordinates were measured using the RTK positional mode and a pair of dual-frequency L1/L2 Geomax Zenith 10 receivers, which have horizontal accuracy of 10 mm + 1 ppm and vertical of 20 mm + 1 ppm. They were configured within the Geomax X-PAD Ultimate application and were set to consider fixed points with horizontal and vertical accuracy below 5 cm. The project coordinate system was set to SIRGAS 2000 / UTM zone 25S (EPSG::31985).

The GCP considered in this research were all already built or painted structures, e. g., arrows, crosswalks, sidewalk corners, culverts, stones, etc. Out of 241 points collected, 63 were used on the point cloud georeferencing (GCP-Georefencing) and 22 as a checkpoint (GCP-Checkpoint) for positional assessment. They were selected based on their distribution and inter-distance (Villanueva and Blanco, 2019), size, sharpness, and distinctiveness to their surrounding environment (Carrivick et al., 2016), Figure 24 exemplifies a GCP measuring and marking task.

Figure 24. Up: GCP measured in a stripe painted on the floor (Professor Marcelo Nero). Down: Placing a marker on a photo.

Among the five installed IBGE geodesic basis on the main island, only the 91569 IBGE base station located on top of the *Forte Nossa Senhora dos Remédios* and the 91571 located at the *Mirante do Vor* were preserved (IBGE, 2020 b), while the others three had their landmarks removed or damaged.

Figure 25 presents the RTK scheme adopted in this study case. The bases were installed in three locations: in 91569 IBGE base, to cover the Eastside of the APA-FNI; in 91571 IBGE base, to cover the Westside; and in front of ICMBio head office, to cover the central area. The last one was transported from 91571 IBGE base. Figure 25 also reveals the GCP distribution and a straight line connecting the RTK base to the GCPs measured with the hover receptor.

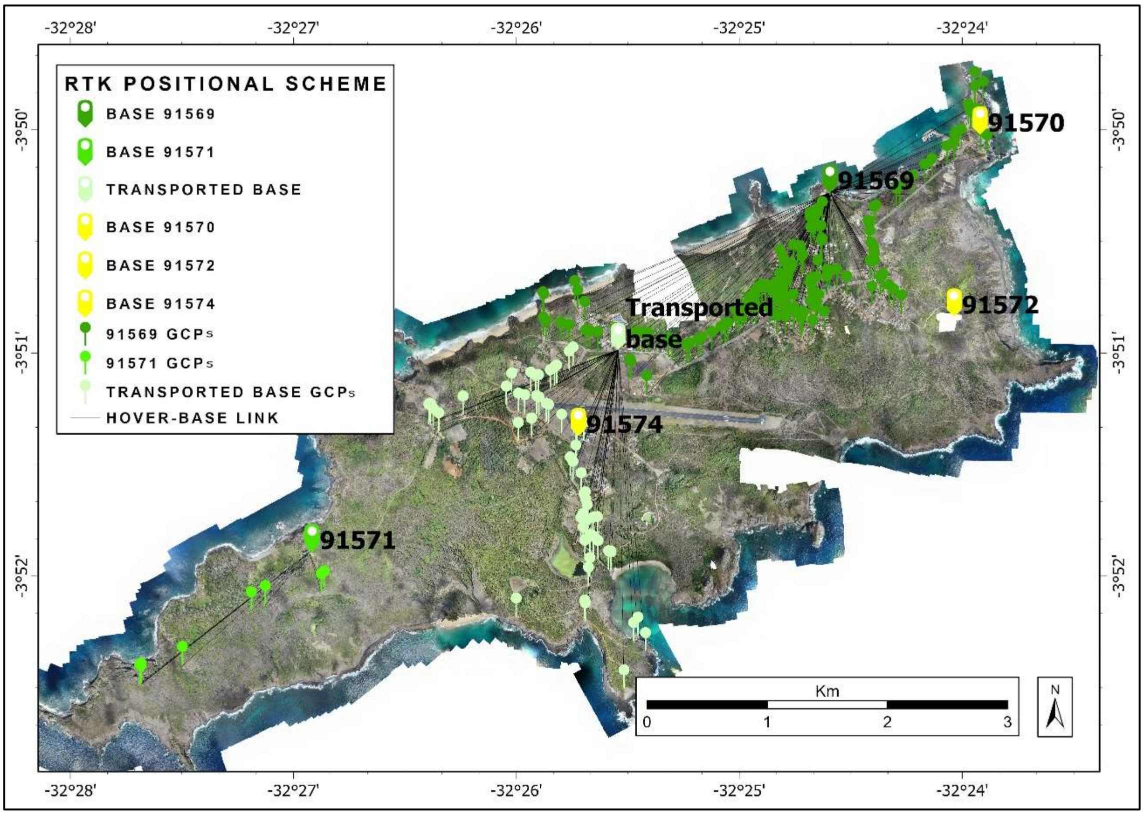

Figure 25. RTK positioning scheme of GCPs measurement. The GCP distribution was mostly concentrated on the urban areas, on the areas that do not have environmental restrictions for installing PV plants, or where high-quality positional accuracy was needed. In those areas, the GCP distribution followed the recommendations presented in the literature review.

Although Villanueva and Blanco (2019) and Manfreda et al. (2019) recommended and verified that distribution of points in the extremities and at homogeneous inter distances in photogrammetric surveys resulted in better positional accuracy, their recommendations were not completely followed on this survey because of three factors. Firstly, particularly for this research, there was no need for high positional accuracy in PARNAMAR-FNI because of environmental legislation preventing the installation of PV plants there. Secondly, due to its remoteness, these areas are hard to reach and walk. This would not be a problem if time were not an issue and 4x4 vehicles and boats were easily available. Thirdly, in some areas, there were no distinctive ground elements that could be used as GCPs. Nevertheless, in urban areas of APA-FNI the GCP network was homogeneously distributed and followed the mentioned literature.

Regarding the orthophoto positional quality, it was followed the Point-to-Raster comparison method proposed by Carrivick et al. (2016), using GCPs coordinates measured on fieldwork to analyze the positional accuracy of the orthophoto raster. The residual difference between ground truth GCP-Checkpoints and orthophoto coordinates were calculated to feed the RMSE statistic calculation (Equation 7). The positional analysis was limited to the area covered by the 91571 IBGE basis, the only undamaged inside APA-FNI, and encompassed 22 GCP-Checkpoints.

Eq. 7. RMSE =

$$\sqrt{\sum_{i}^{n} \frac{(\boldsymbol{E}\_Orthophoto_{i} - \boldsymbol{E}\_GCP\_Checkpoint_{i})^2 + (\boldsymbol{N}\_Orthophoto_{i} - \boldsymbol{N}\_GCP\_Checkpoint_{i})^2}{n}}$$

4.1.2. Photogrammetric data processing

The Agisoft Metashape 1.6 was adopted for the SfM-MVS photogrammetry process that aimed to produce an orthophoto and a DSM, used further to conduct the solar irradiation modeling. The computer used had the following configuration: Windows 64-bit, RAM 128 Gb, CPU Intel(R) Core (TM) i9-9900KF CPU @ 3.60GHz, and GPU GeForce RTX 2080.

The processing methodology was described in 3.2.2.1. Photogrammetric data processing in Agisoft Metashape 1.6 section and was based in Agisoft LCC (2019). Moreover, the parameters used in the photogrammetric process followed USGS (2017) recommendations.

The parameters adopted for the alignment were: high quality, reference selection, key point limit set to 60,000, and tie point limit set to 0 (no limit) (USGS, 2017). After filtering the sparse point cloud, where the unwanted points were removed, 9.9 Million points were selected out of 21 Million.

The next step generated the dense point cloud. The processing quality was set to high, so rooftop buildings could be well represented in the dense cloud. The densification of the sparse point cloud produced 2.8 Billion points.

In sequence, the mesh was constructed using a high-quality set, which produced 212 Million polygonal faces. The high-quality mesh reduces noise and variation in DSM pixels, which provides a smoother GHI model.

In sequence, the DSM was generated with a default spatial resolution, GSD of 10.6 cm. But, because of better efficiency in solar GHI modeling, the raster was resampled to a GSD of 50 cm.

Finally, the orthophoto was generated with a GSD of 5.3 cm. The elevation surface considered to ortho mosaicking was the DSM built using the mesh.

4.2. Phase 2: Solar irradiation modeling and PV Potential assessment

As stated, the ArcGIS Solar Radiation toolset was employed for the solar irradiation modeling. In that regard, the irradiation modeling and analysis occurred at a GSD of 50 cm. Thereby, buildings and open areas can be well represented in the modeling.

Although a better spatial resolution would represent the objects above rooftops with more details and thereby, produce a more accurate solar irradiation data, it was not applied because the meteorological annual variability is more significant than higher spatial resolutions variability, and it would increase computational processing time significantly (Nelson and Grubesic, 2020).

4.2.1. ArcGIS Solar Radiation calibration

The ArcGIS Solar Radiation toolset employed two meteorological calibration parameters: diffuse proportion and atmospheric transmittivity. In the present research, calibration followed the approach proposed by Majumdar (2018), which computed multiple models varying calibration parameters and selected the most suitable pair, with the lower RMSE. In this research, the DEM used in calibration was an SRTM resampled to the same spatial resolution that the observed data, 277 m/pixel. The observed data were provided by the World Bank Group’s GSA (2020).

The calibration was done in two steps, the first considered a variation of 0.1 in the parameters, and the second 0.05. The diffuse proportion parameter varied from 0.20 to 0.40 and the atmospheric transmittivity from 0.50 to 0.65.

The RMSE error was calculated based on Equation 8. The Raster Calculator tool was used to compute mean difference and the RMSE for every pair variation of diffuse proportion and atmospheric transmittivity.

Eq. 8. RMSE Error = $\sqrt{\sum_{i}^{n}\frac{(RASTER.MODELED\mathrm{i} - RASTER.OBSERVED\mathrm{i})^{2}}{n}}$

In this case, n is 2448, the number of cells in the raster file, which is defined by raster columns and rows. Table 1 details the calculation performed for the model calibration. Green background cells represent the most accurate modeling in each calibration phase. The pair with less RSME had a diffuse proportion of 0.25 and atmospheric transmittivity of 0.60. In that way, the parameters adopted in the best calibration scenario were the same used to generate the GHI models in higher spatial resolution.

Table 1. Calibration of ArcGIS Radiation toolset

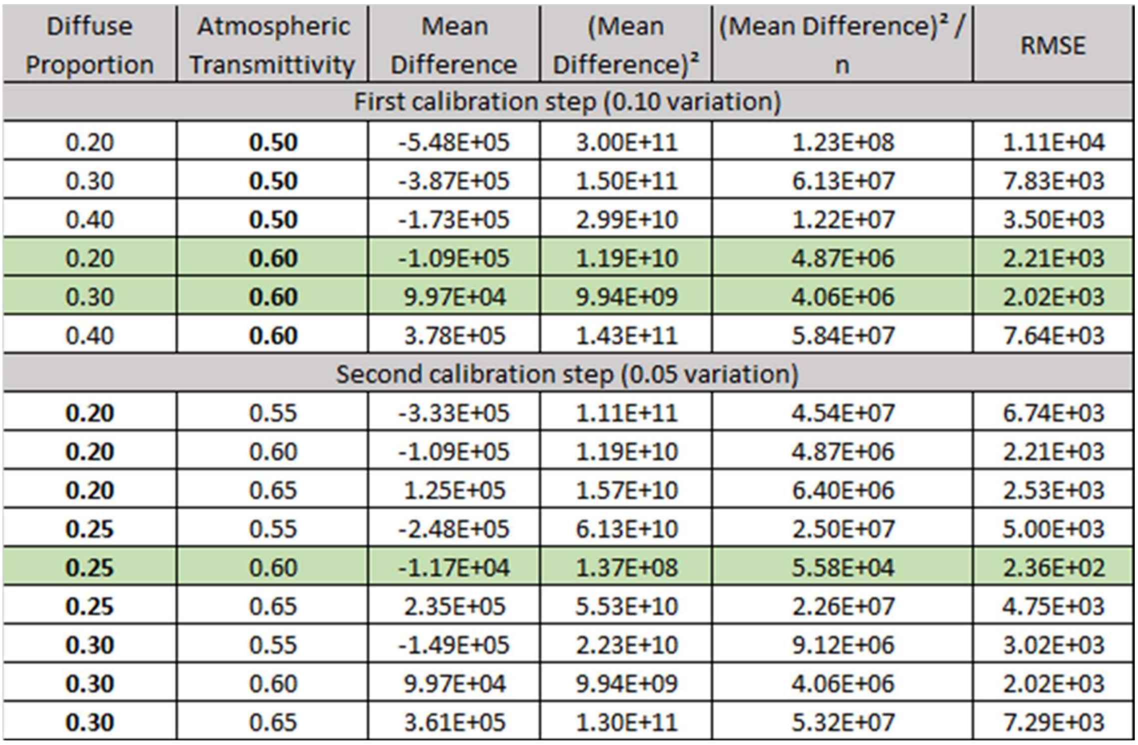

Diffuse Proportion	Atmospheric Transmittivity	Mean Difference	(Mean Difference)^2	(Mean Difference)^2 / n	RMSE
First calibration step (0.10 variation)					
0.20	**0.50**	-5.48E+05	3.00E+11	1.23E+08	1.11E+04
0.30	**0.50**	-3.87E+05	1.50E+11	6.13E+07	7.83E+03
0.40	**0.50**	-1.73E+05	2.99E+10	1.22E+07	3.50E+03
0.20	**0.60**	-1.09E+05	1.19E+10	4.87E+06	2.21E+03
0.30	**0.60**	9.97E+04	9.94E+09	4.06E+06	2.02E+03
0.40	**0.60**	3.78E+05	1.43E+11	5.84E+07	7.64E+03
Second calibration step (0.05 variation)					
0.20	0.55	-3.33E+05	1.11E+11	4.54E+07	6.74E+03
0.20	0.60	-1.09E+05	1.19E+10	4.87E+06	2.21E+03
0.20	0.65	1.25E+05	1.57E+10	6.40E+06	2.53E+03
0.25	0.55	-2.48E+05	6.13E+10	2.50E+07	5.00E+03
0.25	0.60	-1.17E+04	1.37E+08	5.58E+04	2.36E+02
0.25	0.65	2.35E+05	5.53E+10	2.26E+07	4.75E+03
0.30	0.55	-1.49E+05	2.23E+10	9.12E+06	3.02E+03
0.30	0.60	9.97E+04	9.94E+09	4.06E+06	2.02E+03
0.30	0.65	3.61E+05	1.30E+11	5.32E+07	7.29E+03

In spite of its low spatial resolution, the GSA (2020) data are adjusted by satellite historical time series data in several spectral channels, environmental variables (altitude, terrain shading, air temperature), atmospheric parameters (water vapor, aerosol optical depth, aerosol type, ozone), Solar-Earth geometry, and advanced algorithms for cloud quantification. Palmer et al. (2018) and Copper and Bruce (2018) evaluated GSA as the most accurate application in comparison with four techniques in the UK and three in Australia, respectively. The information presented in this paragraph justified the adoption of GSA (2020) as observation data for model calibration.

4.2.2. ArcGIS Solar Radiation parameters

The parameters adopted in the ArcGIS Solar Radiation were based on Fu and Rich (1999) and calibration procedures. The pair that generated the solar irradiation model with the minimum RMSE was a diffuse proportion of 0.25 and a transmittivity of 0.60. Thereby, the solar irradiation model (GSD of 50 cm) used for PV Potential analysis was produced using these calibrated parameters.

Fu and Rich (1999) indicated that a 512 x 512 sky size and sky calculation directions of 64 is enough to represent all sky directions. Regarding skymap divisions, the authors recommended a minimum of 16 zenith divisions and 16 azimuth divisions for detailed studies. Regarding the diffuse model adopted in Solar Radiation toolset, as there was no detailed information about irradiance flux coming from specific sky directions, the uniform diffuse model was adopted.

The parameters were divided into three categories: general modeling, topography, and Radiance. Table 2 presents the parameters used in this research.

Table 2. Parameters used in ArcGIS Solar Radiation tools for irradiance modeling of FNI.

Parameter	Value
General modeling parameters	
Latitude	-3.84362
Sky size / resolution	512 x 512
Time configuration	Whole Year
Day and Hour interval	14 and 0.5
Topographic parameters	
Z factor	1
Slope and aspect input	From DEM
Calculation directions	32
Radiance parameters	
Zenith divisions	16
Azimuth divisions	16
Diffuse model type	Uniform Sky
Diffuse proportion	0.25
Transmittivity	0.60

4.2.3. PV and Environmental Potentials assessment

Based on the photointerpretation of the orthophoto, the buildings and open areas were manually vectorized to be used on potential assessment of decentralized and centralized PV sources. The created polygons were used to extract individual solar GHI data of likely installation sites; in sequence, zonal statistics operation was applied to compute the mean GHI values for each polygon feature, as presented in Chiabrando et al. (2017).

The next step was to estimate the PV and Environmental potentials of rooftops and open areas that are suitable for PV power production.

The PV Potential means the electricity yield estimated for a given surface. In this case, it was assumed that the useful surface area (**Asurface**) is delimited by manual vectorization and the average global horizon irradiation (**GHI**) is calculated by the mean GHI value of zonal statistics operations applied on vectorized areas.

Following Fath et al. (2015), the value assumed for PR was 90% and η was 15%.

Eq. 9. PV-Potential = Asurface * GHI * η * PR

The Environmental potential accounted for the emission of carbon dioxide that will be avoided when one energy source is replaced by a renewable. In the context of this research, the oil diesel-burning in thermoelectric would be replaced by PV energy systems.

The avoided quantity of carbon dioxide was calculated based on Equation 10, where it was considered the carbon intensity conversion rate (CI) and the type of energy source. Following the special report from the Intergovernmental Panel on Climate Change by Edenhofer et al. (2011), diesel has a CI of 840 g/kWh.

Eq. 10. Environmental-Potential = PV-Potential * CI

4.3. Phase 3: Scenarios of PV transition for FNI

The photovoltaic transition scenarios in FNI were developed by equalizing the renewable power needed to achieve a transition with scenarios of decentralized and centralized integrated arrangements of PV production in FNI.

The first consist of the sum of the diesel generators electrical production in 2018 (19.4 GWh/yr) and the estimated electrical demand for desalination plants for local islanders (0.8 GWh/yr), a total of 20.2 GWh/yr. In that way, energy and water securities are enhanced in FNI.

In the other side, the integrated arrangements were elaborated assuming that the decentralized sources (PV modules in rooftops) are not able to supply the entire electrical demand. Thus, the remaining power demand will be supplied by the centralized sources (PV plants in open areas).

To quantify scenarios of decentralized PV production, were considered some real-world conditions, for example, not all roofs are capable to physically support the heavy weight of typically commercialized crystalline PV modules, also, not all owners can afford the initial costs or are willing to install PV. Thinking on those, three percentages (25%, 50% and 75%) were considered to account for buildings that would install PV systems. In this case, constructions are selected in crescent order of GHI value.

Besides those factors, building’s rooftops are not entirely occupied by PV modules, so it was suggested three percentages (10%, 25% and 50%) of roof area occupation for PV production. In that way, considering the suggested percentages, 9 scenarios of PV decentralized production were built. For example, the scenario where most of decentralized PV energy is arranged consider that 75% of buildings adopt PV systems and that 50% of their rooftop are occupied by PV modules.

Ultimately, each scenario will indicate the complementary area needed for centralized PV production, which were calculated considering 2.06 MWh/m²/yr (the average GHI value measured in all APA-FNI open areas). Combined with that, the previous PV Potential analysis in open areas guides the decisions about the size and location of centralized PV plants.

To estimate the cost of each scenario, the LCOE (USD/MWh) adopted for decentralized and centralized PV energy production followed the numbers presented by the report IRENA (2020) and the Energy Auction from New Power Generation Projects no. 04/2019 (ANEEL A-6, 2019), respectively. In that way, IRENA (2020) informed that in 2019 Brazilian residential PV systems had an LCOE of 111.00 USD/MWh, therefore used for PV decentralized cost estimation. On the other side, the average sale prices negotiated on the 11 PV power plants projects dealt in ANEEL A-6 (2019) was 20.52 USD/MWh, the value adopted for PV centralized cost estimation.

Worth noting that the scenario planning was based on the principle that installing PV systems in rooftops is more appropriate than in-ground because there will be more social benefits and participation in the PV energy transition if the energy system is decentralized, although it could represent a higher initial capital investment. In addition to that, social and environmental impacts should be minimized inside the APA-FNI and installing PV plants in open areas would implicate in more land occupation, pressure, and conflicts.

Before suggesting locations to install PV plants, it is recommended to follow the environmental zoning and restrictions in the area of study. However, in the APA-FNI case, the orthophoto revealed many irregular occupations and land uses, which prevented the use of zoning as a decision criterion.

5. Results

5.1. Photogrammetric survey

This topic presented the data produced by the photogrammetric survey: an orthophoto with a GSD of 5.3 cm, a DSM resampled to a GSD of 50 cm, and one dense cloud with a point density of 89.2 points/m².

5.1.1. Sparse and Dense point cloud

The recognition of features on a set of overlapped photos was exemplified in Figure 26, which illustrates the true and invalid keypoints matched on two pairs of photos. A true correspondence, that was assigned as a tie point, was represented by blue dashes, while red dashes represent the invalid matches.

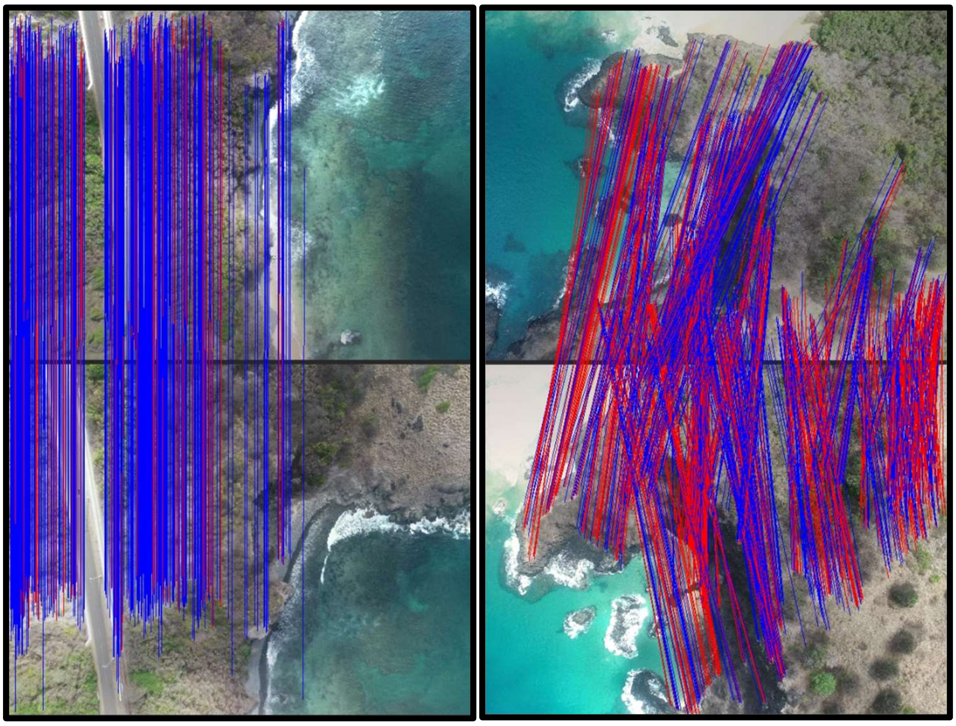

Figure 26. True (blue) and invalid (red) matches on a pair of photos. a) illustrated a pair of photos with 368 matches, from which 368 are true and 113 invalids. b) 1235 matches, from which 524 true and 711 invalids. In the last case, there were no matches over the ocean surface because it is in constant movement, which in consequence obfuscates below-surface targets and disturbs SfM reconstruction. In the first case, there was only one match over the ocean surface.

The tie points calculated in the step of photo alignment composed the 3D sparse cloud. The densification of the point cloud was observed in comparing figures 27 and 28, which illustrate sparce and dense cloud, respectively. In the context of coastal 3D reconstruction, because of shallow and clear water and visible rocks, the software matched some features below the ocean surface. A negative point for coastal areas was that waves and foam disturbed feature recognition procedures and added noise to the 3D model and subsequent DSMs.

However, for urban and infrastructure modeling the focus of this research, the 3D reconstruction was able to model buildings and man-made objects in sufficient detail. For example, Figure 29 presents the point cloud of tilted PV modules of the Noronha II PV Plant and some sloping rooftops.

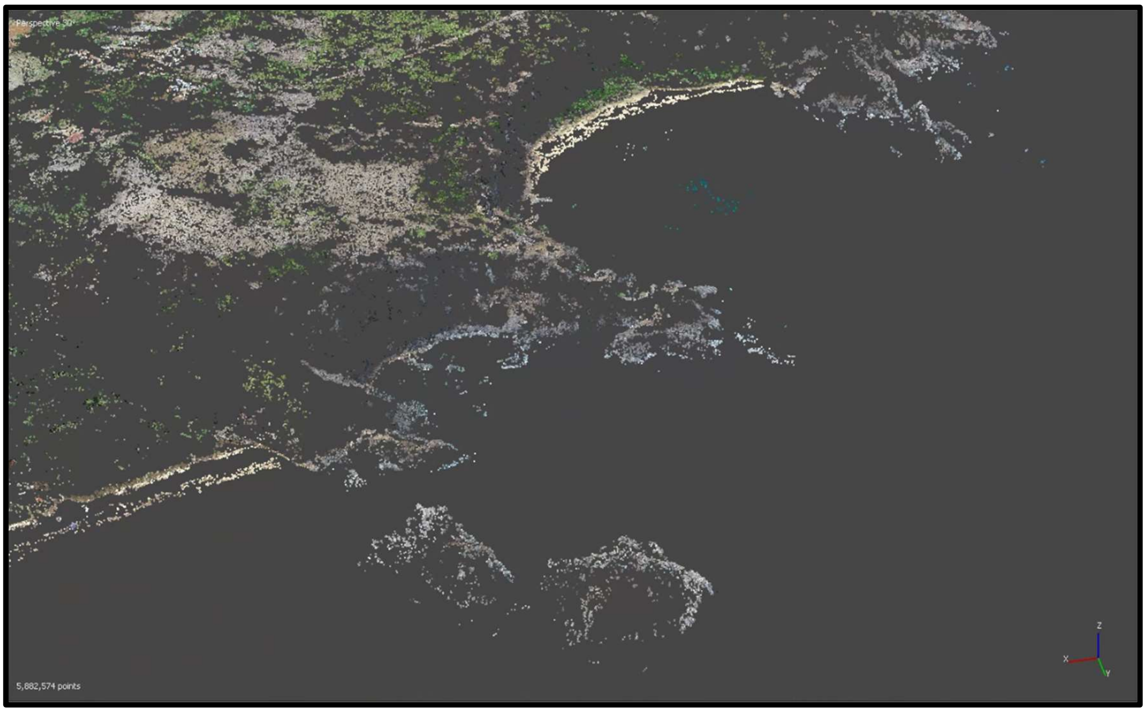

Figure 27. Sparse point cloud of Praia do Sancho, Baía dos Porcos e Praia Cacimba do Padre.

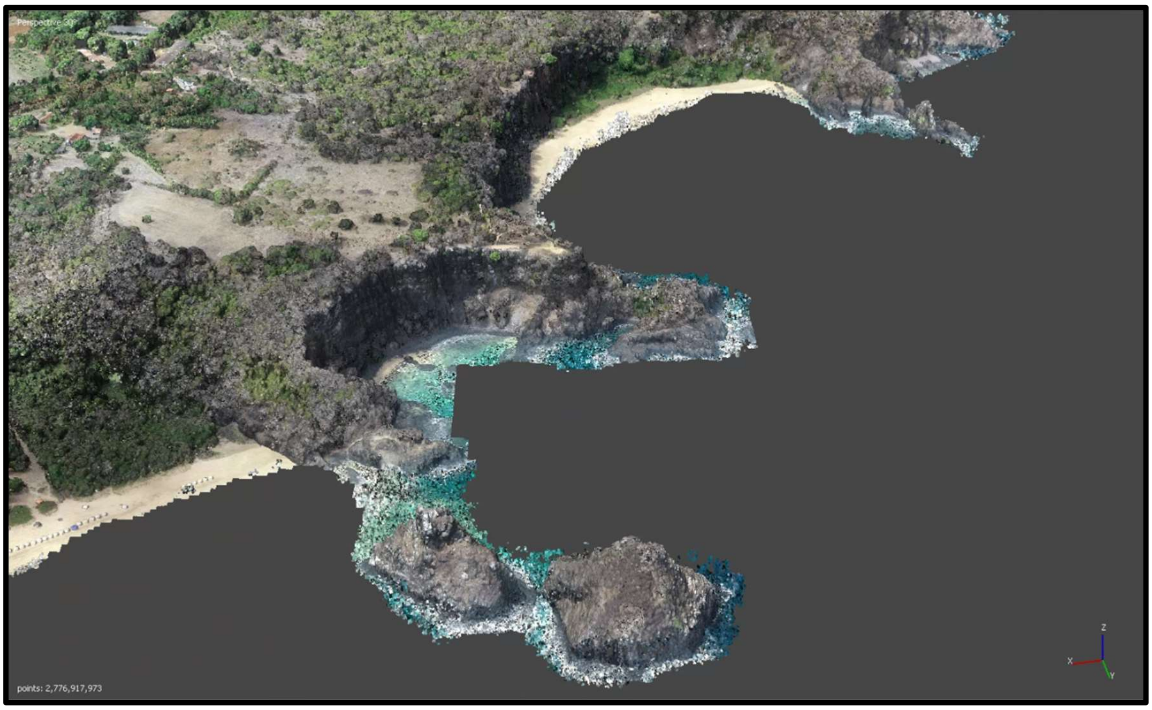

Figure 28. Dense point cloud of Praia do Sancho, Baía dos Porcos e Praia Cacimba do Padre.

Figure 29. Dense point cloud representation of Noronha II PV Plant and sloping rooftop.

5.1.2. Digital Surface Model

The photogrammetric survey produced a DSM with a very refined spatial resolution, with a GSD of 10.9 cm. At this level, the computation of the irradiation modeling takes an unfeasible processing time. Because of that, the DSM was resampled to a GSD of 50 cm, enough for the urban irradiation modeling proposed in this research. Figure 30 presents the DSMs with a GSD of 10.9 cm and 50 cm.

As expected, it was observed that objects above the rooftops (for example trees, water tanks, and fractions of the roof structure itself) were better modeled on higher resolution DSM. It could potentially help to identify objects that increase shading effect and reduce PV feasible installation area. Although it works at the scale of individual PV project installation and dimensioning, it was not the objectives of this research, which focus more on a city scale. Therefore, the reduction in spatial resolution did not affect this study case. Worth noting that a GSD of 50 cm is more refined than typical urban LiDAR surveys.

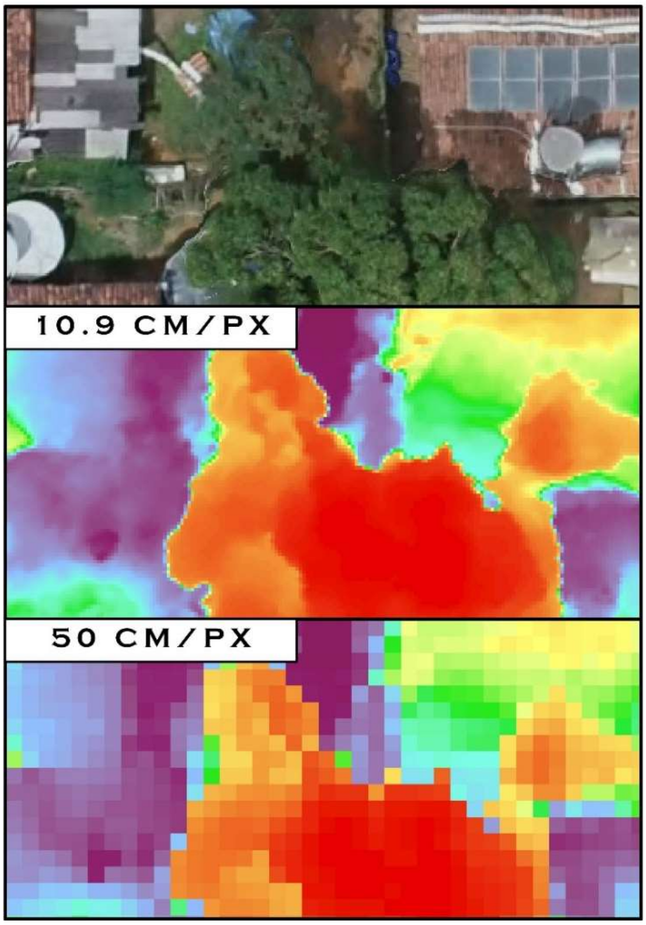

Figure 30. Visual comparison of a DSM with a GSD of 10.9 cm and 50 cm. Worth noting that objects above rooftops, trees and buildings are well represented in both spatial resolutions.

Figure 31 presents the DSM produced for the area covered in FNI ("Morro do Espinhaço" and "Morro do Pico" were not flown by UAV missions). However, considering that the area of interest for PV production is limited to APA-FNI limits, the DSM raster was extracted later to reduce the size of the raster and, in consequence, diminish irradiation modeling processing time.

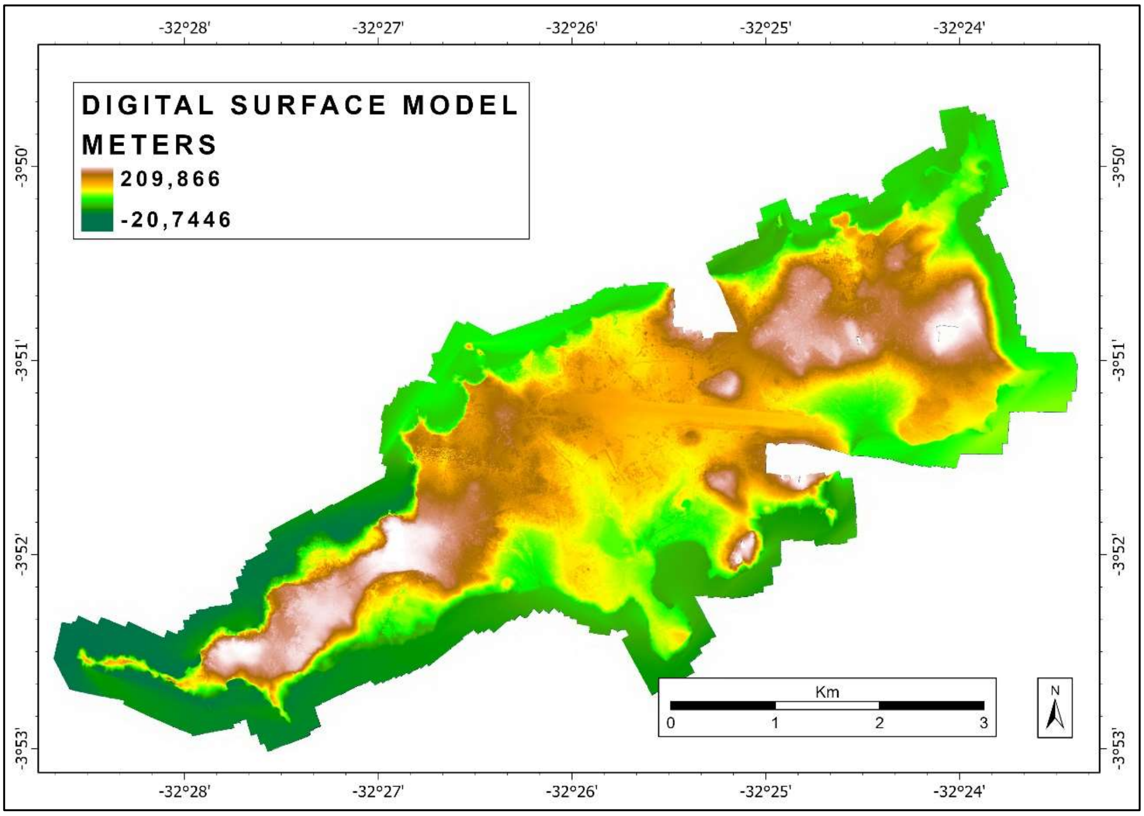

Figure 31. DSM produced by the photogrammetric survey. Although it did not influence PV potential analysis in buildings and open areas, the variation in ocean elevation is caused by erroneous interpolation process in water surfaces and lack of GCP located on extremities of FNI.

5.1.3 Orthophoto.

A few reconstruction failures were noted on the top of some hills. Figure 32 illustrates a sample of a reconstruction failure in "Morro do Medeira". It was caused because of a low number of overlapping photos, which was a consequence of the low flight height in relation to the top of the hill. Although these few holes did not compromise the photogrammetric survey objectives, because they were few and occurred in small areas, they could be avoided by applying a higher percentage of the frontal and side overlap photo collection or higher flight height.

The proposed configuration of 75% longitudinal and 65% lateral overlap could be set to 85% and 75%, for example. Consequently, it would have implicated in more flying time, battery usage, photos acquired, and processing time. In this context, was important to look for an equilibrium in data collection logistics, data processing, and expected final quality.

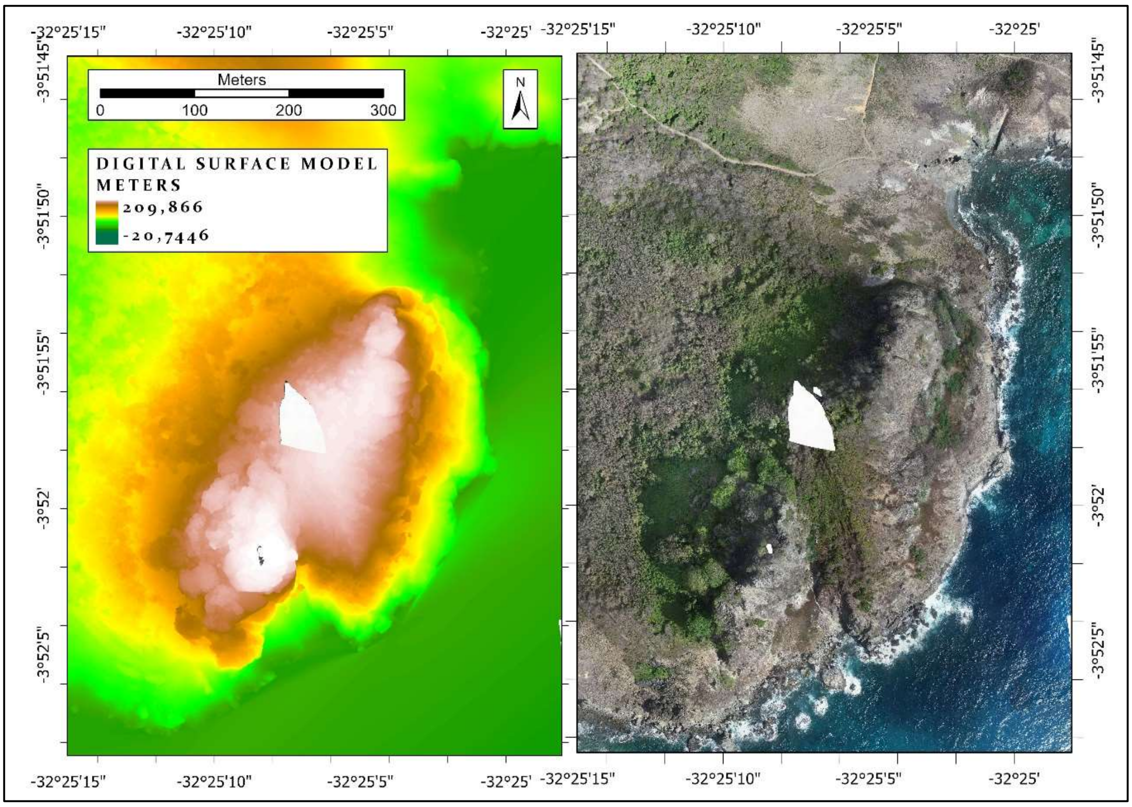

Figure 32. Reconstruction failures identified on Morro do Medeira.

The positional accuracy of the photogrammetric survey was evaluated by calculating the statistic index RMSE, by comparing RTK observed GCP-Checkpoints coordinates with the ones collected in orthophoto. Table 3 presents the calculation of each element of the summation parcel in Equation 7 (8th column in Table 3), which resulted in 0.5295. By solving the Equation 7, the RMSE calculated was 0.155 m.

Table 3 – Positional analysis of the orthophoto.

GCP	E_Ortho	E_GCP	N_Ortho	N_GCP	(ΔE)	(ΔN)	(ΔE)^2 + (ΔN)^2	GCP Root Square Error
1	565938,92	565938,89	9574901,23	9574901,26	0,03	0,03	0,0018	0,0424
2	565883,32	565883,34	9575126,04	9575126,12	-0,02	0,08	0,0068	0,0825
3	565851,24	565851,30	9575283,94	9575283,91	-0,06	-0,03	0,0045	0,0671
4	566067,78	566067,84	9575632,45	9575632,39	-0,06	-0,06	0,0072	0,0849
5	566608,87	566608,87	9576118,51	9576118,52	0,00	0,01	0,0001	0,0100
6	565658,46	565658,52	9574907,30	9574907,16	-0,06	-0,14	0,0232	0,1523
7	565421,05	565421,03	9575469,19	9575469,34	0,02	0,15	0,0229	0,1513
8	565450,14	565450,11	9575218,42	9575218,39	0,03	-0,03	0,0018	0,0424
9	565362,65	565362,62	9574892,18	9574892,22	0,03	0,04	0,0025	0,0500
10	565147,15	565147,10	9574608,08	9574608,06	0,05	-0,02	0,0029	0,0539
11	565375,34	565375,22	9574783,90	9574783,89	0,12	-0,01	0,0145	0,1204
12	565286,61	565286,54	9575078,38	9575078,34	0,07	-0,04	0,0065	0,0806
13	565191,35	565191,31	9574974,27	9574974,34	0,04	0,07	0,0065	0,0806
14	565026,30	565026,29	9574812,46	9574812,45	0,01	-0,01	0,0002	0,0141
15	565016,79	565016,74	9574640,46	9574640,39	0,05	-0,07	0,0074	0,0860
16	564896,12	564896,14	9574755,29	9574755,28	-0,02	-0,01	0,0005	0,0224
17	564763,56	564763,63	9574627,52	9574627,48	-0,07	-0,04	0,0065	0,0806
18	564650,04	564650,07	9574511,04	9574511,00	-0,03	-0,04	0,0025	0,0500
19	564456,47	564456,40	9574404,26	9574404,13	0,07	-0,13	0,0218	0,1476
20	563935,53	563935,84	9574445,97	9574445,84	-0,31	-0,13	0,1130	0,3362
21	563143,72	563144,17	9574761,99	9574761,84	-0,45	-0,15	0,2250	0,4743
22	563482,63	563482,80	9574698,04	9574697,89	-0,17	-0,15	0,0514	0,2267

Eq. 7 Calculation:

$$\text{RMSE} = \sqrt{\sum_{i}^{22} \frac{(\boldsymbol{E}\_Orthophoto_i - \boldsymbol{E}\_GCP\_Checkpoint_i)^2 + (N\_Orthophot_i - N\_GCP\_Checkpoin_i)^2}{22}} =$$

$$\text{RMSE} = \sqrt{\frac{0{,}5295}{22}} = 0.155$$

Figure 33 presents the spatial distribution of the 22 GCP-Checkpoints adopted in this research. It was noted that the 3 GCPs-Checkpoints placed behind Morro do Pico (20, 21, and 22) had the largest errors (33.6 cm, 47.4 cm, and 22.7 cm, respectively), which can be justified by the interference in the link-communication between the base and the hover in the RTK survey caused by the “Morro do Pico” topographic obstruction, as shown in Figure 37. Although this positional error is relatively low for the purposes of this case study research, we could get better results by adding intermediate RTK bases. Moreover, the 19 (1 to 19) GCP-Checkpoints measured without any topographical interference had RMSE of 8.5 cm. Figure 34 represent the error distribution of GCP-Checkpoints.

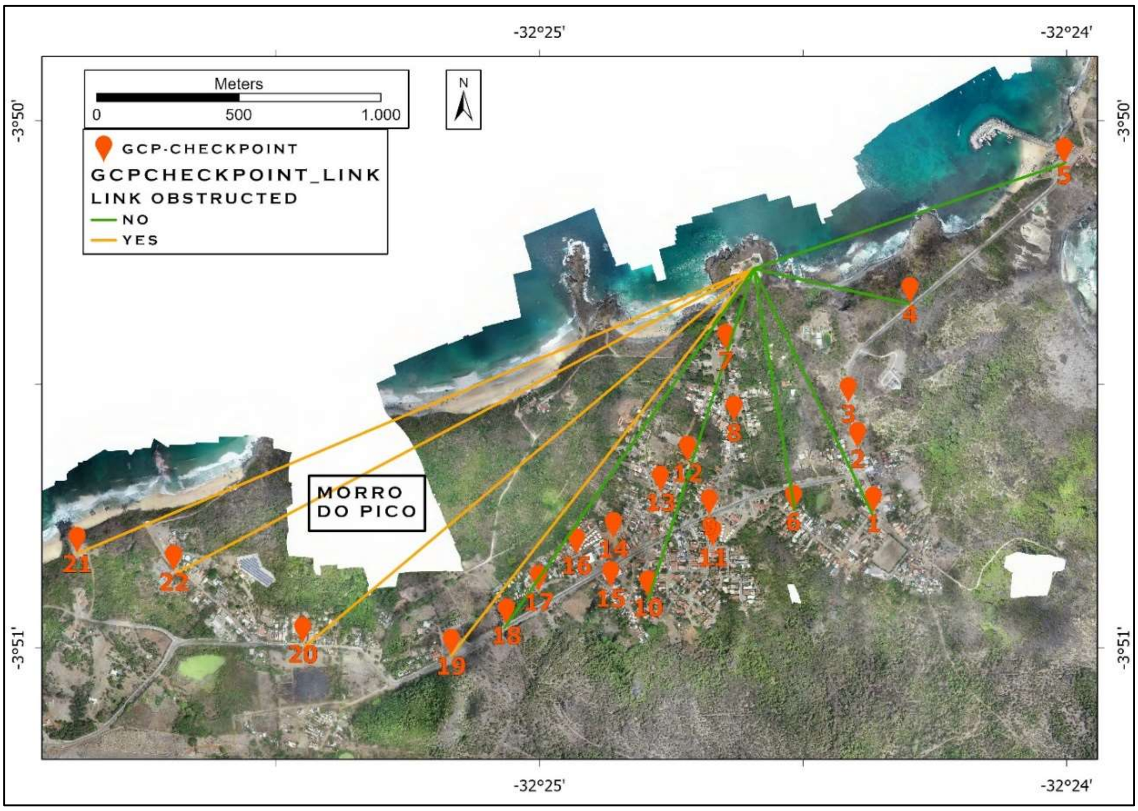

Figure 33. Distribution of 22 GCP-Georeferencing inside APA-FNI.

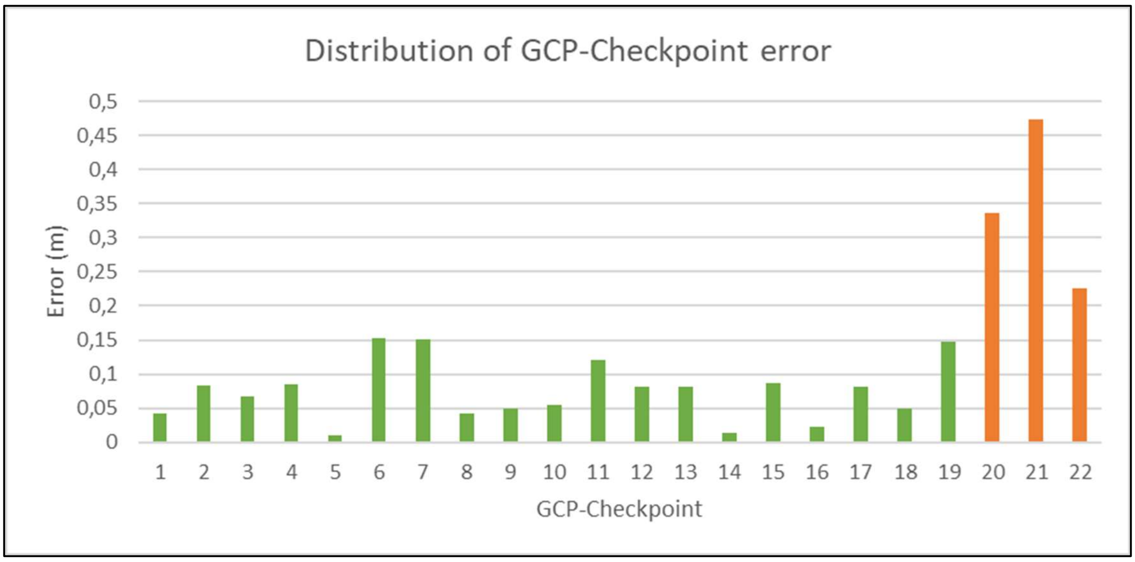

Figure 34. Distribution of errors in GCP-Checkpoints.

Ultimately, the positional accuracy achieved in this case study was satisfactory, considering the purposes of GIS irradiation modeling and scenarios of PV transition.

The vectorization process of buildings and open areas was performed manually and aimed to account for centralized and decentralized areas suitable for PV production. To this extent, by interpreting the orthophoto, were identified 1,272 roofs and 26 open areas, accounting in total 199,743 m² and 239,603 m² of potential areas to install PV modules, respectively. Among the open areas, 9 have more than 10,000 m², with the largest having 39,740 m². In regards of roofs, 40 have more than 500 m². Figure 35 presents the results of the vectorization.

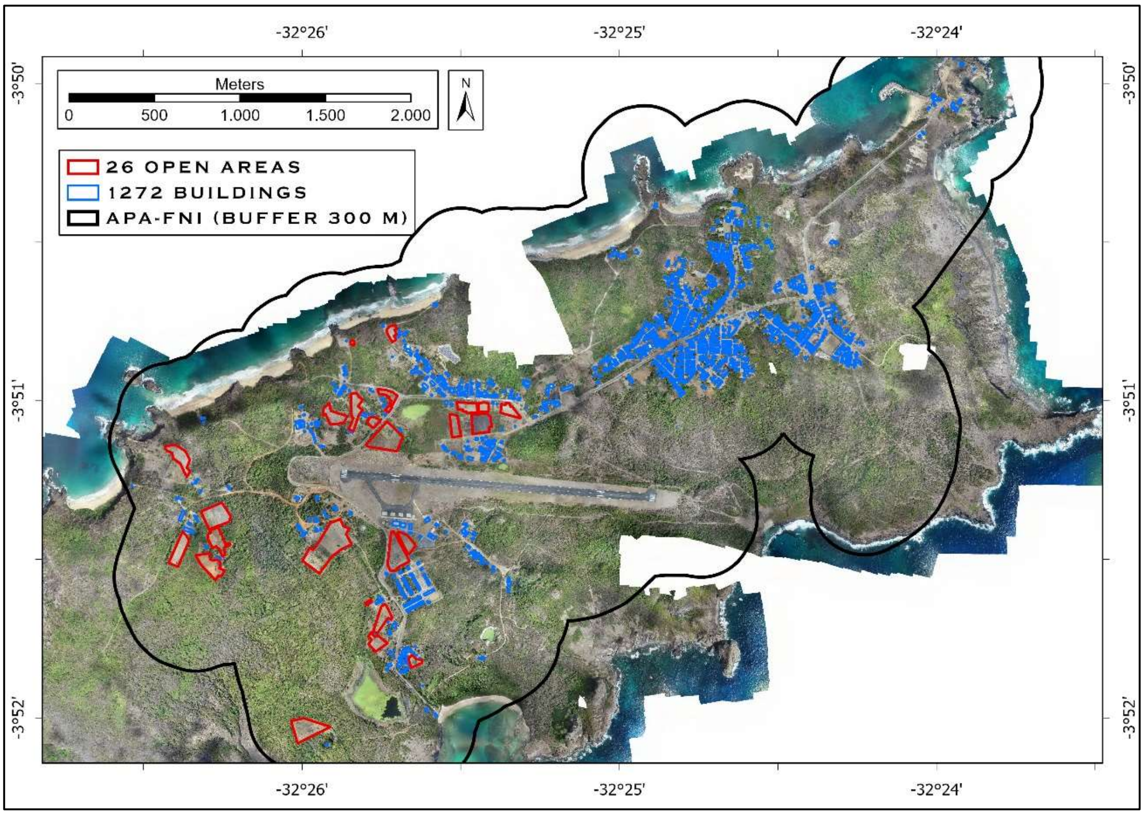

Figure 35. Vectorization of buildings and open areas, the surfaces considered to produce decentralized and centralized PV energy, respectively.

The high spatial resolution of orthophotos produced by UAV SfM-MVS photogrammetry new solutions and applications for mapping and remote sensing. In this case, with a GSD of 5.3 cm, the orthophoto can be used by urban administrators for infrastructure (roads, harbor, airport, landfills, buildings) inspection, monitoring of construction and development sites, documentation of historic and archeological features, territorial/land management, sustainable tourism and agricultural planning, and GIS database for cadastral and thematic maps. In conjunction, environmental managers of park and protected areas can use the data for ecosystems (coastal, vegetation, waterbodies) and natural resources assessment, erosions monitoring, land use classification and change detection analysis, environmental impact analysis, planning and monitoring of sustainable actions, nursery grounds assessment, among others.

As a remote sensing technique, the UAV photogrammetry produced a map with exceptional positional accuracy and impressively detailed, was able to survey *“on demand”*, and demonstrated to be practical, effective, and with great cost-benefit.

5.2. Open area and rooftop irradiation modeling and PV potential assessment

The irradiation model produced for APA-FNI, with a GSD of 50 cm, is presented in Figures 36, 37 and 38. The irradiation data extracted by masks of buildings and open areas are presented with a better scale in figures 39 and 40. As expected, the highest values were obtained on flat surfaces and distant from shading structures (trees, buildings, or hills). For example, pixels with maximum irradiation were found on the airport runway, clearings in vegetation areas, small water dams, parts of the main road, unshaded roofs, and in the sea. In opposition, the minimum values were found on steep surfaces, beaches surrounded by cliffs and places adjacent to hills, houses, and trees.

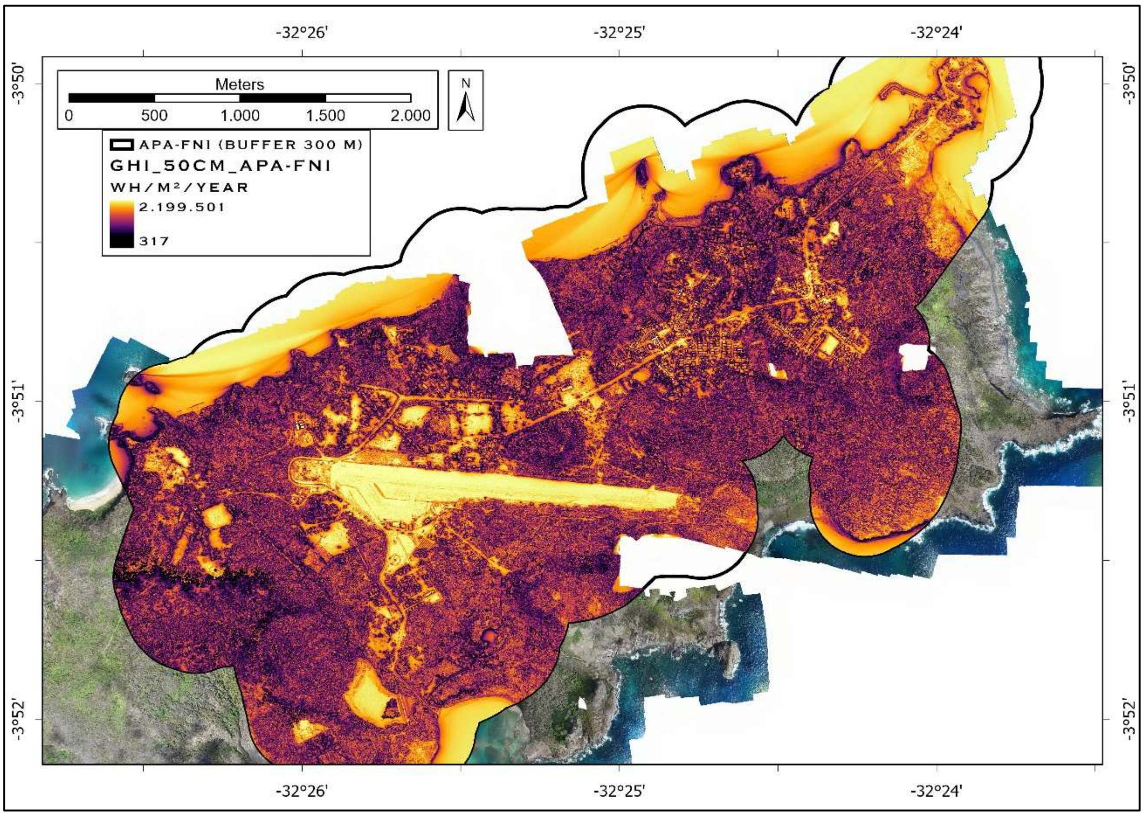

Figure 36. Irradiation model of APA-FNI.

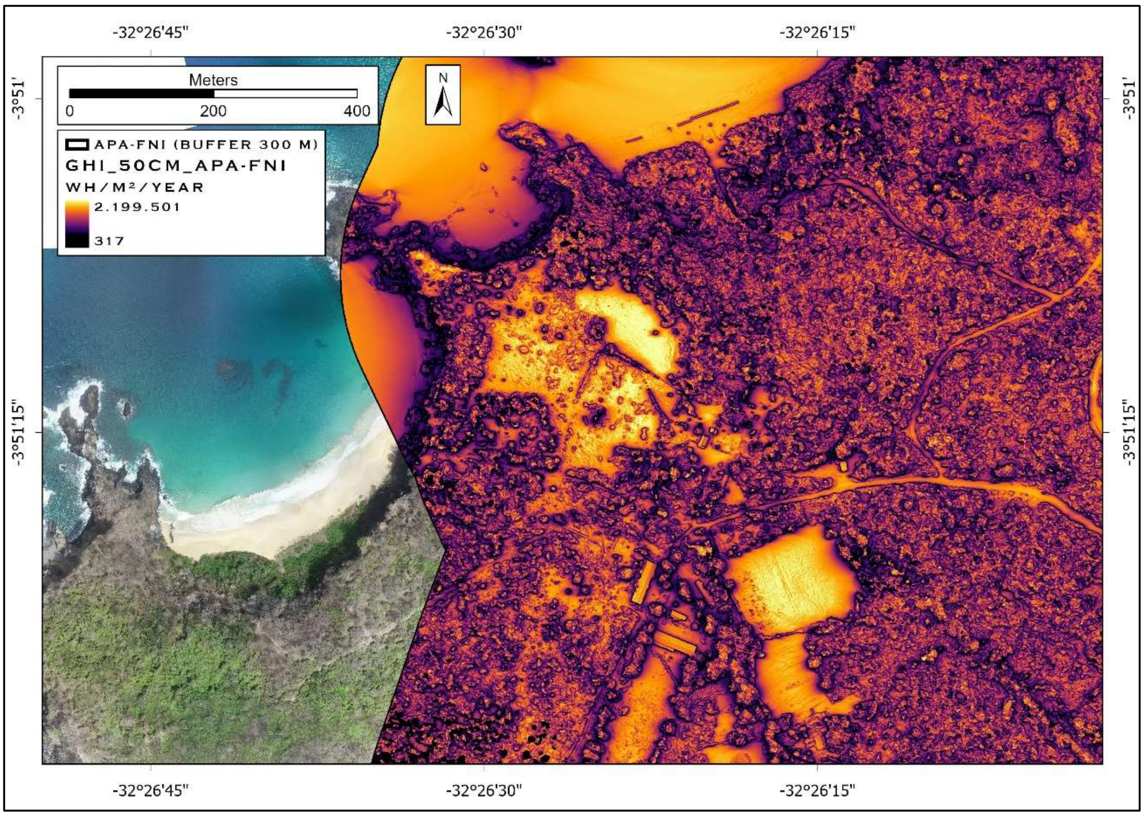

Figure 37. Irradiation map of the same areas represented by point clouds in figures 27 and 28. The high irradiation open area in the southwest position is a plantation area, and the one near the center is a cleared and low vegetation area. Beaches and hills have lower irradiation because of cliff shading and steep terrain slope.

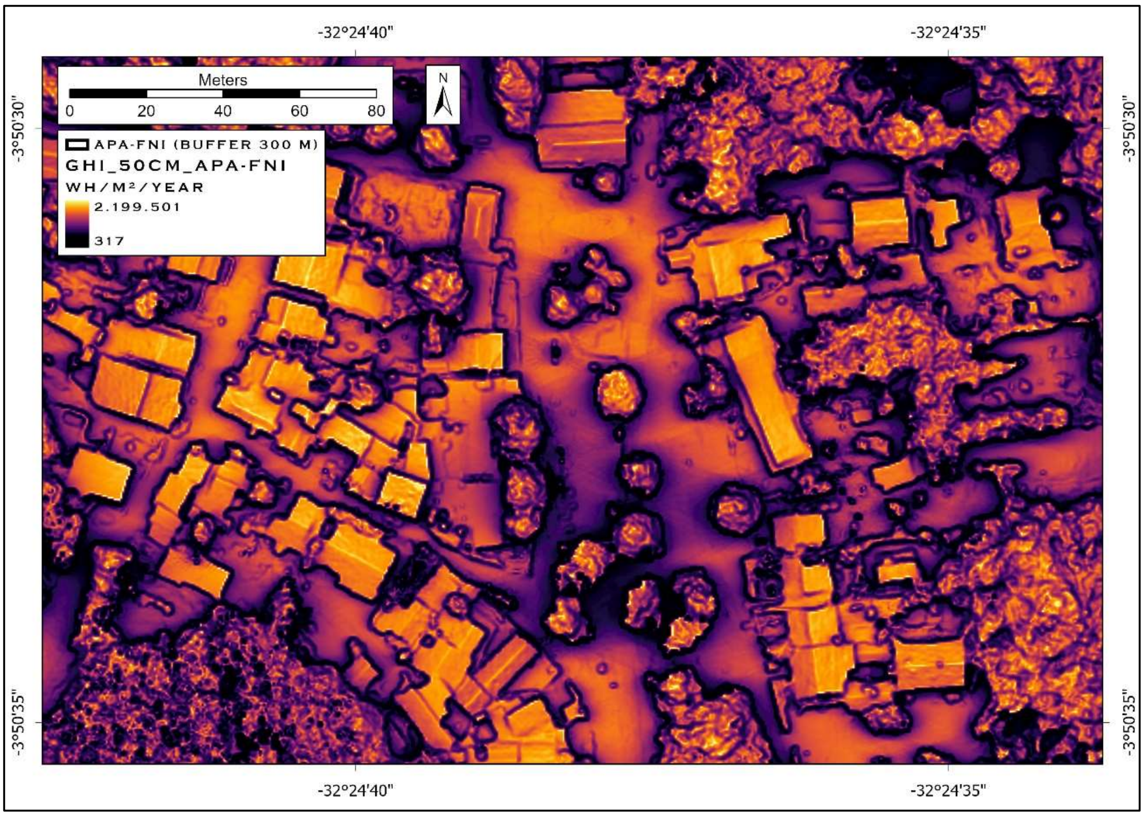

Figure 38. Irradiation map of sector in Vila dos Remédios neighborhood. It is notable that GHI varies because of the shading caused by trees and buildings and due to variation in slope and orientation of the surfaces.

Figure 39. Irradiation data extracted by building vectors.

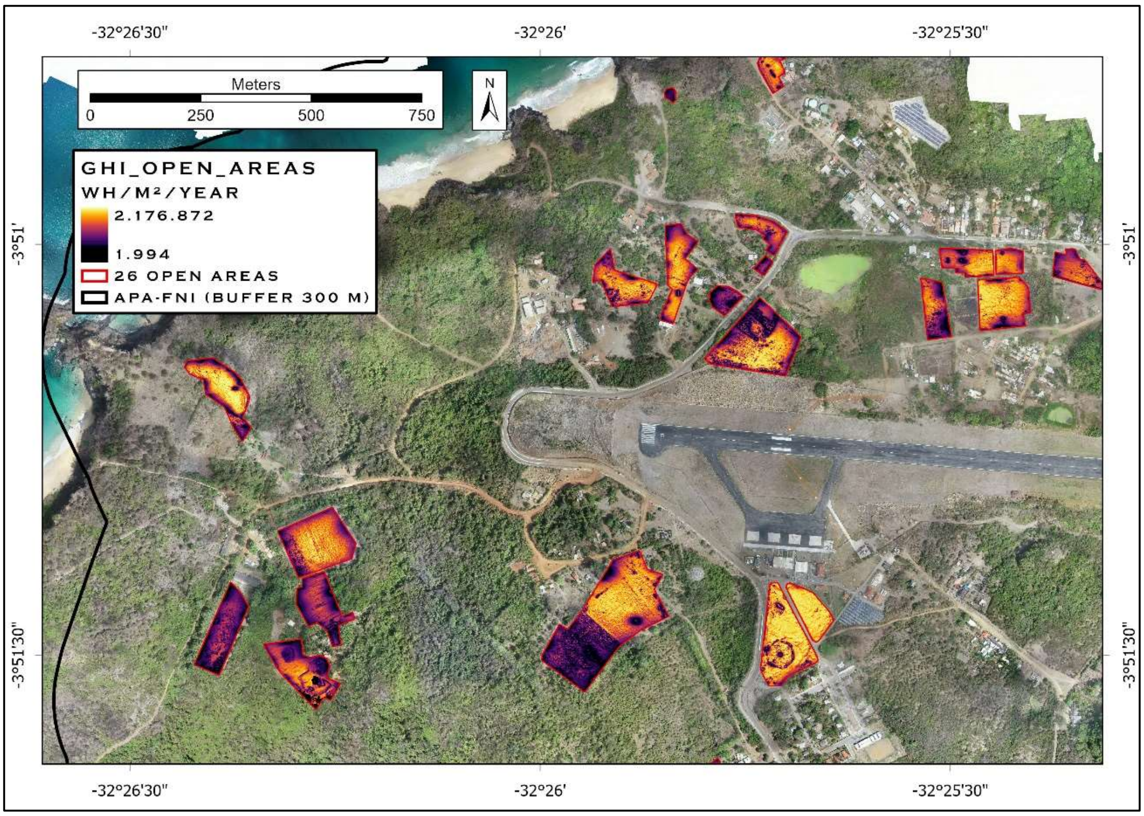

Figure 40. Annual Irradiation data extracted by open area vectors.

The Total Decentralized PV-Potential estimated for the 1272 buildings was 51.6 GWh/yr, corresponding to an Environmental-Potential of 43344 tons of CO_2-eq. Likewise, the Total Centralized PV-Potential estimated for the 26 open areas was 67.0 GWh/yr, and an Environmental-potential of 56028 tons of CO_2-eq. The combined Total PV-potential of decentralized and centralized sources, 118.6 GWh/yr, is almost 5.8 times the annual power consumption for a sustainable transition, 20.2 GWh/yr. Worth remember that 20.2 GWh/yr represents the annual power produced by Tubarão Diesel Plant in 2018 (19.4 GWh/yr) coupled with the power required to produce potable water for local people, with reverse osmosis membrane treatment (0.8 GWh/yr).

Summing up the PV-Potential of the four largest open areas in APA-FNI, 26.25 GWh/yr, and taking a 5% rate discount because of the area occupied by modules spacing and access corridors, reveals that a PV transition is feasible only with those four open areas. With a different point of view, APA-FNI must explore only 17% of its Total PV-Potential to achieve a renewable transition. Those affirmations are important to demonstrate and motivate the society to plan and pursue a renewable energy transition.

To give an example of the output results of Equations 9 (PV-Potential) and 10 (Environmental-Potential), Table 4 presents the data of the 10 largest rooftops and open areas of FNI. Figure 41 presents the PV-Potential of some open areas.

Table 4. PV-Potential and Environmental-Potential of the 10 largest rooftops and open areas of FNI.

Open areas				**Rooftops**			
AREA (m²)	Mean GHI (MWh/m²/yr)	PV-Pot (GWh/yr)	Env. Pot (ton CO2-eq/yr)	AREA (m²)	Mean GHI (MWh/m²/yr)	PV-Pot (GWh/yr)	Env. Pot (ton CO2-eq/yr)
39780	2.03	10.90	9157	3001	1.99	0.81	677
20625	2.07	5.76	4841	1464	1.92	0.38	319
17331	2.08	4.87	4088	1181	2.06	0.33	276
16328	2.14	4.72	3962	1115	1.96	0.29	248
16183	2.13	4.65	3909	1110	1.86	0.28	234
12237	1.98	3.27	2748	1055	2.00	0.28	239
11543	2.13	3.32	2788	1016	2.11	0.29	243
10955	2.09	3.09	2596	958	2.13	0.28	232
10643	1.97	2.83	2378	923	2.01	0.25	211
9811	2.03	2.69	2259	899	2.00	0.24	204

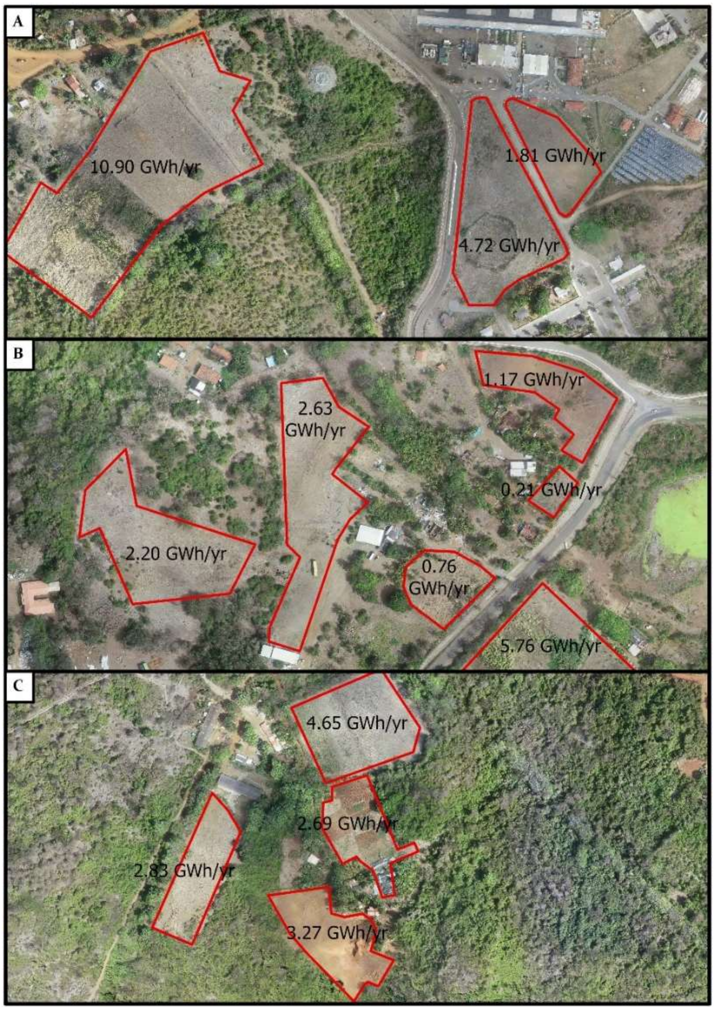

Figure 41. PV-Potential of some open areas in APA-FNI.

It is important to mention that some of these areas were cleared for agricultural purposes, but they could be strategically developed to PV greenhouses, like the 2 GWh/yr in Reunion Island (Scognamiglio et al., 2014), or to stilt-mounted *agrivoltaic* systems (Sekiyama and Nagashima, 2019). Those kinds of solutions could make a more efficient and intelligent use of the available surfaces to enhance at the same time energy and food securities.

As stated in methodology, environmental zoning in APA-FNI was not considered as a location criterion because of many irregular occupations and uses found in there. For example, were found recent earthwork activities, buildings, and agricultural fields inside zones of Conservation and Wildlife Protection, meaning that the environmental zoning is not being followed or it is outdated. Worth mentions that some open areas that were identified in this study are also inside those zoning areas. Moreover, the APA-FNI management and zoning plan does not discuss land use for the production of renewable energy.

Although some areas are extensive and have high irradiation and PV-Potential, they were not considered suitable for installing centralized PV plants and, therefore, were neglected on this study case. For example, the area aside the runway airport (200000 m²) was not contemplated because of sunlight reflex during aircrafts landing. Due to preservation of vulnerable ecosystem, the dunes (100000 m²) located at Northeastern side of APA-FNI were also neglected. Moreover, the soccer field (5000 m²) was also excluded because the community uses it for sports and meetings.

To exemplify the monthly variation in GHI, Figure 42 presents the monthly GHI of two sample buildings. It is notable that between March and September the rooftops facing North have higher GHI. However, between October and February the ones facing South have higher GHI. This happens because FNI is near the Equator Line (latitude of 3°S) and the Sun-rising position vary throughout the year (represented by positions of equinox and summer/winter solstice), in that way, between March and September the Sun rises above the Zenith Angle of a rooftop in FNI, favoring GHI in northern oriented faces, and between October and February it rises below, favoring southern oriented faces.

By simply visual analyzing the annual GHI in FNI (figures 38, 39, and 42), it was observed that the orientation of the rooftop (pointed to north or to south) is not as significant as the shading caused by trees and objects above surface and roofs. This means that the GHI at high spatial resolution (GSD of 50cm) was a key data for estimating accurately the PV-Potential in rooftops because they compute the attenuation caused by shading objects.

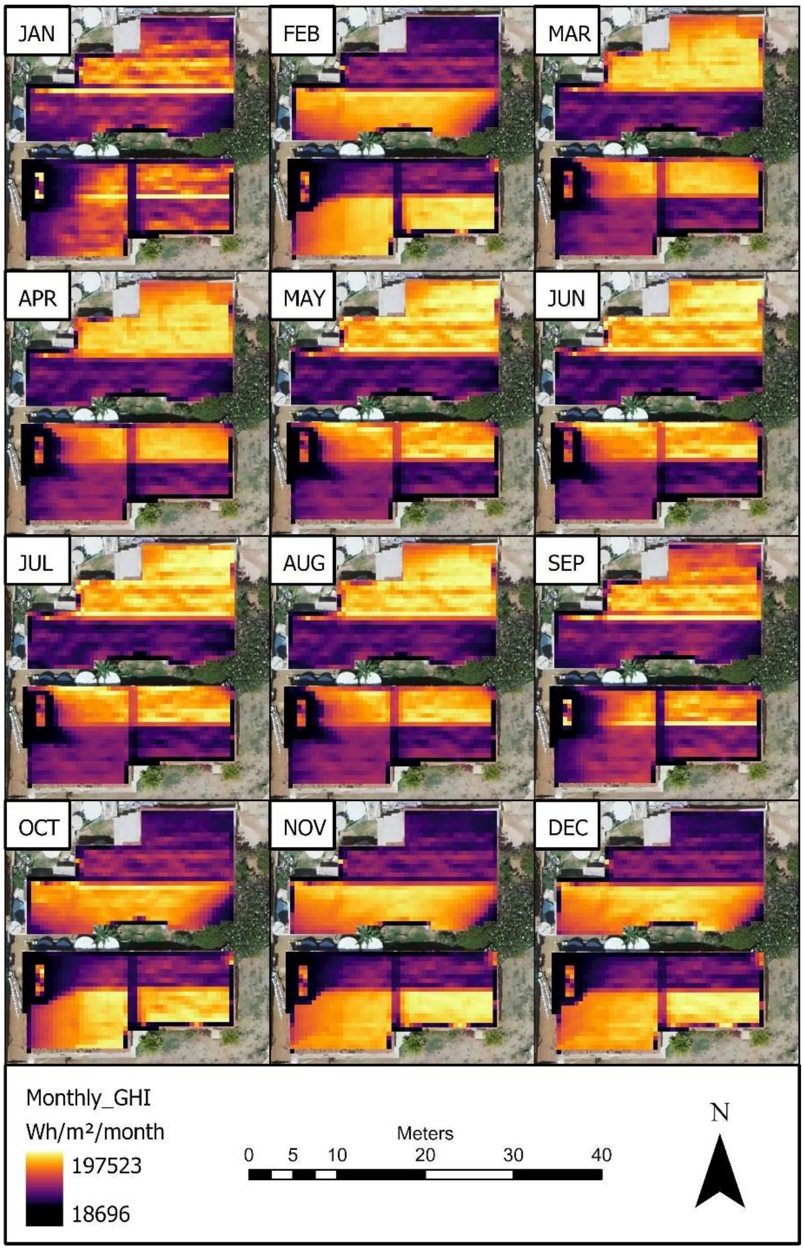

Figure 42. Monthly GHI in two sample buildings to illustrate the GHI variation throughout the year in rooftop faces oriented to north and south. Between March and September, GHI is higher in faces pointing north. Between October and February, GHI is higher in faces pointing south.

Despite not having historical data measured by pyranometers to validate irradiance values estimated in this research, which is highly recommended, it was observed that flat and unshaded areas, like the ocean and water reservoir surface, airport runway and most cleared open areas, had relatively similar irradiation values compared to the data provided by GSA (2020), between 2100 and 2200 kWh/m². Minding that GSA (2020) data is trustable but does not account for high spatial resolution shading effect, it is believed that the calibration procedures achieved its purposes, meaning that the GHI model produced can be trusted and applied in PV-Potential analysis.

Thinking of a way to share the mean GHI of rooftops in FNI, two shapefiles were added to a web GIS application. The first contained the 1272 rooftop buildings footprint (polygon vectors), presented in Figure 35. The second one was produced by transforming the raster GHI into a shapefile of points, with distance between points of 50 cm (same as the GSD of the GHI raster). The link to access the web GIS platform is: https://arcg.is/5D044 . Because of the server maintenance expenses, the platform may be unavailable in the future.

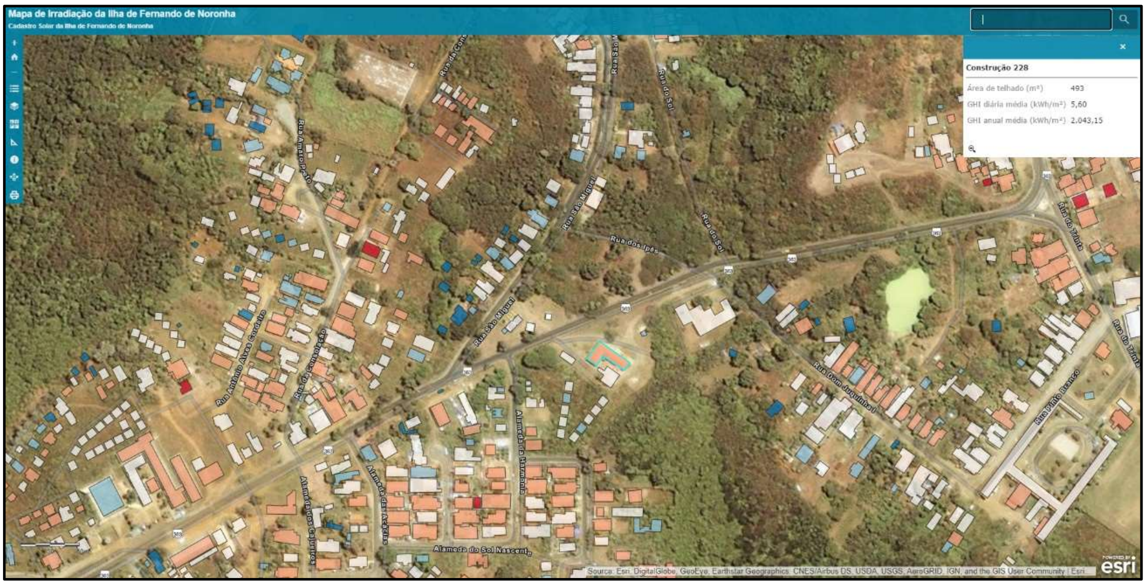

Construção 228

Área de telhado (m²) 493

GHI diária média (kWh/m²) 5,60

GHI anual média (kWh/m²) 2.043,15

Source: Esri, DigitalGlobe, GeoEye, Earthstar Geographics, CNES/Airbus DS, USDA, USGS, AeroGRID, IGN, and the GIS User Community | Esri

Figure 43. Web GIS platform. Clicking on a building footprint opens a pop-up window informing area and mean annual and daily GHI.

Source: Esri, DigitalGlobe, GeoEye, Earthstar Geographics, CNES/Airbus DS, USDA, USGS, AeroGRID, IGN, and the GIS User Community | Esri

Figure 44. Web GIS platform. Zooming in will show the shapefile of points informing the annual GHI in rooftops.

5.3. Suggestion of scenarios of PV transition

The scenarios of PV transition present possible arrangements that integrate decentralized and centralized PV sources, considering the percentages of houses that will install PV systems (25%, 50%, 75%) and the rooftop area occupied by them (10%, 25%, 50%).

In that way, to produce 20.2 GWh/yr of renewable power to achieve energy transition, the 9 possible scenarios of decentralized PV energy production were complemented by centralized PV plants. Table 5 presents the results of this integration.

Table 5. Scenarios of renewable transitions considering decentralized and centralized PV sources.

Scenario	Buildings with PV systems (%)	Area occupied by PV modules in rooftops (%)	Decentralized rooftops useful area (m²)	Decentralized rooftops annual PV-Potential (GWh)	Centralized PV plants complementary annual PV-Potential (GWh)	Centralized PV plants area required (m²)	Degree of decentralization (%)	Scenario cost estimation (thousand US dollars)
A	25	10	6204	1,7	18,5	66443	8,5	550
B	25	25	15512	4,3	15,9	57237	21,1	754
C	25	50	31024	8,5	11,7	41894	42,3	1093
D	50	10	12075	3,3	16,9	60829	16,2	674
E	50	25	30187	8,2	12,0	43202	40,5	1064
F	50	50	60375	16,4	3,8	13823	81,0	1714
G	75	10	16414	4,4	15,8	56797	21,7	764
H	75	25	41035	11,0	9,2	33121	54,4	1287
I	75	50	82071	22,0	-1,8	0	108,7	2160

Scenario “I”, whereas the decentralized sources are most integrated, highlights that a decentralized rooftop PV system in FNI can produce 108% of the electricity required to achieve a renewable transition, a surplus of 1.8 GWh/yr. In the other side, scenario “A” needs to be complemented with 18.5 GWh/yr, i.e., 66443 m² of useful area of centralized PV plants. Moreover, the midway Scenario “E” needs that complementary centralized PV plants produce 12.0 GWh/yr.

As predicted, scenarios with the largest share of decentralized sources had a higher cost than those with the highest share of centralized sources. Scenario “A” had an estimated cost of 550 thousand USD, scenario “E” 1064 thousand dollars, and scenario “I” 2160 thousand dollars. In that way, an 100% decentralized PV energy transition - Scenario “I” - can cost almost four times a less decentralized PV transition – Scenario “A”. Worth highlighting that the analysis of cost estimation is particularly important for the viability of renewable energy transitions, however different aspects must also be considered, for example environmental restrictions for land occupation, public hearings about the degree of decentralization and social engagement, rooftops and soils technical viabilities, among others. Moreover, particularly for FNI, it is important that tourists, the largest source of income, have a good impression of the participation of islanders in the production of renewable energy and their commitment to sustainability and preservation of the environment. Therefore, the scenario cost is not the most important aspect on an energy renewable transition.

The decisions regarding the locations and sizes of centralized PV plants are supported by the previous analysis that identified and estimated the PV-Potential of open areas in APA-FNI. For example, the centralized PV power needed in scenario "C" (11.7 GWh/yr) could be located on the three open areas near the airport and the PV Plant Noronha II (Figure 41.a), which have a combined PV Potential of 17.4 GWh/yr. Worth noting that is recommended to discount a 5% rate in calculation of available centralized PV Potential because of the area required for spacing between modules, access roads, parking lots, and structures needed on PV plants. With that in mind, the useful combined PV Potential of that areas are 16.5 GWh/yr.

However, the centralized PV potential can be interpreted with a different point of view. The mentioned 16.5 GWh/yr is enough to fulfill the scenarios B, C, E, F, G, H, and I. This approach is recommended if areas are somehow preferred due external factors, such as the distribution network location, environmental zoning and legislation, development plans, or if there are pavemented roads to access the areas.

Worth remembers that the scope of this study was limited to GHI modeling and analysis to suggest scenarios that produce more PV energy than the power consumed annually. It was out of the boundary to discuss fundamental aspects of a renewable energy transition, such as battery storage systems, other renewable energy sources, mismatch daily power consumption, smart grids, among others.

However, in terms of renewable power and transitions plan, smart and sustainable islands or cities should have hybrids renewable energy systems (wind-solar, wind-solar-hydro, wind-solar-oceanic, etc.) to take advantage of the concept of complementarity among renewable sources. Moreover, a smart-grid system coupled with an energy battery storage system must be dimensioned properly to solve the mismatch between the grid load demand and the variability in renewable power production. If a complete storage system is not feasible (because of high initial costs), diesel generators that already exists could be minimally integrated to control the grid load, since they have a flexible operation, good ramp capability (control of increasing/decreasing output power), and a short time to start-up/shutdown the system. The topics presented in this paragraph were out of the scope of this study but are recommended as future research.

6. Conclusions

The workflow proposed in the present research demonstrated that the integration of UAV photogrammetry and GIS solar irradiation modeling and PV potential analysis produce applicable data and solutions in the context of smart and solar cities, contributing for smarter, faster and more socially engaged PV transition.

Although this study case took place on a remote island environment, with an isolated power system, the workflow could be replicated in several scales and almost any environment. For example, isolated communities in forests, islands, and arid regions, whole cities connected to national power systems, specific zoning areas (residential, commercial, industrial, recreative), and private enterprises (agricultural and rural properties, hotels, factories, among others).

It was demonstrated that UAV photogrammetry worked fine on mapping a 2000 ha area and was capable of produce GIS data with high spatial resolution and positional accuracy. As a remote sensing technique, considering the on-demand and high-quality mapping results achieved in this case study, UAV photogrammetry had excellent cost-effectiveness and practicality. The technique is substantial and directly contribute to innovations and solutions on GIS and remote sensing fields.

Moreover, the high spatial resolution survey was particularly important for irradiation modeling and PV potential analysis at the scale of buildings and open areas because it was possible to accurately model shading tracks caused by trees, buildings, above-rooftop objects, among other surface elements. Although none ground truth pyranometer data was used to validate the irradiation modeling (recommended for future research), the estimation was considered reliable because GHI calibration procedures for atmospheric attenuation were applied and verified.

Worth noting that irradiation models could be somehow used by almost all energy stakeholders (individual consumers, small neighborhoods, public administrators, power companies, shareholders, entrepreneurs, non-governmental organizations). The high-resolution irradiation model could also be used in best-location and decision-makings process of different technologies, such as PV light poles, PV integration with water desalination and wastewater treatment plants, electric car station, agrivoltaics systems, PV wide-spread projects funding, among others.

The results of this research indicate that the FNI can achieve a renewable energy transition, powered by centralized and decentralized PV sources located in APA-FNI. It was estimated that the PV systems used to achieve the renewable energy transition cost between 550 and 2160 thousand US dollars, depending on the degree of decentralization.

For a small island like FNI, it is important to highlight that achieving a renewable energy transitions means (i) an improvement of energy and water security, (ii) a reduction of water and energy costs and of environmental impacts and risks, (iii) an efficient use and management of natural resources, (iv) a strengthening in economic, social, and environmental aspects, and (v) more publicity and revenues for sustainable tourism.

Nonetheless, the spatial data (orthophoto, DSM, and GHI) produced in this research could be used by ICMBio and ADEFN for (i) inspection, management, protection and preservation of urban and environmental assets and resources, (ii) monitoring and planning of efficient uses and occupations of the territory, (iii) Planning, developing and looking for funding projects of sustainable renewable energy, sustainable and smart cities, community-based agriculture, ecotourism, environmental preservation, archaeological, among others, and (iv) facilitate future research.

7. References

ABSOLAR - Brazilian Association of Photovoltaic Energy. Infographic. ABSOLAR n 17. 2019. Available on: <http://www.absolar.org.br/infografico-absolar-.html> Accessed in March 2020.

ADELEKE, Adedayo Kelvin. Web-based GIS modelling of building-integrated solar photovoltaic system for the City of Cape Town. 2018. **PhD Thesis. University of Cape Town.**

AGISOFT LCC. Agisoft Metashape User Manual: Professional Edition, Version 1.5. 2019.

AGÜERA-VEGA, Francisco; CARVAJAL-RAMÍREZ, Fernando; MARTÍNEZ-CARRICONDO, Patricio. Assessment of photogrammetric mapping accuracy based on variation ground control points number using unmanned aerial vehicle. **Measurement**, v. 98, p. 221-227, 2017.

ALBERTZ, Jörg. Albrecht Meydenbauer-Pioneer of photogrammetric documentation of the cultural heritage. **International Archives of Photogrammetry Remote Sensing and Spatial Information Sciences**, v. 34, n. 5/C7, p. 19-25, 2002.

ALBINO, Vito; BERARDI, Umberto; DANGELICO, Rosa Maria. Smart cities: Definitions, dimensions, performance, and initiatives. **Journal of urban technology**, v. 22, n. 1, p. 3-21, 2015.

ANDERSON, Karen; GASTON, Kevin J. Lightweight unmanned aerial vehicles will revolutionize spatial ecology. **Frontiers in Ecology and the Environment**, v. 11, n. 3, p. 138-146, 2013.

ANEEL - Brazilian Electricity Regulatory Agency. "**ANEEL Normative Resolution Nº 482, 17th April 2012**". 2012. Available on: <http://www2.aneel.gov.br/cedoc/ren2012482.pdf>. Accessed in December 2019.

ANEEL A-6. "**Energy Auction from New Power Generation Projects (A-6 of 2019)**". Brazilian Electricity Regulatory Agency, in partnership with the Electric Energy Trading Chamber. October 2019. Available on: < https://www2.aneel.gov.br/aplicacoes/editais_geracao/documentos/Resultados-do-Leilao_4-2019_30len_a6.pdf> and <https://www.ppi.gov.br/new-energy-auction-len-a-6-of-2019>. Accessed in January 2021.

BALUJA, J.; DIAGO, M. P.; BALDA, P.; ZORER, R.; MEGGIO, F.; MORALES, F.; TARDAGUILA, J. Assessment of vineyard water status variability by thermal and multispectral imagery using an unmanned aerial vehicle (UAV). **Irrigation Science**, v. 30, n. 6, p. 511-522, 2012.

BENDIG, J.; YU, K.; AASEN, H.; BOLTEN, A.; BENNERTZ, S.; BROSCHEIT, J.; GNYP, M.; BARETH, G. Combining UAV-based plant height from crop surface models, visible, and near infrared vegetation indices for biomass monitoring in barley. **International Journal of Applied Earth Observation and Geoinformation**, v. 39, p. 79-87, 2015.

BERGAMASCO, Luca; ASINARI, Pietro. Scalable methodology for the photovoltaic solar energy potential assessment based on available roof surface area: Application to Piedmont Region (Italy). **Solar energy**, v. 85, n. 5, p. 1041-1055, 2011.

BESSER, A.; KAZAK, J. K.; ŚWIĄDER, M.; SZEWRAŃSKI, S. A Customized Decision Support System for Renewable Energy Application by Housing Association. **Sustainability**, v. 11, n. 16, p. 4377, 2019.

BILJECKI, F.; STOTER, J.; LEDOUX, H.; ZLATANOVA, S.; ÇÖLTEKIN, A. Applications of 3D city models: State of the art review. **ISPRS International Journal of Geo-Information**, v. 4, n. 4, p. 2842-2889, 2015.

BILTON, Amy M.; KELLEY, Leah C.; DUBOWSKY, Steven. Photovoltaic reverse osmosis—Feasibility and a pathway to develop technology. **Desalination and Water Treatment**, v. 31, n. 1-3, p. 24-34, 2011.

BLECHINGER, P.; CADER, C.; BERTHEAU, P.; HUYSKENS, H.; SEGUIN, R.; BREYER, C. Global analysis of the techno-economic potential of renewable energy hybrid systems on small islands. **Energy Policy**, v. 98, p. 674-687, 2016.

BÓDIS, K.; KOUGIAS, I.; JÄGER-WALDAU, A.; TAYLOR, N.; SZABÓ, S. A high-resolution geospatial assessment of the rooftop solar photovoltaic potential in the European Union. **Renewable and Sustainable Energy Reviews**, v. 114, p. 109309, 2019.

BOON, M. A.; DRIJFHOUT, A. P.; TESFAMICHAEL, S. Comparison of a fixed-wing and multi-rotor UAV for environmental mapping applications: a case study. **The International Archives of Photogrammetry, Remote Sensing and Spatial Information Sciences**, v. 42, p. 47, 2017.

BRASIL, 1942. **Decree-Law No. 4.102/1942**. Creates a Federal Territory of Fernando de Noronha. Federal Official Gazette - Section 1 - 2/11/1942. Available on: <https://www2.camara.leg.br/legin/fed/declei/1940-1949/decreto-lei-4102-9-fevereiro-1942-414714-publicacaooriginal-1-pe.html>. Accessed in April 2020.

BRASIL, 1987. **Decree-Law No. 94.780/1987**. Disposes on the basic structure of the Administration of the Federal Territory of Fernando de Noronha. Federal Official Gazette - Section 1 - 17/08/1987. Available on: <https://www.planalto.gov.br/ccivil_03/decreto/1980-1989/1985-1987/d94780.htm>. Accessed in April 2020.

BRASIL,1988a. **Decree-Law No. 95.922/1988**. Disposes about the zoning for the ecological defense of the Federal Territory of Fernando de Noronha. Federal Official Gazette - Section 1 - 15/04/1988. Available on: <https://www.planalto.gov.br/ccivil_03/decreto/1980-1989/d95922.htm>. Accessed in April 2020.

BRASIL, 1988b. **Constitution of the Federative Republic of Brazil of 1988**. Available on: <https://www2.senado.leg.br/bdsf/bitstream/handle/id/518231/CF88_Livro_EC91_2016.pdf>. Accessed in April 2020.

BRASIL, 2000. **Decree-Law No. 9.985/2000**. Institutes the National System of Nature Conservation Units. Federal Official Gazette - Section 1 - 19/07/2000. Available on: <https://www2.camara.leg.br/legin/indef/lei/2000/lei-9985-18-julho-2000-359708-norma-pl.html>. Accessed in April 2020.

BREWER, J.; AMES, D. P.; SOLAN, D.; LEE, R.; CARLISLE, J. Using GIS analytics and social preference data to evaluate utility-scale solar power site suitability. **Renewable energy**, v. 81, p. 825-836, 2015.

BYRNE, J.; TAMINIAU, J.; KURDGELASHVILI, L.; KIM, K. A review of the solar city concept and methods to assess rooftop solar electric potential, with an illustrative application to the city of Seoul. **Renewable and Sustainable Energy Reviews**, v. 41, p. 830-844, 2015.

CALVILLO, Christian F.; SÁNCHEZ-MIRALLES, Alvaro; VILLAR, Jose. Energy management and planning in smart cities. **Renewable and Sustainable Energy Reviews**, v. 55, p. 273-287, 2016.

CAMARGO, L. R.; ZINK, R.; DORNER, W.; STOEGLEHNER, G. Spatio-temporal modeling of roof-top photovoltaic panels for improved technical potential assessment and electricity peak load offsetting at the municipal scale. **Computers, Environment and Urban Systems**, v. 52, p. 58-69, 2015.

CAMERO, Andrés; ALBA, Enrique. Smart City and information technology: A review. **cities**, v. 93, p. 84-94, 2019.

CARAGLIU, Andrea; DEL BO, Chiara; NIJKAMP, Peter. Smart cities in Europe. **Journal of urban technology**, v. 18, n. 2, p. 65-82, 2011.

CARRIVICK, Jonathan L.; SMITH, Mark W.; QUINCEY, Duncan J. **Structure from Motion in the Geosciences**. John Wiley & Sons, 2016.

CASELLA, E.; COLLIN, A.; HARRIS, D.; FERSE, S.; BEJARANO, S.; PARRAVICINI, V.; HENCH, J.; ROVERE, A. L.Mapping coral reefs using consumer-grade drones and structure from motion photogrammetry techniques. **Coral Reefs**, v. 36, n. 1, p. 269-275, 2017.

CASTELLANOS, Sergio; SUNTER, Deborah A.; KAMMEN, Daniel M. Rooftop solar photovoltaic potential in cities: how scalable are assessment approaches? **Environmental Research Letters**, v. 12, n. 12, p. 125005, 2017.

CASTRO, José Ariel. CARTA DE CAMINHA, EXPEDIÇÃO DE CABRAL. **Revista da Escola Superior de Guerra**, n. 40, p. 64-91, 2001. Available on <https://www.esg.br/publi/arquivos-revista/revista_40.pdf/@@download/file/revista_40.pdf> Accessed in April 2020.

CELPE - Pernambuco Energy Company. Fernando de Noronha: Ilha de Inovação. Presentation in: **National Circuit of the Electric Sector (CINASE) 36th Edition Nordeste 2019**. 2019. 33 slides. Available on: <https://www.cinase.com.br/wp-content/uploads/2019/10/Caso-Fernando-de-Noronha_CELPE_compressed-2.pdf>. Accessed in April 2020.

CHIABRANDO, F.; DANNA, C.; LINGUA, A.; NOARDO, F.; OSELLO, A. 3D roof model generation and analysis supporting solar system positioning. **GEOMATICA**, v. 71, n. 3, p. 137-153, 2017.

CHOI, Yosoon; SUH, Jangwon; KIM, Sung-Min. GIS-based solar irradiance mapping, site evaluation, and potential assessment: A review. **Applied Sciences**, v. 9, n. 9, p. 1960, 2019.

CLAUDINO-SALES, Vanda. **Coastal World Heritage Sites**. Coastal Research Library. Vol. 28. Springer, 2018. DOI: 10.1007/978-94-024-1528-5.

COLOMINA, Ismael; MOLINA, Pere. Unmanned aerial systems for photogrammetry and remote sensing: A review. **ISPRS Journal of photogrammetry and remote sensing**, v. 92, p. 79-97, 2014.

COPPER, J. K. and BRUCE, A.G. Comparison of Annual Global Horizontal Irradiance Maps for Australia. **Asia Pacific Solar Research Conference**, Sydney, December 4-6 2018.

Creutzig, F.; Agoston, P.; Goldschmidt, J.; Luderer, G.; Nemet, G.; Pietzcker, R. C. The underestimated potential of solar energy to mitigate climate change. **Nature Energy**, v. 2, n. 9, p. 17140, 2017.

CROMMELINCK, S.; BENNETT, R.; GERKE, M.; NEX, F.; YANG, M. Y.; VOSSELMAN, G. Review of automatic feature extraction from high-resolution optical sensor data for UAV-based cadastral mapping. **Remote Sensing**, v. 8, n. 8, p. 689, 2016.

CURTO, D.; FRANZITTA, V.; VIOLA, A.; CIRRINCIONE, M.; MOHAMMADI, A.; KUMAR, A. A renewable energy mix to supply small islands. A comparative study applied to Balearic Islands and Fiji. **Journal of Cleaner Production**, v. 241, p. 118356, 2019.

CURTO, D.; FAVUZZA, S.; FRANZITTA, V.; MUSCA, R.; NAVIA, M.; ZIZZO, G. Evaluation of the optimal renewable electricity mix for Lampedusa island: The adoption of a technical and economical methodology. **Journal of Cleaner Production**, p. 121404, 2020.

DE ANDRADE, J.; RODRIGUES, B.; DOS SANTOS, I.; HADDAD, J.; TIAGO FILHO, G. L. Constitutional aspects of distributed generation policies for promoting Brazilian economic development. **Energy Policy**, v. 143, p. 111555, 2020.

DE GROOT, Maarten; KOGOJ, Meta. Temperature, leaf cover density and solar irradiance influence the abundance of an oligophagous insect herbivore at the southern edge of its range. **Journal of insect conservation**, v. 19, n. 5, p. 891-899, 2015.

DESTHIEUX, G.; CARNEIRO, C.; CAMPONOVO, R.; INEICHEN, P.; MORELLO, E.; BOULMIER, A.; ELLERT, C. Solar Energy Potential Assessment on Rooftops and Facades in Large Built Environments Based on LiDAR Data, Image Processing, and Cloud Computing. Methodological Background, Application, and Validation in Geneva (Solar Cadaster). **Frontiers in Built Environment**, v. 4, p. 14, 2018.

DI SILVESTRE, M. L.; FAVUZZA, S.; SANSEVERINO, E. R.; ZIZZO, G. How Decarbonization, Digitalization and Decentralization are changing key power infrastructures. **Renewable and Sustainable Energy Reviews**, v. 93, p. 483-498, 2018.

DJI - Dà-Jiāng Innovations Science and Technology. **Phantom 4 Pro**. 2020. Available on: <https://www.dji.com/br/phantom-4-pro>. Accessed in April 2020.

DONDARIYA, C.; PORWAL, D.; AWASTHI, A.; SHUKLA, A. K.; SUDHAKAR, K.; SR, M. M.; BHIMTE, A. Performance simulation of grid-connected rooftop solar PV system for small households: A case study of Ujjain, India. **Energy reports**, v. 4, p. 546-553, 2018.

DOORGA, Jay Rovisham Singh; RUGHOOPUTH, Soonil DDV; BOOJHAWON, Ravindra. High resolution spatio-temporal modelling of solar photovoltaic potential for tropical islands: Case of Mauritius. **Energy**, v. 169, p. 972-987, 2019.

DroneDeploy. **Mapping varied elevations, tall buildings or trees**. 2019. Available on: <https://support.dronedeploy.com/docs/mapping-varied-elevations-tall-buildings-or-trees>. Accessed in April 2020.

DUBAYAH, Ralph; RICH, Paul M. Topographic solar irradiance models for GIS. **International journal of geographical information systems**, v. 9, n. 4, p. 405-419, 1995.

DUPONT, Elise; KOPPELAAR, Rembrandt; JEANMART, Hervé. Global available solar energy under physical and energy return on investment constraints. **Applied Energy**, v. 257, p. 113968, 2020.

EDENHOFER, O.; PICHS-MADRUGA, R.; SOKONA, Y.; SEYBOTH, K.; KADNER, S.; ZWICKEL, T.; MATSCHOSS, P. Renewable energy sources and climate change mitigation: Special report of the intergovernmental panel on climate change. **Cambridge University Press**, 2011.

EICKER, U.; NOUVEL, R.; DUMINIL, E.; COORS, V. Assessing passive and active solar energy resources in cities using 3D city models. **Energy Procedia**, v. 57, n. 896, p. e905, 2014.

EKASO, Desta; NEX, Francesco; KERLE, Norman. Accuracy assessment of real-time kinematics (RTK) measurements on unmanned aerial vehicles (UAV) for direct geo-referencing. **Geo-spatial information science**, p. 1-17, 2020.

ERAS-ALMEIDA, A. A.; EGIDO-AGUILERA, M. A.; BLECHINGER, P.; BERENDES, S.; CAAMAÑO, E.; GARCÍA-ALCALDE, E. Decarbonizing the Galapagos Islands: Techno-Economic Perspectives for the Hybrid Renewable Mini-Grid Baltra–Santa Cruz. **Sustainability**, v. 12, n. 6, p. 2282, 2020.

ERDÉLYI, R.; WANG, Y.; GUO, W.; HANNA, E.; COLANTUONO, G. Three-dimensional SOlar Irradiance Model (SORAM) and its application to 3-D urban planning. **Solar Energy**, v. 101, p. 63-73, 2014.

ESCLAPÉS, J., FERREIRO, I., PIERA, J., TELLER, J. A method to evaluate the adaptability of photovoltaic energy on urban façades. **Solar Energy**, v. 105, p. 414-427, 2014.

ESRI - Environmental Systems Research Institute. **ArcGIS Pro Tool Reference: An overview of the Solar Radiation toolset**. 2020. Available on: <https://pro.arcgis.com/en/pro-app/tool-reference/spatial-analyst/an-overview-of-the-solar-irradiance-tools.htm> Accessed in April 2020.

ETHERDEN, Nicholas; BOLLEN, Math HJ. Overload and overvoltage in low-voltage and medium-voltage networks due to renewable energy–some illustrative case studies. **Electric Power Systems Research**, v. 114, p. 39-48, 2014.

FALKLEV, Erlend Homme. **Mapping of solar energy potential on Tromsøya using solar analyst in ArcGIS**. 2017. Master Dissertation of The Arctic University of Norway.

FATH, K.; STENGEL, J.; SPRENGER, W.; WILSON, H. R.; SCHULTMANN, F.; KUHN, T. A method for predicting the economic potential of (building-integrated) photovoltaics in urban areas based on hourly Radiance simulations. **Solar energy**, v. 116, p. 357-370, 2015.

FAZELI, H.; SAMADZADEGAN, F.; DADRASJAVAN, F. Evaluating the potential of RTK-UAV for automatic point cloud generation in 3D rapid mapping. **The International Archives of Photogrammetry, Remote Sensing and Spatial Information Sciences**, v. 41, p. 221, 2016.

FETAI, B.; OŠTIR, K.; KOSMATIN FRAS, M.; LISEC, A. Extraction of Visible Boundaries for Cadastral Mapping Based on UAV Imagery. **Remote Sensing**, v. 11, n. 13, p. 1510, 2019.

FONSECA NETO, F.; GRIPP JUNIOR, J.; BOTELHO, M.; DOS SANTOS, A.; NASCIMENTO, L.; BRAGA FONSECA, A. Assessment of positional quality in spatial data generated by VANT using point and linear feature for cadastre applications. **Boletim de Ciências Geodésicas**, v. 23, n. 1, p. 134-149, 2017.

FONSTAD, M.; DIETRICH, J.; COURVILLE, B. C.; JENSEN, J.; CARBONNEAU, P. Topographic structure from motion: a new development in photogrammetric measurement. **Earth surface processes and Landforms**, v. 38, n. 4, p. 421-430, 2013.

FORLANI, G.; DALL'ASTA, E.; DIOTRI, F.; CELLA, U.; RONCELLA, R.; SANTISE, M. Quality assessment of DSMs produced from UAV flights georeferenced with on-board RTK positioning. **Remote Sensing**, v. 10, n. 2, p. 311, 2018.

FREITAS, S.; CATITA, C.; REDWEIK, P.; BRITO, M. Modelling solar potential in the urban environment: State-of-the-art review. **Renewable and Sustainable Energy Reviews**, v. 41, p. 915-931, 2015.

FU, Pinde; RICH, Paul M. Design and implementation of the Solar Analyst: an ArcView extension for modeling solar irradiance at landscape scales. In: **Proceedings of the nineteenth annual ESRI user conference**. USA: San Diego, 1999. p. 1-31.

FURUKAWA, Y.; CURLESS, B.; SEITZ, S.; SZELISKI, R. Towards internet-scale multi-view stereo. In: **2010 IEEE computer society conference on computer vision and pattern recognition**. IEEE, 2010. p. 1434-1441.

FURUKAWA, Yasutaka; PONCE, Jean. Accurate, dense, and robust multiview stereopsis. **IEEE transactions on pattern analysis and machine intelligence**, v. 32, n. 8, p. 1362-1376, 2009.

GAGO, J.; DOUTHE, C.; COOPMAN, R. , GALLEGO, P.; RIBAS-CARBO, M.; FLEXAS, J.; MEDRANO, H. UAVs challenge to assess water stress for sustainable agriculture. **Agricultural water management**, v. 153, p. 9-19, 2015.

GALLARDO-SAAVEDRA, Sara; HERNÁNDEZ-CALLEJO, Luis; DUQUE-PEREZ, Oscar. Technological review of the instrumentation used in aerial thermographic inspection of photovoltaic plants. **Renewable and Sustainable Energy Reviews**, v. 93, p. 566-579, 2018.

GIENKO, Gennady A.; TERRY, James P. Three-dimensional modeling of coastal boulders using multi-view image measurements. **Earth surface processes and Landforms**, v. 39, n. 7, p. 853-864, 2014.

GWA - Global Wind Atlas – **GWA App. 2020.** Available on <https://globalwindatlas.info/>. Accessed in April 2020.

GOLDTHAU, Andreas. Rethinking the governance of energy infrastructure: Scale, decentralization and polycentrism. **Energy Research & Social Science**, v. 1, p. 134-140, 2014.

GONÇALVES, J. A.; HENRIQUES, R. UAV photogrammetry for topographic monitoring of coastal areas. **ISPRS Journal of Photogrammetry and Remote Sensing**, v. 104, p. 101-111, 2015.

GREEN, Martin A.; HISHIKAWA, Y.; WARTA, W.; DUNLOP, E. Solar cell efficiency tables (Version 45). **Progress in photovoltaics: research and applications**, v. 23, n. 1, p. 1-9, 2015.

GREEN, Martin A. Photovoltaics: technology overview. **Energy policy**, v. 28, n. 14, p. 989-998, 2000.

GSA - Global Solar Atlas. **GSA App.** 2020. Available on <https://globalsolaratlas.info/>. Accessed in April 2020.

GUNGOR, V.; SAHIN, D.; KOCAK, T.; ERGUT, S.; BUCCELLA, C.; CECATI, C.; HANCKE, G. P. Smart grid and smart homes: Key players and pilot projects. **IEEE Industrial Electronics Magazine**, v. 6, n. 4, p. 18-34, 2012.

HAAS, F.; HILGER, L.; NEUGIRG, F.; UMSTÄDTER, K.; BREITUNG, C.; FISCHER, P.; BECHT, M. Quantification and analysis of geomorphic processes on a recultivated iron ore mine on the Italian island of Elba using long-term ground-based lidar and photogrammetric SfM data by a UAV. **Natural Hazards and Earth System Sciences**, v. 16, n. 5, p. 1269-1288, 2016.

HASHEMI-BENI, L.; JONES, J.; THOMPSON, G.; JOHNSON, C.; GEBREHIWOT, A. Challenges and opportunities for UAV-based digital elevation model generation for flood-risk management: A case of princeville, north carolina. **Sensors**, v. 18, n. 11, p. 3843, 2018.

HIREMATH, R. B.; SHIKHA, S.; RAVINDRANATH, N. H. Decentralized energy planning; modeling and application—a review. **Renewable and Sustainable Energy Reviews**, v. 11, n. 5, p. 729-752, 2007.

HOFIERKA, Jaroslav; SURI, Marcel. The solar irradiance model for Open source GIS: implementation and applications. In: **Proceedings of the Open source GIS-GRASS users conference**. 2002. p. 1-19.

HOFIERKA, Jaroslav; KAŇUK, Ján; GALLAY, Michal. The spatial distribution of photovoltaic power plants in relation to solar resource potential: the case of the Czech Republic and Slovakia. **Moravian Geographical Reports**, v. 22, n. 2, p. 26-33, 2014.

HOFIERKA, Jaroslav; ZLOCHA, Marian. A new 3-D solar irradiance model for 3-D city models. **Transactions in GIS**, v. 16, n. 5, p. 681-690, 2012.

HONG, T.; LEE, M.; KOO, C.; JEONG, K.; KIM, J. Development of a method for estimating the rooftop solar photovoltaic (PV) potential by analyzing the available rooftop area using Hillshade analysis. **Applied Energy**, v. 194, p. 320-332, 2017.

HONKAVAARA, E.; SAARI, H.; KAIVOSOJA, J.; PÖLÖNEN, I.; HAKALA, T.; LITKEY, P.; PESONEN, L. Processing and assessment of spectrometric, stereoscopic imagery collected using a lightweight UAV spectral camera for precision agriculture. **Remote Sensing**, v. 5, n. 10, p. 5006-5039, 2013.

HUANG, S.; FU, P. 2009. **Modeling Small Areas Is a Big Challenge**. ESRI, ArcUser Online, Spring edition, 28–31. Available on: <https://www.esri.com/news/arcuser/0309/files/solar.pdf>. Accessed in April 2020.

HUANG, S.; RICH, P. M.; CRABTREE, R. L.; POTTER, C. S.; FU, P. Modeling monthly near-surface air temperature from solar irradiance and lapse rate: Application over complex terrain in Yellowstone National Park. **Physical Geography**, v. 29, n. 2, p. 158-178, 2008.

IBGE - Brazilian Institute of Geography and Statistics. **IBGE | Cidades@ | Pernambuco | Fernando de Noronha.** 2020, a. Available on: <https://cidades.ibge.gov.br/brasil/pe/fernando-de-noronha/panorama>. Accessed in February 2020.

IBGE - Brazilian Institute of Geography and Statistics. **Geodetic Database APPBDG.** 2020, b. Available on: <http://www.bdg.ibge.gov.br/appbdg/>. Accessed in April 2020.

IGLHAUT, J.; CABO, C.; PULITI, S.; PIERMATTEI, L.; O'CONNOR, J.; ROSETTE, J. Structure from motion photogrammetry in forestry: A review. **Current Forestry Reports**, v. 5, n. 3, p. 155-168, 2019.

IRENA – International Renewable Energy Agency. **Renewable Energy and Jobs: Annual Review 2019**. ISBN: 978-92-9260-134-8. 2019. Available on <https://www.irena.org/publications/2019/Jun/Renewable-Energy-and-Jobs-Annual-Review-2019>. Accessed in July 2020.

IRENA – International Renewable Energy Agency. **Renewable power generation costs in 2019.** ISBN: 978-92-9260-244-4. 2020. Available on <https://www.irena.org/-/media/Files/IRENA/Agency/Publication/2020/Jun/IRENA_Power_Generation_Costs_2019.pdf>. Accessed in January 2021.

JAMES, M. R.; ROBSON, S.; D'OLEIRE-OLTMANNS, S.; NIETHAMMER, U. Optimizing UAV topographic surveys processed with structure-from-motion: Ground control quality, quantity and bundle adjustment. **Geomorphology**, v. 280, p. 51-66, 2017.

JANKE, Jason R. Multicriteria GIS modeling of wind and solar plants in Colorado. **Renewable Energy**, v. 35, n. 10, p. 2228-2234, 2010.

JANTZEN, Jan; KRISTENSEN, Michael; CHRISTENSEN, Toke Haunstrup. Sociotechnical transition to smart energy: The case of Samso 1997–2030. **Energy**, v. 162, p. 20-34, 2018.

JEZIORSKA, Justyna. UAS for Wetland Mapping and Hydrological Modeling. **Remote Sensing**, v. 11, n. 17, p. 1997, 2019.

JIMÉNEZ-LÓPEZ, Jesús; MULERO-PÁZMÁNY, Margarita. Drones for conservation in protected areas: present and future. **Drones**, v. 3, n. 1, p. 10, 2019.

KABALCI, Yasin. A survey on smart metering and smart grid communication. **Renewable and Sustainable Energy Reviews**, v. 57, p. 302-318, 2016.

KABIR, E., KUMAR, P., KUMAR, S., ADELODUN, A.; KIM, K. Solar energy: Potential and future prospects. **Renewable and Sustainable Energy Reviews**, v. 82, p. 894-900, 2018.

KAUNDINYA, Deepak Paramashivan; BALACHANDRA, P.; RAVINDRANATH, Nijavalli H. Grid-connected versus stand-alone energy systems for decentralized power—A review of literature. **Renewable and Sustainable Energy Reviews**, v. 13, n. 8, p. 2041-2050, 2009.

KODYSH, J.; OMITAOMU, O.; BHADURI, B.; NEISH, B. Methodology for estimating solar potential on multiple building rooftops for photovoltaic systems. **Sustainable Cities and Society**, v. 8, p. 31-41, 2013.

KOEVA, M.; MUNEZA, M.; GEVAERT, C.; GERKE, M.; NEX, F. Using UAVs for map creation and updating. A case study in Rwanda. **Survey review**, v. 50, n. 361, p. 312-325, 2018.

KOH, Lian Pin; WICH, Serge A. Dawn of drone ecology: low-cost autonomous aerial vehicles for conservation. **Tropical Conservation Science**, v. 5, n. 2, p. 121-132, 2012.

KRÜGER, A.; KOLBE, T. H. Building analysis for urban energy planning using key indicators on virtual 3D city models—the energy atlas of Berlin. **International Archives of the Photogrammetry, Remote Sensing and Spatial Information Sciences**, v. 39, n. B2, p. 145-150, 2012.

KUANG, Y.; ZHANG, Y.; ZHOU, B.; LI, C.; CAO, Y.; LI, L.; ZENG, L. A review of renewable energy utilization in islands. **Renewable and Sustainable Energy Review**s, v. 59, p. 504-513, 2016.

LEE, Nathan; ROBERTS, Billy J. **Technical Potential Assessment for the Renewable Energy Zone (REZ) Process: A GIS-based Approach**. National Renewable Energy Lab.(NREL), Golden, CO (United States), 2018.

LEITÃO, J.; MOY DE VITRY, M.; SCHEIDEGGER, A.; RIECKERMANN, J. Assessing the quality of digital elevation models obtained from mini unmanned aerial vehicles for overland flow modelling in urban areas. **Hydrology and Earth System Sciences**, v. 20, n. 4, p. 1637, 2016.

LISEIN, J.; PIERROT-DESEILLIGNY, M.; BONNET, S.; LEJEUNE, P. A photogrammetric workflow for the creation of a forest canopy height model from small unmanned aerial system imagery. **Forests**, v. 4, n. 4, p. 922-944, 2013.

LIU, J.; MEI, C.; WANG, H.; SHAO, W.; XIANG, C. Powering an island system by renewable energy—A feasibility analysis in the Maldives. **Applied Energy**, v. 227, p. 18-27, 2018.

LONGLEY, P.; GOODCHILD, M.; MAGUIRE, D.; RHIND, D. **Geographic information science and systems**. John Wiley & Sons, 2015.

LOPEZ, A.; ROBERTS, B.; HEIMILLER, D.; BLAIR, N.; PORRO, G. **US Renewable Energy Technical Potentials. A GIS-Based Analysis**. National Renewable Energy Lab.(NREL), Golden, CO (United States), 2012.

LOWE, David G. Distinctive image features from scale-invariant keypoints. **International journal of computer vision**, v. 60, n. 2, p. 91-110, 2004.

LUCIEER, Arko; JONG, Steven M. de; TURNER, Darren. Mapping landslide displacements using Structure from Motion (SfM) and image correlation of multi-temporal UAV photography. **Progress in Physical Geography**, v. 38, n. 1, p. 97-116, 2014.

LUKAČ, N., SEME, S., DEŽAN, K., ŽALIK, B., ŠTUMBERGER, G. Economic and environmental assessment of rooftops regarding suitability for photovoltaic systems installation based on remote sensing data. **Energy**, v. 107, p. 854-865, 2016.

LUQUE, Antonio; HEGEDUS, Steven (Ed.). **Handbook of photovoltaic science and engineering**. John Wiley & Sons, 2011.

MAES, Wouter H.; STEPPE, Kathy. Perspectives for remote sensing with unmanned aerial vehicles in precision agriculture. **Trends in plant science**, v. 24, n. 2, p. 152-164, 2019.

MAJUMDAR, Debaleena. **Planning for the Energy Transition: Solar Photovoltaics in Arizona**. 2018. Ph.D. Thesis. Arizona State University.

MANFREDA, S.; DVORAK, P.; MULLEROVA, J.; HERBAN, S.; VUONO, P.; JUSTEL, J.; PERKS, M. Assessing the Accuracy of Digital Surface Models Derived from Optical Imagery Acquired with Unmanned Aerial Systems. **Drones**, v. 3, n. 1, p. 15, 2019.

MAREŠOVÁ, Eva. **LIDAR based estimation of roof-top photovoltaic potential of Wageningen. Case of Wageningen Municipality**. Master of Science Thesis Report. Wageningen University and Research Centre, The Netherlands. 2014

MARGOLIS, R.; GAGNON, P.; MELIUS, J.; PHILLIPS, C.; ELMORE, R. Using GIS-based methods and lidar data to estimate rooftop solar technical potential in US cities. **Environmental Research Letters**, v. 12, n. 7, p. 074013, 2017.

MARTÍN, Ana M.; DOMÍNGUEZ, Javier; AMADOR, Julio. Applying LIDAR datasets and GIS based model to evaluate solar potential over roofs: a review. **AIMS Energy**, v. 3, n. 3, p. 326-343, 2015.

MAVROMATIDIS, Georgios; OREHOUNIG, Kristina; CARMELIET, Jan. Evaluation of photovoltaic integration potential in a village. **Solar Energy**, v. 121, p. 152-168, 2015.

MCKENNA, P.; ERSKINE, P. D.; LECHNER, A. M.; PHINN, S. Measuring fire severity using UAV imagery in semi-arid central Queensland, Australia. **International Journal of Remote Sensing**, v. 38, n. 14, p. 4244-4264, 2017.

MEHRJERDI, Hasan. Modeling and optimization of an island water-energy nexus powered by a hybrid solar-wind renewable system. **Energy**, p. 117217, 2020.

MELLO, Thayna Jeremias; OLIVEIRA, Alexandre Adalardo de. Making a bad situation worse: An invasive species altering the balance of interactions between local species. **PloS one**, v. 11, n. 3, p. e0152070, 2016.

MENTIS, D.; KARALIS, G.; ZERVOS, A.; HOWELLS, M.; TALIOTIS, C.; BAZILIAN, M.; ROGNER, H. Desalination using renewable energy sources on the arid islands of South Aegean Sea. **Energy**, v. 94, p. 262-272, 2016.

MEZEI, P.; JAKUŠ, R.; BLAŽENEC, M.; BELÁNOVÁ, S.; ŠMÍDT, J. The relationship between potential solar irradiance and spruce bark beetle catches in pheromone traps. **Annals of Forest Research**, v. 55, n. 2, p. 243-252, 2012.

MIRANDA, Raul; SZKLO, Alexandre; SCHAEFFER, Roberto. Technical-economic potential of PV systems on Brazilian rooftops. **Renewable Energy**, v. 75, p. 694-713, 2015.

MMA - Ministério do Meio Ambiente do Brasil (Ministry of the Environment). **SNUC – Sistema Nacional de Unidades de Conservação da Natureza (Nature Conservation Units National System):** Decree-Law nº 9.985/2000; Decree-Law nº 4.340/2002; Decree-Law nº 5.746/2006. Decree-Law nº 5.758/2006. p. 76, Brasília: MMA, 2011.

MOUDRÝ, Vítězslav; BEKOVÁ, Anna; LAGNER, Ondřej. Evaluation of a high resolution UAV imagery model for rooftop solar irradiance estimates. **Remote Sensing Letters**, v. 10, n. 11, p. 1077-1085, 2019.

MUMBONE, Mukendwa. **Innovations in Boundary Mapping: Namibia, Customary Land and UAV's**. University of Twente Faculty of Geo-Information and Earth Observation (ITC), 2015.

NASCIMENTO, Grazielle Rodrigues do. Fernando de Noronha e os Ventos da Guerra Fria: a relação entre Brasil e Estados Unidos nos anos de JK. 2009. **Master Dissertation in Universidade Federal de Pernambuco**.

NELSON, Jake R.; GRUBESIC, Tony H. The use of LiDAR versus unmanned aerial systems (UAS) to assess rooftop solar energy potential. **Sustainable Cities and Society**, v. 61, p. 102353, 2020.

NERO, M.; SALIM, D.; MELLO, C.; AMARANTE, R.; FONSECA, B.; TEMBA, P. Case study of a model of local solar radiation potential and discussion on the associated sustainable applications and potentials. **Sustainability in Debate/Sustentabilidade em Debate**, v. 11, n. 2, 2020.

NEX, Francesco; REMONDINO, Fabio. UAV for 3D mapping applications: a review. **Applied geomatics**, v. 6, n. 1, p. 1-15, 2014.

NGUYEN, Ha T.; PEARCE, Joshua M. Incorporating shading losses in solar photovoltaic potential assessment at the municipal scale. **Solar Energy**, v. 86, n. 5, p. 1245-1260, 2012.

NIELSEN, Søren Nors; JØRGENSEN, Sven Erik. Sustainability analysis of a society based on exergy studies–a case study of the island of Samsø (Denmark). **Journal of Cleaner Production**, v. 96, p. 12-29, 2015.

NIETHAMMER, U.; JAMES, M. R.; ROTHMUND, S.; TRAVELLETTI, J.; JOSWIG, M. UAV-based remote sensing of the Super-Sauze landslide: Evaluation and results. **Engineering Geology**, v. 128, p. 2-11, 2012.

NUNES, Pedro; FIGUEIREDO, Raquel; BRITO, Miguel C. The use of parking lots to solar-charge electric vehicles. **Renewable and Sustainable Energy Reviews**, v. 66, p. 679-693, 2016.

PADRÓ, J.; MUÑOZ, F.; PLANAS, J.; PONS, X. Comparison of four UAV georeferencing methods for environmental monitoring purposes focusing on the combined use with airborne and satellite remote sensing platforms. **International Journal of Applied Earth Observation and Geoinformation**, v. 75, p. 130-140, 2019.

PAJARES, Gonzalo. Overview and current status of remote sensing applications based on unmanned aerial vehicles (UAVs). **Photogrammetric Engineering & Remote Sensing**, v. 81, n. 4, p. 281-330, 2015.

PALMER, D.; KOUBLI, E.; COLE, I.; BETTS, T.; GOTTSCHALG, R. Satellite or ground-based measurements for production of site specific hourly irradiance data: Which is most accurate and where?. **Solar Energy**, v. 165, p. 240-255, 2018.

PAPAKONSTANTINOU, Apostolos; TOPOUZELIS, Konstantinos; PAVLOGEORGATOS, Gerasimos. Coastline zones identification and 3D coastal mapping using UAV spatial data. **ISPRS International Journal of Geo-Information**, v. 5, n. 6, p. 75, 2016.

PELLETIER, Jon D.; SWETNAM, Tyson L. Asymmetry of weathering-limited hillslopes: the importance of diurnal covariation in solar insolation and temperature. **Earth Surface Processes and Landforms**, v. 42, n. 9, p. 1408-1418, 2017.

PEREZ, R.; SEALS, R.; INEICHEN, P.; STEWART, R.; MENICUCCI, D. A new simplified version of the Perez diffuse irradiance model for tilted surfaces. **Solar energy**, v. 39, n. 3, p. 221-231, 1987.

PERNAMBUCO STATE DATABASE. **Infraestrutura | Energia | Consumo de energia elétrica | Fernando de Noronha**. Available on <http://www.bde.pe.gov.br/>. Accessed in April 2020.

PERONATO, Giuseppe. Urban planning support based on the photovoltaic potential of buildings: a multi-scenario ranking system. **PhD Thesis in L'Ecole polytechnique fédérale de Lausanne**, 2019.

PIELECH, Remigiusz; ANIOŁ-KWIATKOWSKA, Jadwiga; SZCZĘŚNIAK, Ewa. Landscape-scale factors driving plant species composition in mountain streamside and spring riparian forests. **Forest Ecology and Management**, v. 347, p. 217-227, 2015.

PS - Project Sunroof. **Google Project Sunroof.** 2020. Available on <https://www.google.com/get/sunroof>. Accessed in April, 2020.

RAMADHANI, Sheilla Ayu; BENNETT, R. M.; NEX, F. C. Exploring UAV in Indonesian cadastral boundary data acquisition. **Earth science informatics**, v. 11, n. 1, p. 129-146, 2018.

REDISKE, G.; SILUK, J. C. M.; MICHELS, L.; RIGO, P. D.; ROSA, C. B.; CUGLER, G. Multi-criteria decision-making model for assessment of large photovoltaic plants in Brazil. **Energy**, v. 197, p. 117-167, 2020.

REKA, S. Sofana; DRAGICEVIC, Tomislav. Future effectual role of energy delivery: A comprehensive review of Internet of Things and smart grid. **Renewable and Sustainable Energy Reviews**, v. 91, p. 90-108, 2018.

REMONDINO, F.; NOCERINO, E.; TOSCHI, I.; MENNA, F. A CRITICAL REVIEW OF AUTOMATED PHOTOGRAMMETRIC PROCESSING OF LARGE DATASETS. **International Archives of the Photogrammetry, Remote Sensing & Spatial Information Sciences**, v. 42, 2017.

REN21. **Renewables 2019 Global Status Report**; REN21 Secretariat: Paris, France, 2019; ISBN 978-3-9818911-7-1. Available on: <http://www.ren21.net/gsr-2019/> Accessed in February 2020.

RIBEIRO, F.; LAURIA, D.; DO RIO, M.; DA CUNHA, F.; DE OLIVEIRA SOUSA, W.; LIMA, E.; FRANZEN, M. Mapping soil radioactivity in the Fernando de Noronha archipelago, Brazil. **Journal of Radioanalytical and Nuclear Chemistry**, v. 311, n. 1, p. 577-587, 2017.

RUIZ-ARIAS, J. A.; TOVAR-PESCADOR, J.; POZO-VÁZQUEZ, D.; ALSAMAMRA, H. A comparative analysis of DEM-based models to estimate the solar irradiance in mountainous terrain. **International Journal of Geographical Information Science**, v. 23, n. 8, p. 1049-1076, 2009.

SALES, Vanda. **Coastal World Heritage Sites**. Coastal Research Library. v. 28. Springer, 2018.

SALIM, Mariam G. Selection of groundwater sites in Egypt, using geographic information systems, for desalination by solar energy in order to reduce greenhouse gases. **Journal of Advanced Research**, v. 3, n. 1, p. 11-19, 2012.

SAMPAIO, Priscila Gonçalves Vasconcelos; GONZÁLEZ, Mario Orestes Aguirre. Photovoltaic solar energy: Conceptual framework. **Renewable and Sustainable Energy Reviews**, v. 74, p. 590-601, 2017.

SÁNCHEZ-LOZANO, J. M.; TERUEL-SOLANO, J.; SOTO-ELVIRA, P. L.; GARCÍA-CASCALES, M. S. Geographical Information Systems (GIS) and Multi-Criteria Decision Making (MCDM) methods for the evaluation of solar plants locations: Case study in south-eastern Spain. **Renewable and Sustainable Energy Reviews**, v. 24, p. 544-556, 2013.

SANKEY, T.; DONAGER, J.; MCVAY, J.; SANKEY, J. B. UAV lidar and hyperspectral fusion for forest monitoring in the southwestern USA. **Remote Sensing of Environment**, v. 195, p. 30-43, 2017.

SANZ-ABLANEDO, E.; CHANDLER, J. H.; RODRÍGUEZ-PÉREZ, J. R.; ORDÓÑEZ, C. Accuracy of unmanned aerial vehicle (UAV) and SfM photogrammetry survey as a function of the number and location of ground control points used. **Remote Sensing**, v. 10, n. 10, p. 1606, 2018.

SCHALLENBERG-RODRÍGUEZ, Julieta. Photovoltaic techno-economical potential on roofs in regions and islands: the case of the Canary Islands. Methodological review and methodology proposal. **Renewable and Sustainable Energy Reviews**, v. 20, p. 219-239, 2013.

SCHENK, Toni. Introduction to photogrammetry. **The Ohio State University, Columbus**, v. 106, 2005.

SCHUFFERT, S.; VOEGTLE, T.; TATE, N.; RAMIREZ, A. Quality assessment of roof planes extracted from height data for solar energy systems by the EAGLE platform. **Remote Sensing**, v. 7, n. 12, p. 17016-17034, 2015.

SCOGNAMIGLIO, A.; GARDE, F.; MONNIER, A.; SCOTTO, E. Photovoltaic greenhouses: a feasible solution for islands? Design operation monitoring and lessons learned from a real case study. **In Conference: The 6th World Conference on Photovoltaic Energy Conversion**. p. 1169-1070. 2014.

SEKIYAMA, Takashi; NAGASHIMA, Akira. Solar Sharing for Both Food and Clean Energy Production: Performance of Agrivoltaic Systems for Corn, A Typical Shade-Intolerant Crop. **Environments**, v. 6, n. 6, p. 65, 2019.

SELOSSE, S.; GARABEDIAN, S.; RICCI, O.; MAÏZI, N. The renewable energy revolution of reunion island. **Renewable and Sustainable Energy Reviews**, v. 89, p. 99-105, 2018.

SHAAD, K.; NINSALAM, Y.; PADAWANGI, R.; BURLANDO, P. Towards high resolution and cost-effective terrain mapping for urban hydrodynamic modelling in densely settled river-corridors. **Sustainable Cities and Society**, v. 20, p. 168-179, 2016.

SHUKLA, Akash Kumar; SUDHAKAR, K.; BAREDAR, Prashant. Simulation and performance analysis of 110 kWp grid-connected photovoltaic system for residential building in India: A comparative analysis of various PV technology. **Energy Reports**, v. 2, p. 82-88, 2016.

SILVA, Marieta Borges Lins; Fernando de Noronha: cinco séculos de história. **Recife: Editora Universitária da UFPE**, 2013.

SINGH, Kunwar K.; FRAZIER, Amy E. A meta-analysis and review of unmanned aircraft system (UAS) imagery for terrestrial applications. **International Journal of Remote Sensing**, v. 39, n. 15-16, p. 5078-5098, 2018.

SMETS, A.; JÄGER, K.; ISABELLA, O.; SWAAIJ, R. A.; ZEMAN, M. **physics and engineering of photovoltaic conversion, technologies and systems**. UIT Cambridge Ltd, 2016. Electronic Book. ISBN: 9781906860752

SPERLING, Karl. How does a pioneer community energy project succeed in practice? The case of the Samsø Renewable Energy Island. **Renewable and Sustainable Energy Reviews**, v. 71, p. 884-897, 2017.

STURDIVANT, E. J.; LENTZ, E. E.; THIELER, E. R.; FARRIS, A. S.; WEBER, K. M.; REMSEN, D. P.; HENDERSON, R. E. UAS-SfM for coastal research: Geomorphic feature extraction and land cover classification from high-resolution elevation and optical imagery. **Remote Sensing**, v. 9, n. 10, p. 1020, 2017.

SUH, Jangwon; BROWNSON, Jeffrey. Solar farm suitability using geographic information system fuzzy sets and analytic hierarchy processes: Case study of Ulleung Island, Korea. **Energies**, v. 9, n. 8, p. 648, 2016.

SUNTER, Deborah A.; CASTELLANOS, Sergio; KAMMEN, Daniel M. Disparities in rooftop photovoltaics deployment in the United States by race and ethnicity. **Nature Sustainability**, v. 2, n. 1, p. 71-76, 2019.

ŠÚRI, Marcel; HOFIERKA, Jaroslav. A new GIS-based solar irradiance model and its application to photovoltaic assessments. **Transactions in GIS**, v. 8, n. 2, p. 175-190, 2004.

SWEENEY, C. 2016. **Theia vision library**. Available on: <http://www.theia-sfm.org/sfm.html>. Accessed in April 2020.

SZABÓ, S.; ENYEDI, P.; HORVÁTH, M.; KOVÁCS, Z.; BURAI, P.; CSOKNYAI, T.; SZABÓ, G. Automated registration of potential locations for solar energy production with Light Detection And Ranging (LiDAR) and small format photogrammetry. **Journal of Cleaner Production**, v. 112, p. 3820-3829, 2016.

TENEDÓRIO, J. A.; ESTANQUEIRO, R.; MATOS LIMA, A.; MARQUES, J. Remote sensing from unmanned aerial vehicles for 3D urban modelling: case study of Loulé, Portugal. In: **Back to the Sense of the City: International Monograph Book**. Centre de Política de Sòl i Valoracions, 2016. p. 1118-1128.

TOMAŠTÍK, J.; MOKROŠ, M.; SUROVÝ, P.; GRZNÁROVÁ, A.; MERGANIČ, J. UAV RTK/PPK Method—An Optimal Solution for Mapping Inaccessible Forested Areas?. **Remote sensing**, v. 11, n. 6, p. 721, 2019.

TSANAKAS, John A.; HA, Long D.; AL SHAKARCHI, F. Advanced inspection of photovoltaic installations by aerial triangulation and terrestrial georeferencing of thermal/visual imagery. **Renewable Energy**, v. 102, p. 224-233, 2017.

TURNER, Darren; LUCIEER, Arko; WATSON, Christopher. An automated technique for generating georectified mosaics from ultra-high resolution unmanned aerial vehicle (UAV) imagery, based on structure from motion (SfM) point clouds. **Remote sensing**, v. 4, n. 5, p. 1392-1410, 2012.

TURNER, Darren; LUCIEER, Arko; DE JONG, Steven M. Time series analysis of landslide dynamics using an unmanned aerial vehicle (UAV). **Remote Sensing**, v. 7, n. 2, p. 1736-1757, 2015.

TURNER, Ian L.; HARLEY, Mitchell D.; DRUMMOND, Christopher D. UAVs for coastal surveying. **Coastal Engineering**, v. 114, p. 19-24, 2016.

ULLMAN, Shimon. The interpretation of structure from motion. **Proceedings of the Royal Society of London. Series B. Biological Sciences**, v. 203, n. 1153, p. 405-426, 1979.

UNESCO - United Nations Education, Scientific and Cultural Organization. **Brazilian Atlantic Islands: Fernando de Noronha and Atol das Rocas Reserves.** Available on: <https://whc.unesco.org/en/list/1000>. Accessed in April 2020.

US EIA - United States Energy Information Administration. **Solar explained Photovoltaics and electricity.** Available on: <https://www.eia.gov/energyexplained/solar/photovoltaics-and-electricity.php>. Accessed in April 2020.

USGS - United States Geological Survey. **Agisoft PhotoScan Workflow**. USGS National UAS Project Office – March 2017. Accessed in April 2020. Available on: <https://uas.usgs.gov/nupo/pdf/USGSAgisoftPhotoScanWorkflow.pdf>. Accessed in April 2020.

VAN HOESEN, John; LETENDRE, Steven. Evaluating potential renewable energy resources in Poultney, Vermont: A GIS-based approach to supporting rural community energy planning. **Renewable energy**, v. 35, n. 9, p. 2114-2122, 2010.

VARDIMON, Ran. Assessment of the potential for distributed photovoltaic electricity production in Israel. **Renewable Energy**, v. 36, n. 2, p. 591-594, 2011.

VARTIAINEN, E.; MASSON, G.; BREYER, C.; MOSER, D.; ROMÁN MEDINA, E. Impact of weighted average cost of capital, capital expenditure, and other parameters on future utility-scale PV levelised cost of electricity. **Progress in Photovoltaics: Research and Applications**, 2019. DOI: 10.1002/pip.3189.

VILLANUEVA, J. K. S.; BLANCO, A. C. Optimization of Ground Control Point (gcp) Configuration for Unmanned Aerial Vehicle (uav) Survey Using Structure from Motion (sfm). **International Archives of the Photogrammetry, Remote Sensing and Spatial Information Sciences**, v. 42, n. 4/W12, 2019.

WALLACE, L.; LUCIEER, A.; MALENOVSKÝ, Z.; TURNER, D.; VOPĚNKA, P. Assessment of forest structure using two UAV techniques: A comparison of airborne laser scanning and structure from motion (SfM) point clouds. **Forests**, v. 7, n. 3, p. 62, 2016.

WAN, C.; ZHAO, J.; SONG, Y.; XU, Z.; LIN, J.; HU, Z. Photovoltaic and solar power forecasting for smart grid energy management. **CSEE Journal of Power and Energy Systems**, v. 1, n. 4, p. 38-46, 2015.

WANG, Z.; LIN, X.; TONG, N.; LI, Z.; SUN, S.; LIU, C. Optimal planning of a 100% renewable energy island supply system based on the integration of a concentrating solar power plant and desalination units. **International Journal of Electrical Power & Energy Systems**, v. 117, p. 105707, 2020.

WESTOBY, M. J.; BRASINGTON, J.; GLASSER, N. F.; HAMBREY, M. J.; REYNOLDS, J. M. 'Structure-from-Motion'photogrammetry: A low-cost, effective tool for geoscience applications. **Geomorphology**, v. 179, p. 300-314, 2012.

WILSON, John P.; GALLANT, John C. (Ed.). **Terrain analysis: principles and applications**. John Wiley & Sons, 2000.

WOLF, Paul; DEWITT, Bon; WILKINSON B. **Elements of photogrammetry: with applications in GIS**. Fourth Edition. McGraw-Hill Education Professional Publishing. 2014. ISBN: 978-0-07-176111-6.

WONG, M. S.; ZHU, R.; LIU, Z.; LU, L.; PENG, J.; TANG, Z.; CHAN, W. K. Estimation of Hong Kong's solar energy potential using GIS and remote sensing technologies. **Renewable Energy**, v. 99, p. 325-335, 2016.

WRIGHT, Natasha C. Justification for community-scale photovoltaic-powered electrodialysis desalination systems for inland rural villages in India. **Desalination**, v. 352, p. 82-91, 2014.

XIA, Xue; PERSELLO, Claudio; KOEVA, Mila. Deep fully convolutional networks for cadastral boundary detection from UAV images. **Remote sensing**, v. 11, n. 14, p. 1725, 2019.

YANG, D.; KLEISSL, J.; GUEYMARD, C. A.; PEDRO, H. T.; COIMBRA, C. History and trends in solar irradiance and PV power forecasting: A preliminary assessment and review using text mining. **Solar Energy**, v. 168, p. 60-101, 2018.

YAO, Huang; QIN, Rongjun; CHEN, Xiaoyu. Unmanned aerial vehicle for remote sensing applications—A review. **Remote Sensing**, v. 11, n. 12, p. 1443, 2019.

YUAN, Chi; ZHANG, Youmin; LIU, Zhixiang. A survey on technologies for automatic forest fire monitoring, detection, and fighting using unmanned aerial vehicles and remote sensing techniques. **Canadian journal of forest research**, v. 45, n. 7, p. 783-792, 2015.

YUSHCHENKO, A.; DE BONO, A.; CHATENOUX, B.; PATEL, M. K.; RAY, N. GIS-based assessment of photovoltaic (PV) and concentrated solar power (CSP) generation potential in West Africa. **Renewable and Sustainable Energy Reviews**, v. 81, p. 2088-2103, 2018.

ZARAGOZA, I.; CAROTI, G.; PIEMONTE, A.; RIEDEL, B.; TENGEN, D.; NIEMEIER, W. Structure from motion (SfM) processing of UAV images and combination with terrestrial laser scanning, applied for a 3D-documentation in a hazardous situation. **Geomatics, Natural Hazards and Risk**, v. 8, n. 2, p. 1492-1504, 2017.

ZARCO-TEJADA, P. J.; DIAZ-VARELA, R.; ANGILERI, V.; LOUDJANI, P. Tree height quantification using very high resolution imagery acquired from an unmanned aerial vehicle (UAV) and automatic 3D photo-reconstruction methods. **European journal of agronomy**, v. 55, p. 89-99, 2014.

ZHANG, Chunhua; KOVACS, John M. The application of small unmanned aerial systems for precision agriculture: a review. **Precision agriculture**, v. 13, n. 6, p. 693-712, 2012.

ZHANG, M., WANG, B., LIU, D. L., LIU, J., ZHANG, H., FENG, P., YU, Q. Incorporating dynamic factors for improving a GIS-based solar irradiance model. **Transactions in GIS**, 2020.

ZINK, R.; CAMARGO, L. R.; REIDELSTÜRZ, P.; DORNER, W. Photogrammetric point clouds for GIS-based high-resolution estimation of solar irradiance for roof-top solar systems. In: **Surface Models for Geosciences**. Springer, Cham, 2015. p. 293-305.

ZYGIARIS, Sotiris. Smart city reference model: Assisting planners to conceptualize the building of smart city innovation ecosystems. **Journal of the knowledge economy**, v. 4, n. 2, p. 217-231, 2013.